Graphene-based devices for terahertz technology

Panhui Huang

PSL UNIVERSITÉ PARIS

華東師範大學 EAST CHINA NORMAL UNIVERSITY

THÈSE DE DOCTORAT

DE L'UNIVERSITÉ PSL

Préparée à École normale supérieure

Dans le cadre d'une cotutelle avec East China Normal University

Dispostifs á base de graphéne pour la technologie terahertz

Graphene-based devices for terahertz technology

Soutenue par

Panhui HUANG

Le 16 07 2020

École doctorale n°397

Physique et Chimie des Matériaux

Spécialité

Chimie Physique

Composition du jury :

Emilien PEYTAVIT Chargé de recherche, Institut d'électronique de microélectronique et de nanotechnologie	*Rapporteur*
Guohong MA Full professor, Shanghai University	*Rapporteur*
Jérôme LESUEUR Professeur, ESPCI Paris	*Président*
Miriam Serena VITIELLO CNR-Director of Research, CNR-Istituto Nanoscienze and Scuola Normale Superiore	*Examinateur*
Yiming ZHU Professor, University of Shanghai for Science and Technology	*Examinateur*
Qingyuan JIN Professor, East China Normal University	*Co-directeur de thèse*
Juliette MANGENEY Directrice de recherche, Ecole normale supérieure	*Directrice de thèse*

ENS | PSL

Abstract

THz radiation is extremely attractive for fundamental investigations of matter and emerging applications including, for example, security screening, medical imaging, and spectroscopy. However, the THz spectral range remains one of the least exploited spectral regions, mainly due to the lack of compact powerful THz sources/amplifiers and passive devices. This thesis concerns the development of advanced THz devices based on graphene material.

The first project focuses on the carrier lifetime in neutral graphene-hBN van der Waals heterostructures under mid-infrared illumination. The carrier lifetime in such device for photoexcited carriers at low density and energy is reported to be 30ps using mid-infrared photoconductivity measurements. By igniting the hyperbolic phonon polaritons in hBN via an electrical or optical pump, we demonstrate that the carrier lifetime is switched from 30ps down to few picoseconds. This project opens interesting perspectives for the development of THz lasers by exploiting graphene/hBN heterostructures, for the realization of highly sensitive THz photodetectors as well as for phonon polariton optics.

The second project reports on original devices based on hybrid semiconductor-metal waveguides coupled to the graphene layer. These devices, which are easy to fabricate, can act as THz amplitude modulators and THz amplifiers. First, we numerically investigate the dispersion relation of the two fundamental propagation modes of these hybrid waveguides. Then, we experimentally characterize these graphene-coupled waveguides using THz time-domain spectroscopy. We demonstrate that these devices act as Mach-Zehnder modulators at 2 THz and 5.6 THz, the cut-off frequencies of TE0 and TE1 modes respectively. This project opens interesting perspectives on the modulation of THz waves and represents an important building block for the realization of THz lasers.

Acknowledgements

First, I want to sincerely thank Jérôme Lesueur, Emilien Peytavit, Guohong Ma, Miriam Serena Vitiello, Yiming Zhu as they accepted to be the jury members of my defense.

The four years' of Ph.D. career in laboratoire de phyique de l'ENS is an unforgettable period in my life as I worked with so many lovely people. The first person that I want to thank is my supervisor Juliette Mangeney. I can always feel your passion and optimism in research which encourages me, your profession and patience helped me a lot in my thesis and articles, you also pay high attention to the development of your students so we have many chances to participate important conferences to show our results and practice our abilities, and the most important thing you teach me is to be cool, you always tell me that and you are the coolest 'Shifu' I ever know in my life, it is my great pleasure to work with you. I want to thank Sukhdeep Dhillon, thank you for helping me with the micro bonding and your expertise in QCL, and thank you for your great concern on my administrative affairs. I want to thank Jérôme Tignon for the support in my course enrollment. Nano-THz is a great group, it is my great pleasure to work with you guys, Sylvain, Elisa, Simon, Romaine, Thibault, Niloufar, Valentino, Jacques, Chao, Seonggil, and the old members of this group, Sarah, Hanond, and Feihu. I also want to thank the people from the mesoscopic physics group, Holger and David who helped me a lot in the transport measurement and sample fabrication, Bernard Plaçais who provided me theoretical support in my thesis. Thank you Djamal from the QUAD group for lending me a good photo detector. I want to thank the technical and technological services of the LPENS as well, José and Aurelie from the cleanroom; Pascal from the design office; Phillipe from the electronics; Florent and Olivier from the cryogenics; Olga, Anne, Christine, and Valerie from the administrative service; Yann from the IT. Besides, I want to thank Stephane Emery and Eric Sinaman from the administrative service of ENS and Nadine Witkowski from doctorate school 397 of UPMC

I want to thank the people from ECNU, Professor Qingyuan Jin and Dr. Shitao Lou;

Xiaolin Liu, and Xiaoyan Liu from the PROSFER program who helped me in the administrative affairs.

Moreover, I want to thank the people outside of my schools, Miriam Vitiello and Alessandra Digaspare from NEST-CNR Pisa fabricated a series of high-quality waveguide sample; Jean-françois Lampin from IEMN Lille helped me with the interpretation of the data based on the interference effect; Aloyse Degiron helped me with the COMSOL simulation.

Special thanks to the China Scholarship Council(CSC) for the financial support and the councilor Mr. Chunqiao Wang from the education department of the Chinese embassy in France for the administrative support.

At last, I want to thank all my friends in ENS & ECNU and my family, especially my chou-chou Na, I sincerely cherish the life with you in Paris. The year 2020 is a magic realism year, I wish the world would be in love and peace.

Contents

Chapter 1

Introduction

1.1 General context

The far-infrared part of the electromagnetic spectrum, presently known as the terahertz (THz) domain, is of outstanding interest in physics offering unique applications in various domains and also very appealing fundamental investigations. THz radiation usually ranges between 10^{11} Hz to 10^{13} Hz, corresponding to wavelength ranging from 0.03 mm to 3 mm and photon energy ranging from 0.41 meV to 41 meV; the THz spectral range lies between the microwave and mid-infrared ranges (see Figure 1.1). Historically, the first THz emission was obtained by the extension to the low frequencies of conventional infrared thermal radiation. In 1911, Rubens and Baeyer have shown that the mercury arc lamp sealed in a quartz envelope is an excellent source of far-infrared radiation with emission up to wavelengths of 430 µm [1]. This source, which is equivalent to the radiation of a black body whose temperature would be 4 000 K, remains the preferred source of spectrometers and modern network THz interferometers. Since this first demonstration of THz emission, intensive research has been dedicated to this specific spectral region.

The motivation of the research works is that THz photons have very interesting and unique properties. For instance, the absorption spectrum linked to vibration modes of molecules have resonances that fall in the THz frequency range. Due to the collective nature of these modes, they are very sensitive to the structure, the conformation of the molecule and to its environment [2]. So an important characteristic of spectroscopy in the THz domain is its ability to observe inter-molecular vibrations, while conventional infrared spectroscopy is sensitive only to intra-molecular vibrations. In astrophysics, we can cite the observations of thermal radiation at THz frequencies, which are important for characterizing cold dust (10-20 K) in the interstellar medium of our galaxy[3]. Moreover, many elementary processes in condensed matter, such as the interaction of electrons,

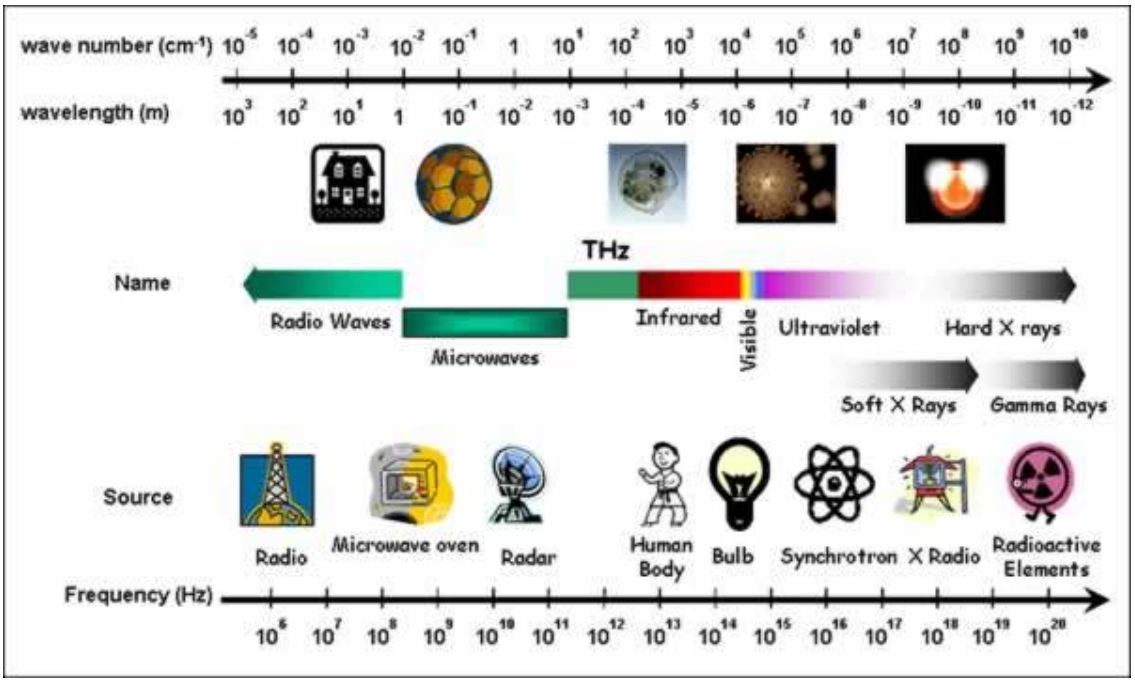

Fig. 1.1 *Table of electromagnetic waves from* http://t.ly/dNGAw

spins and phonons, possess resonance frequencies in the THz spectral range[4]. While visible light usually provides excessive photon energy for collective excitations in matter systems, THz light allows for direct coupling to these low-energy (meV scale) excitations. The corresponding (sub)-picosecond period corresponds to the time-scale of elementary chemical reactions, weak collective excitations in solids, the relaxation time of phonons, free carriers collision time. In addition, THz photons can penetrate a wide variety of non-conducting materials. They can pass through clothing, paper, cardboard, wood, masonry, plastic and ceramics, but they cannot penetrate metal and are strongly attenuated in water. At last, owing to their low energy, they are non-ionizing compared to x-rays.

All of these features of THz photons are very appealing for a wide variety of applications. For instance, THz technology is attractive for homeland security since metallic objects (such as weapons) reflect THz waves and thus can be easily identified by THz imaging. THz technology is also very attractive for non-destructive testing and non-destructive thickness measurements[5]. For instance, for quality control in the pharmaceutical industry, the contact-free thickness gauging of tablet coatings using THz systems is very useful since tablet coatings regulate the release of the drug inside the body. Moreover, the combination of THz imaging and thickness measurement can help to restore ancient paintings without being invasive[6]. For biomedical application, THz systems can help doctors non-invasively detecting cancerous tissue in early time [7], and THz biosensors are able to

ultrasensitively trace the risk in a human body at virus scale[7]. Besides, THz radiation is expected to support future wireless telecommunication systems to overcome the limited spectral resources above 60 GHz. Indeed, a significant capacity enhancement to multi-gigabit or even terabit wireless transmission requires larger bandwidths, which are only available in the THz region. Exploiting the transmission window between 200 GHz and 300 GHz, S. Koenig *et al.* have successfully demonstrated wireless link with a maximum data rate of 100 Gbit/s bridging a distance of 20 m near 237.5 GHz [8].

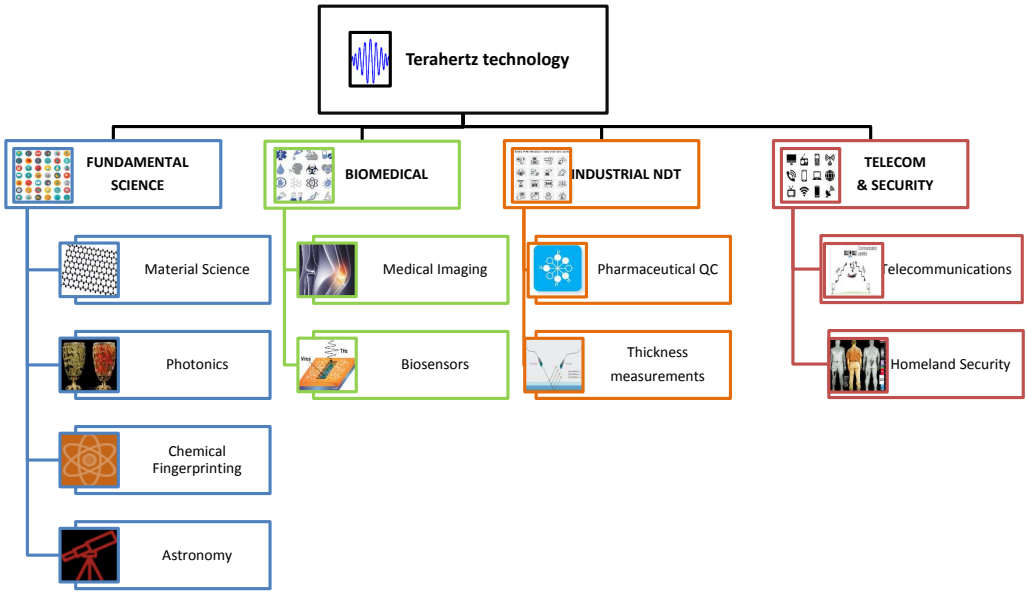

Fig. 1.2 *THz technology for fundamental science and applications.*

Despite these useful attributes, the THz spectral range remains one of the least technologically developed spectral regions owing to the lack of compact powerful sources. For instance, a compact powerful THz laser operating at room temperature, analogous to the semiconductor laser diode in the visible and near-infrared wavelength ranges is not available today[9]. Actually, this frequency domain moderately benefits from techniques from the two neighboring infrared and microwave domains[10]. Indeed, radiation sources, whether optical or electronic, see their effectiveness fall sharply when the frequencies approach and reach the THz domain. The fundamental physical limitations of conventional optical sources at large wavelengths are due to the absence of an appropriate material with a sufficiently small bandgap. The longest wavelength laser diodes are based on lead salt materials and do not extend beyond 20 µm [11] (i.e. below 15 THz) due to the interactions between carriers (Auger effect, ...) which favor non-radiative recombinations. On side of conventional electronic sources, the fundamental limitations come mainly from the transit time of the carriers and the RC time constants. So to operate at a very high

frequency, a reduction in the dimensions of electronic sources is necessary, limiting the delivered power available. Consequently, current THz sources are either bulky or deliver moderate power. A major technological breakthrough for modern THz technology would therefore to develop a compact and powerful THz laser alternatively a compact and powerful THz amplifier.

Moreover, the various application fields of THz radiation define stringent requirements for high-performance THz passive components such as waveplates, lenses[12, 13], waveguides[14], and modulators[15], which are readily available for the optical, infrared, and microwave regions of the electromagnetic spectrum but not necessarily for the THz frequency regime. For instance, the lack of efficient components to modulate the propagation properties of the THz wave is a major barrier for the further development of THz technology. In addition, THz modulators can be very useful for imaging and active mode-locking. Nowadays, important efforts are dedicated to the developments of efficient and compact passive THz components such as THz modulators, but their development is in its infancy.

In addition, passive waveguide components with low-loss and low-dispersion allowing to guide THz waveguides with greater confinement than free-space are highly desired for several applications. Indeed, the foremost advantage is that the bulk optics used for manipulating THz radiation in free space can be replaced by waveguides. This will open up new opportunities in the further development of compact THz systems and consequently lab-on-chip systems. The diffraction-limited spot size can be reduced further, resulting in a resolution improvement over free-space THz imaging systems. Also, tight mode confinement can be achieved by exploiting waveguides with subwavelength features. This is beneficial for THz sensing applications, specifically for noninvasive and label-free molecular detection, and gas and liquid spectroscopy. Other THz devices such as the near-field scanning optical microscope, THz sources based on QCL, imaging, and communication technologies, which revolve around THz waveguides, will have improved functionalities with the development of advanced THz waveguides.

Thesis objectives The main objective of this thesis is to investigate the potential of graphene as an active material for future developments of THz sources, amplifiers and modulators. To this aim, we investigate the carrier recombination time in graphene under illumination that has to reach tens of picoseconds for graphene to be effective for THz amplifiers and lasers. We also focus on graphene-based modulators based on original hybrid THz waveguides. To place my work in the general frame of THz technology, in the

following sections, I will give an overview of the state of the art of sources, amplifiers, modulators and waveguides operating at THz frequencies. As my work aims to exploit the graphene for the development of such devices, I will introduce the properties of graphene that are interesting for THz technology.

1.2 State-of-the-art

1.2.1 THz sources

Since many decades, tremendous progress has been made in the development of powerful THz sources. The current THz sources rely on various different schemes. Table 1.1 presents some of the main THz sources available today.

Classification	***Source type***
Vacuum electronic	Gyrotrons Klystron Synchrontrons Travelling wave tubes
Solid-state electronic	Transistors Superconductors Electronic sources based on frequency multiplication
Lasers	Quantum cascade lasers Free electron lasers Gas lasers p-Germanium lasers
Laser-pumped sources(continuous)	Photomixers
Laser-pumped sources(pulsed)	Photoconductive switches Nonlinearity in graphene Magnetic dipoles and magnetic heterostructures Dipoles in liquids Optical rectification in bulk material and based on surface effect

Table 1.1: Examples of current THz sources

A large part of THz sources are vacuum electronic sources including gyrotrons [16], klystrons [17], synchrontrons[18]. The pulsed gyrotron can reach power of 5 kW [19] and 200 kW[20] at frequencies of 1 THz and 0.7 THz respectively with a pulse duration of tens of μs. In continuous wave, gyrotrons can deliver an output power of 100 W at 0.2 THz [21]. Such output power from gyrotron sources is promising but they need of highly

driven magnetic field that limits their compactness. Klystron sources are able to reach high output power up to 500 W while the operating frequency is limited to a moderate value of 200 GHz and the bandwidth is relatively low[22]. The synchrotron THz source is very hard to be implemented even it can deliver intense output power [23].

The other category of electronic THz sources are solid-state electronic sources including transistors[24] and superconductors[25]. Indium phosphide transistors have been able to reach maximum oscillation frequency values of over 1 THz for around a decade already. Moreover, transistors have the advantage to provide gain so that THz amplification can be achieved. However, increase the frequency of transistors above 1 THz is hardly achievable. The superconductor-based sources are limited by the complex realization of superconducting condition.

The free-electron laser can generate very high average THz powers, reportedly up to 0.5 kW, but is very bulky and expensive and is therefore only practical for selected scientific applications[26].

THz gas lasers, which have been demonstrated around since the late 1960s[27, 9, 28, 29], can provide watts of power in continuous-wave, but they are usually pumped by CO2-lasers making them complex and expensive. Very recently, the group of J.F. Lampin has demonstrated for the first time a table-top continuous-wave THz molecular (NH_3) laser optically pumped by a mid-infrared quantum cascade laser delivering a power of 34 μW at 1.07 THz[30, 29].

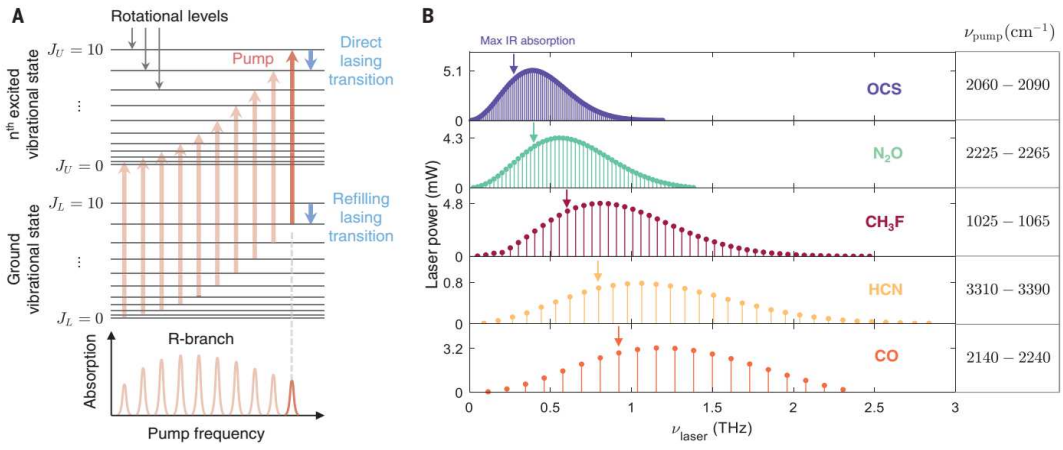

Fig. 1.3 *A: Diagram showing the rotational levels of the NH_3 molecule for the ground and excited vibrational states[29]. B: Plots showing the tuning range and power of a QCL-pumped molecular laser[29].*

Alternatively, semiconductor THz lasers such as the quantum cascade lasers (QCL)[31, 32] and the p-Germanium lasers, which involve intersubband transitions are, in principle, compact, powerful and cost-effective. They offer tunability over large bandwidth with milliwatt output power[33, 32]. However, despite extensive research effort, THz QCLs delivering a few mW of average power have a limited maximum operating temperature (∼200 K) and thus requires cryogenic cooling, which adds complexity and cost. As for the p-Germanium laser[34, 35], although it provides an enormous peak output power of up to 10 W, the operation is limited to liquid Helium temperature, which is inappropriate for most high-volume applications.

A wide variety of alternative techniques have also been developed for THz generation based on down-conversion from the visible and mid-infrared regime or by multiplication up from the millimeter-wave regime. These systems are fairly compact systems. Down-conversion techniques used laser systems and are mostly achieved using nonlinear effects in crystals or photoconductive effects. For instance, illuminating a nonlinear medium by short intense optical pulses results in the emission of coherent THz radiation by optical rectification effect (relying on the generation of quasi-DC polarization in the nonlinear medium). This effect can be achieved in both bulk materials and surface materials [36, 37]. A down-conversion technique to generate coherent THz radiation that is also widely widespread is based on photoconductive antennas illuminated by optical radiation. By beating two continuous optical lasers in a photoconductive antenna made of an ultrafast semiconductor (used as photomixer), continuous THz radiation is generated with a very narrow spectral bandwidth. In return, illuminating by femtosecond optical pulses a photoconductive antenna leads to coherent ultra-broadband THz emission [38]. More recently, it has been demonstrated that by illuminating with femtosecond optical pulses ferromagnetic/non-ferromagnetic layers, a THz emission is produced based on inverse spin Hall effect[39]. Beaurepaire *et al.* demonstrated that the THz emission is induced by an ultrafast demagnetization of ferromagnetic films [40]. Coherent THz emission from monolayer graphene excited by femtosecond optical pulses have also been reported by our team [41]. The emission process relies on a nonlinear effect, the photon drag effect, which is induced by the transfer of light momentum to carriers through ponderomotive electric and magnetic forces. D. Sun *et al.* [42] and P.A Obraztsov *et al.* also report such THz emission generated from graphene illuminated by ultrashort optical pulses. Electronic sources based on multiplication up from the millimeter-wave regime are one of the most used THz sources. They use a microwave signal generator and diode frequency multipliers to typically extend the emission up to 1.1 THz with an output power of 5 μW. Diode frequency multipliers utilize the reactive and/or resistive nonlinearity of the diode to generate harmonics of an input signal. By providing appropriate embedding impedances at

each integer multiple of the input frequency, it is possible to design frequency doublers, triplers, or even quintuplers. The dominant technology is based on GaAs Schottky diodes.

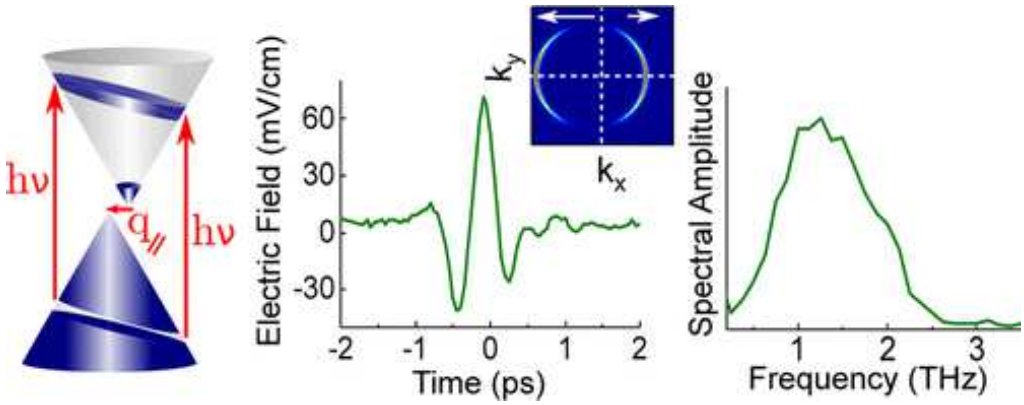

Fig. 1.4 *Coherent THz emission by dynamical photon drag effect in graphene excited by fs optical pulses at room temperature [41].*

All of these techniques based on nonlinear conversion at room temperature are relatively compact. However, the THz powers delivered by these techniques remain moderate.

1.2.2 THz amplifiers

An alternative strategy to develop compact and powerful THz sources is to amplify the output power delivered by THz sources using a compact and effective THz amplifier. Table 1.2 presents some of the main THz amplifiers:

Amplifiers	***Reference***
Semiconductor integrated cirtcuits	
High electron mobility transistors(HEMT) and metamorphic HEMT	[43]
Vacuum electronic devices	[44]
Quantum cascade structures	[45, 46, 47].

Table 1.2: Examples of current THz amplifiers

THz amplifiers are roughly categorized in three distinct technology: solid-state amplifiers composed of semiconductor integrated circuits, vacuum electronic devices and quantum cascade structures.

THz amplifiers based on high frequency monolithic millimeter-wave integrated circuits have been widely investigated[48]. For power, GaN high electron mobility transistors

(HEMTs) have achieved the highest power at lower frequencies (more than 0.5 W at 100 GHz)[49], while at higher frequencies, InP HEMTs[43] and heterojunction bipolar transistors have the highest reported power, in the 20-100 mW range around 200 GHz and in the 1-10mW range for amplifiers around 300 GHz[50].

Based on a micromachined vacuum tube, power amplifiers at 0.85 THz have been demonstrated with 100 mW output power owing the high linearity, with a 21.5 dB gain, 15 GHz of operational bandwidth and a device efficiency of 0.44 %[44].

Some designs based on quantum cascade vertical structures have been theoretically investigated for THz amplification. Experimentally, in 2007, Mauro *et al.* have demonstrated the amplification of THz radiation in a quantum cascade structure at 2.3 THz with an enhanced magnitude of 1.5 × [45]. In 2014, Ren *et al.* have reported the realization of THz amplification by depositing an anti-reflective coating on the QCL facet so that the losses of the laser mirrors are enhanced to fully suppress the lasing action. They succeeded to achieve an optical gain of 30 dB with single-mode radiation at 2.9 THz[46].

1.2.3 THz amplitude modulators

Besides the need for compact and powerful THz emitters, progress on passive THz components is also crucial to support the proliferation of THz technology outside of research laboratories. Among them, THz modulators are crucial components since they allow controlling the amplitude, phase, or polarization of THz waves. Thus, many applications in the THz field including but not limited to gas and solid-state spectroscopy, biosensing, astronomy are in great demand for THz modulators with high modulation speed and depth. To meet these needs, a variety of THz modulators that achieve various functions in different architectures have been designed and some of them have been practically developed. There are mainly three types of THz modulators: all-optical types, all-electronic types and microelectromechanical systems (MEMS) [51]. This section is not intended to cover every single state-of-art approaches, but rather to highlight some outstanding works from all-optical and all-electronic devices, especially for amplitude modulators.

All-optical type The main idea of THz optical modulators is to tune the characteristics of THz waves via optical-induced modification of the device properties such as optical conductivity or charge mobility. The sources used for the illumination of THz modulators are often selected from cw or pulsed lasers with a wavelength in the visible or near-infrared spectrum. The modulation speed is often limited by the recombination time of photogenerated carriers. At the first stage, different bulk materials such as silicon, GaAs[52, 53, 54, 55], or Germium have been used to realize THz modulation without

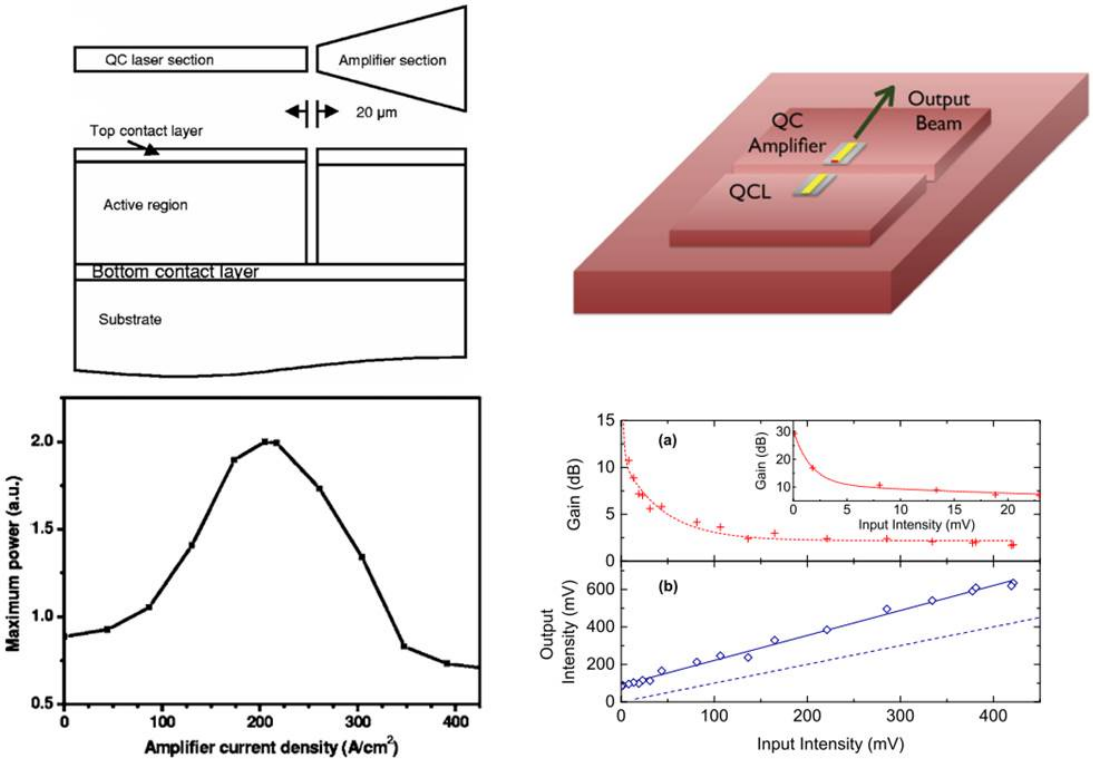

Fig. 1.5 *Left: A schematic diagram of the master-oscillator power-amplifier structure from[45] (up); the maximum power as a function of the amplifier current density delivering by the the master-oscillator power-amplifier structure (bottom). Right: A schematic drawing of the amplifier based device from [46] (up). The corresponding gain and output power of the device as a function of the input intensity (bottom).*

extra components. The modulation depth can reach almost 100% with pump intensity > 540 $\mu J/cm^2$[52] at 10^5 Hz modulation rate, or time-averaged pump power > 40 mW[53]. Then, new methods that lowered the optical pump required to reach the same modulation efficiency were implemented by introducing a polymer/inorganic interface[55] or by the deposition of 2D materials on the semiconductors[53, 56, 57]. Towards the improvement of performances, approaches were developed to improve the light-matter interaction using metamaterials or plasmonic resonant structures[58, 59].

All-electronic type While all-optical THz modulators rely on a relatively bulky laser system, for some applications, a more compact design is needed. This issue is overcome by all-electronic THz modulators. An early success of the all-electronic THz modulator was demonstrated in 2004[60]. Klein-Ostmann *et al.* has fabricated a HEMT-like structure with undoped GaAs, undoped AlGaAs, and silicon-doped GaAs. Their approach

is to manipulate the electron density in a gated two-dimensional electron gas system at room temperature, realizing the amplitude modulation of the THz waves. Although the reported achievable modulation depth of their work is only 3% with 10 kHz modulation speed, they provide a feasible way to implement all-electronic THz modulation. With this concept, some new ideas to enhance the modulation efficiency have emerged with the use of metamaterials or 2D materials. For instance, metamaterial resonant devices have been integrated into the THz modulator forming as a Schottky barrier to allow dynamical damping of the resonance[61]. With this strategy, the achievable modulation efficiency reaches 50% around 1 THz.

1.2.4 THz waveguides

The development of THz waveguides has been subject to many research works intending to realize a wide variety of functions such as transmission, amplification, modulation, and so on. There are two main issues in designing THz waveguides, the first one is that most materials highly absorb THz waves so that the long-distance propagation is hard. The other one is that the group velocity dispersion of several standard waveguides is high, which results in THz pulse broadening over centimeter distance scale[62]. To design a low-loss and low-dispersion THz waveguides, there are a variety of approaches benefiting from different aspects such as the use of low-loss materials[63], the achievement of strong confinement obtained from geometries, the use of metamaterials and 2D materials like graphene[64, 65]. THz waveguides currently provide absorption loss lower than 0.1 cm^{-1} at THz frequencies with almost zero dispersion. Selecting materials that are suitable for the fabrication of waveguides is one of the major barriers to advancing this field. Dry air, as its low loss and barely non-cost, is considered as an ideal guiding material. The main task to develop waveguides based on dry air is to confine the THz waves. One solution is the metallic waveguides. Structured metals have a high ohmic loss in THz range but they can provide strong confinement, so the basic idea is to confine THz waves with a metallic structure and guide the THz waves in dry air. Then, designing the geometry of the metallic waveguides is crucial for their optimization. To name a few, commonly-used structures are : circular cross-section waveguides[66], parallel-plate waveguides[67, 68, 69], bare metal wires[70, 71], metallic slot waveguides[72]. Another solution is the dielectric waveguide. There are some dielectric materials such as high-resistivity silicon, high-resistivity GaAs, polytetrafluoroethylene(Teflon), TOPAS, Zeonex, etc. that possess relatively low-loss at THz frequencies. In terms of geometry, the dielectric waveguides can be divided into hollow-core waveguides/fibres[73, 74, 75, 76, 77], solid-core waveguides/fibres[78, 63], and porous-core waveguides[79, 80, 81]. The difference between hollow-core structure and solid-core is whether the THz wave is guided in the air or in the dielectric materials.

In summary of this state-of-the-art, current THz technologies suffer from the lack of compact room temperature THz sources/amplifiers and efficient THz passive components, limiting the proliferation of consumer applications. As a consequence, an important activity in this field is dedicated to improving the performances of current sources/amplifiers and passive components. In parallel, an important effort is dedicated to the study of new physical properties within novel materials. Among them, graphene is gaining increasing attention for new developments in the THz domain owing to its unique electrical and optical properties.

1.3 Graphene for THz technology

Graphene, the first discovered two-dimensional material, has been placed with great exceptions on a wide variety of fields thanks to its unique properties. The first theoretical model of its band structure was described by P. Wallace [82] in 1947. This monoatomic layer of carbon was named graphene in 1986 [83]. Two decades later, in 2004, the first graphene sample composed of three layers of graphene was fabricated in a laboratory, showing remarkable two-dimensional electron behavior.

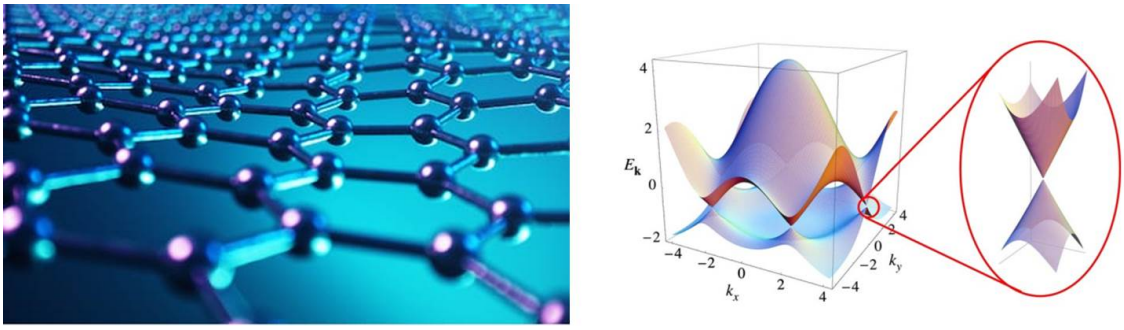

Fig. 1.6 *Left: Artistic view of graphene from* https://www.shutterstock.com/fr/search/graphene. *Right: The band structure of graphene in Brillouin zone.*

1.3.1 Electronic band structure of graphene

There are numbers of nice introductions and reviews about the electronic properties of graphene, so I give here only a brief introduction with important results related to the band structure of graphene. The graphene is composed of carbon atoms in a regular hexagonal structure with a constant C-C distance $a = 1.42\,\text{Å}$, as it shown in Figure 1.7 (left). Generally, the graphene is described as the superposition of two spatially symmetric sublattice A and B and the unique electronic characterization is based on this structure.

These two sublattices are described by the vectors:

$$\vec{a_1} = \frac{a}{2}(3, \sqrt{3}) \qquad \vec{a_2} = \frac{a}{2}(3, -\sqrt{3})$$

so in the reciprocal space, they are written as:

$$\vec{b_1} = \frac{2\pi}{3a}(1, \sqrt{3}) \qquad \vec{b_1} = \frac{2\pi}{3a}(1, -\sqrt{3})$$

which define the Brillouin zone of graphene depicted in Figure 1.7 (right). By using tight

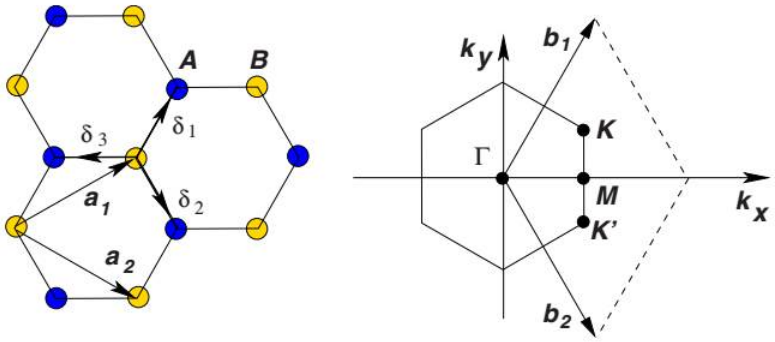

Fig. 1.7 *Geometry of graphene in real and reciprocal space. Left: Hexagonal honeycomb lattice in real space, the vectors a1 and a2 and the atoms A and B define the Bravais network. Right: Corresponding Brillouin zone where* Γ *is the centre of the first Brillouin zone and K and K its Dirac points[84].*

binding approach with the next nearest-neighbor approximation, one can calculate the electronic band structure and obtain the energy dispersion relation for electrons in the π bands in the reciprocal space:

$$E_{\pm}(\vec{k}) = \pm t\sqrt{3 + f(\vec{k})} - t' f(\vec{k})$$

t and t' represent the hopping energies for nearest neighbor and next nearest neighbor atoms, the plus and minus sign refers to the conduction and valence band respectively. There are two important coordinates in the Brillouin zone which are **K** and **K'**, they are called Dirac points. Near the Dirac points, the energy dispersion $E(\vec{k})$ has a conical shape(see Figure 1.6) called Dirac cone, and it follows a linear relation with wave vector k:

$$E(\vec{k}) = \pm \hbar v_F |\vec{k}|$$

v_F being the Fermi velocity $v_F \approx 10^6$ m/s. The zero bandgap and the linearity of the band structure are among the most distinctive features of graphene.

More generally, graphene has several properties particularly attractive for THz technology. For instance, THz photons can instigate interband transitions at THz frequencies owing to its zero bandgap, which opens the way for the realization of THz lasers/amplifiers. S. Massabeau *et al.* have recently demonstrated interband transitions in multilayer graphene at THz frequencies [85]. Moreover, population inversion in graphene under optical excitation close to the Dirac point has been reported suggesting that THz lasing and amplification may be possible[86]. Combining multilayer optically pumped graphene multilayers with a traveling-wave waveguide[87], THz amplification has been predicted at room temperature. In 2018, Guo *et al.* [88] have proposed an original design to achieve efficiently tunable and compact THz amplifiers and lasers based on active THz hyperbolic metamaterials composed with multiple stacked photoexcited graphene layers separated by thin dielectric sheets. As well, A. A. Dubinov *et al.* have recently proposed a new scheme for THz laser based on resonant photon-assisted transitions in multiple graphene layer structure embedded in a surface plasmonic waveguide for emission ranging from 5 to 12 THz. However, due to very efficient non-radiative processes, in particular, Auger-recombination processes [89], the lifetime of hot carriers in graphene and thus of the optical gain in graphene is limited to a few hundreds of femtoseconds. This short-lived optical gain in graphene is detrimental to the development of THz lasers. This main issue has to be overcome for opening the possibility to develop powerful THz lasers and amplifiers based on interband transitions in graphene at THz frequencies.

Another interesting property is the high optical phonon energy in graphene, $\sim$ 200 meV, which is very promising for operation at room temperature. Moreover, the mobility of carriers in graphene is very high, which is very suitable for the realization of sensitive THz photodetectors and THz transistors. As well, the optical properties of graphene can be very easily tuned with a simple electrostatic gate; these properties can be exploited for the development of THz modulators. At last, plasmons in graphene have resonances at THz frequencies opening the field of THz plasmonic. For instance, optical gain at THz frequencies based on graphene plasmon or graphene plasmon polariton has been proposed. The main idea is to realize the THz amplification via a stimulated generation of plasmon or plasmon polariton in graphene with different approaches. The realization of plasmons can benefit from different strategies such as periodical or resonant structures[90, 91, 92, 93], hyperbolic metamaterial[94], plasmonic crystals[95] and so on. The feasibility of the graphene plasmon polariton to produce THz amplification was experimentally demonstrated by Watanabe *et al.* in 2013. They observed gain enhancement effect of surface plasmon polaritons on THz stimulated emission in optically pumped monolayer graphene[96].

1.4 Thesis outline

In this thesis work, we investigate the potential of graphene as an active material for future developments of THz sources and amplifiers that involves radiative interband transitions. We also study the potential of graphene for the development of THz modulators. The content is organized as below:

- The introduction gives the general context of this thesis and the related THz technology's state-of-art.
- The second chapter investigates the dark current characteristics of graphene/hBN-graphene phototransistor at low temperature. We show that the dark current at charge neutrality point is governed by Zener-Klein tunneling current that corresponds to an electrical pump of non-equilibrium carriers.
- The third chapter studies the recombination process in the graphene/hBN phototransitors of non-equilibrium carriers generated by mid-infrared illumination. First, we investigate the linear photoconductive regime and extract the carrier lifetime. Then we investigate the non-linear regimes that involve the emission of hyperbolic phonon polariton in the hBN layers. We also study the dependence of the carrier lifetime with the bias and optical power and study the interplay between optical and electrical pumping.
- The fourth chapter proposes an original design of hybrid metal-dielectric waveguides coupled to graphene. Using a 2D Finite Element Method calculation, we numerically study the dispersion relation of the two fundamental modes propagating along these hybrid waveguides and when they are coupled to a graphene layer. We focus on the enhancement of the THz light-graphene interaction and on the modulation efficiency of THz modes propagating along these graphene-coupled hybrid waveguides. We also evaluate the possibility to enhance THz gain in graphene owing to its coupling with these hybrid waveguides.
- In the fifth chapter, we investigate experimentally the hybrid metal-dielectric waveguides. After preliminary characterization using Raman spectroscopy and electrical measurements, we use THz time-domain spectroscopy system to characterize the quasi-TE modes propagating along these hybrid waveguides at THz frequencies. We also study the modulation of THz waves by modulating the chemical potential of the graphene layer. From the confrontation between measurements and calculation based on interference effects, we demonstrate the Mach-Zehnder behavior of these graphene-coupled metal-dielectric waveguides.

Chapter 2

Graphene/hBN phototransistors: transport properties

This chapter includes parts of our full article: Ultra-long carrier lifetime in neutral graphene-hBN van der Waals heterostructures under mid-infrared illumination, P. Huang et al., Nature Communications 11, 863 (2020) [97].

2.1 Introduction

As discussed in the introduction, the unique optoelectronic properties of graphene make it a new platform for the development of advanced THz passive and active devices. Especially, graphene is potentially an excellent candidate for the development of a THz semiconductor-laser model owing to its zero bandgap. Indeed, graphene could provide the gain medium at THz frequencies for lasers/amplifiers [98, 99]. As well, THz photodetectors based on graphene have shown very promising results so far owing to the high carrier mobility in graphene and its broad absorption spectrum [100, 101, 102]. In addition, as the optical phonon energy in graphene is high ($\sim$ 200 meV) compared to the thermal energy at room temperature ($\sim$ 25 meV), valuable performances of graphene-based devices should be preserved up to room temperature. Recent progress in the 2D material fabrication has made accessible the full encapsulation of graphene by two hBN layers. This encapsulation protects the graphene layer from chemical contamination, even during technological processes, preserving the high quality of the graphene layer. As a result, in hBN/graphene heterostructures, the disorder is weak and the chemical potential of the graphene layer can be finely tuned to very low values[103]. Achieving low-doping values in graphene is crucial to avoid Pauli blocking effect at low energy (i.e. for photon frequency in the THz range) so that interband transitions are allowed in the THz spectral

range.

For the realization of a THz laser, carrier lifetimes of a few tens of picoseconds are needed to reach long-lived optical gain. As well, for a compromise between sensitivity and speed in THz photoconductors based on graphene, carrier lifetimes of a few tens of picoseconds are also required. More generally, the recombination dynamics of non-equilibrium carriers close to the Dirac point in graphene plays a crucial role in the performance of optoelectronic THz devices based on interband transitions and recombination times of at least a few tens of picoseconds are often highly desirable[101, 104, 105, 106].

The recombination dynamics of non-equilibrium carriers in graphene has been widely investigated[107, 108, 109, 110]. Mostly, femtosecond visible or near infrared pulses are used to generate hot non-equilibrium carriers of large density at high energies as illustrated in Figure 2.1. After photoexcitation, the electron/hole populations are both redistributed (by energy-conserving intraband carrier-carrier scattering) and relaxed (by intraband electron-optical phonon scattering) within 50fs. It results in two independent lower-energy broad electron and hole distributions, for which efficient interband Auger recombinaison processes leads to a single Fermi-Dirac distribution for conduction and valence populations within 100–200 fs. A subsequent cooling process occurs mediated by interband optical phonon emissions within 1-2 ps and by less efficient intraband acoustical phonon scattering[108, 111].

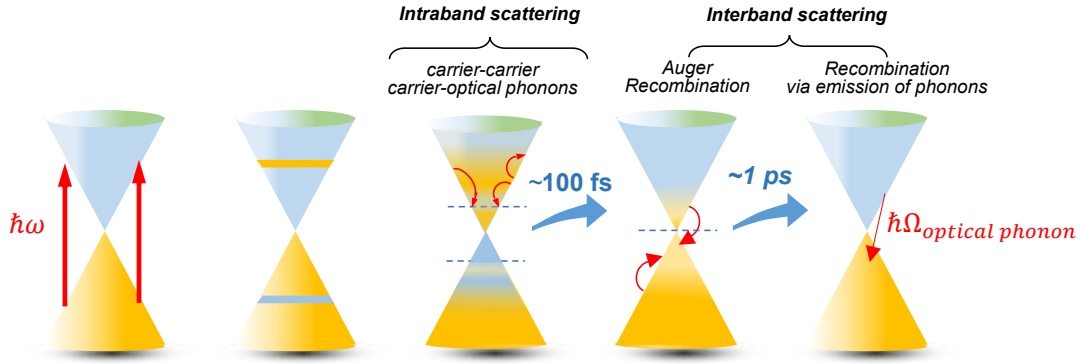

Fig. 2.1 *The relaxation and recombination process in graphene. From left to right: after photoexcitation, the redistribution and relaxation of electrons and holes within their respective bands via intraband process; recombination of electrons and holes via interband Auger processes and via interband optical phonon emission.*

Very recently, an additional recombination channel with picosecond decay time has been demonstrated in hBN encapsulated graphene relying on the coupling of hot carriers in graphene with hyperbolic phonon-polaritons (HPhP) in the hBN layers[112, 113]. Few studies have used an optical pump with energies lower than optical phonon energy and reported significant slowing of the carrier relaxation[114]. However, due to the excitation of a large density of hot carriers, optical-phonon emission remained the predominant relaxation channel[114, 115]. In spite of intensive work, the investigation of recombination dynamic for carriers at low photon energy and fluence remains elusive in graphene, notably under dc bias control.

In this thesis, we investigate the recombination processes of non-equilibrium at low density and energy, using mid-infrared photoconductivity measurements. For this purpose, we fabricate hBN/graphene phototransistors and set graphene at charge neutrality point (CNP). We use continuous mid-infrared laser excitation ($\hbar\omega = 117meV$) to provide weak incident photon density and corresponds to a photon energy between the Fermi-level fluctuations (typically $\sim$ 20 meV in graphene/hBN heterostructures) and the optical phonons of graphene and hBN ($\hbar\Omega \approx$170-200 meV) as illustrated in Figure 2.2.

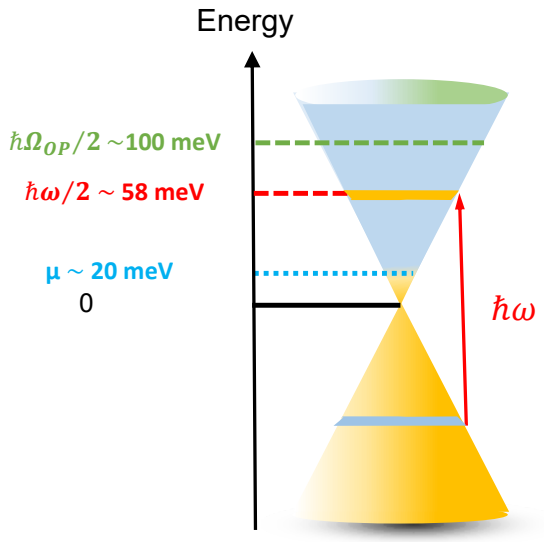

Fig. 2.2 *A schematic view, which illustrates our experimental condition : the incident photon energy lies between the Fermi-level fluctuations in graphene/hBN heterostructures and the optical phonons of graphene and hBN*

.

In this chapter, we will first introduce the fabrication of the graphene/hBN photo-

transistors performed by Elisa Riccardi in my research group. Secondly, I will present the experimental set-up I built for the measurement of transport in these devices. Then I will discuss the different contributions of currents in graphene and show the dark current characteristics of the hBN/graphene phototransistors. The investigation related to the photocurrent characteristic of the hBN/graphene phototransistors under mid-infrared illumination will be described in the next chapter.

2.2 Fabrication of the graphene/hBN phototransistors

The fabrication of the graphene/hBN phototransistors, performed by Elisa Riccardi in my research group, starts with the mechanical exfoliation of monolayer graphene and two hexagonal BN flakes from bulk crystals. We identified monolayer graphene sample by optical contrast and Raman spectroscopy and clean hBN flakes were chosen after bright- and dark-field optical microscopy. Afterwards, we encapsulated one monolayer graphene into two hBN flakes to be a van der Waals heterostructures by hot pick-up technique[116]. The heterostructure is transfered onto an intrinsic silicon (Si) substrate with a 500-nm-thick thermal oxide (SiO_2) layer on top.

The resistivity of the intrinsic Si substrate is $> 8000\ \Omega \cdot cm$. We localized the encapsulated graphene using Raman spectroscopy. We perform a map scan based on scanning pixel to check precisely the homogeneity of the graphene layer over large dimensions, the Raman map is reported in Figure 2.3b. We also measured the hBN thickness and roughness using atomic force microscopy. After the sample characterization, we performed e-beam lithography on the heterostructure in order to define the design of the device on the cleanest region of the sandwich and to obtain an HSQ resist mask. This mask was used to etch (Reactive Ion Etching) the top hBN layer in order to connect the graphene with one-dimensional edge contacts [117] . The last step of the device fabrication was the e-beam lithography to design the source, drain, and gate electrodes and metal evaporation (Cr-Au).

Hot pick-up technique The assembly of graphene and hBN flakes has five steps[116]:

- **Step1**: Use a piece of silicon dioxide slab to pick up an hBN flake held by a micromanipulator and PDMS/PPC contact.
- **Step2**: Settle the hBN flake on top of the graphene.
- **Step3**: Bake the hBN/graphene to solidify the liaison between them.

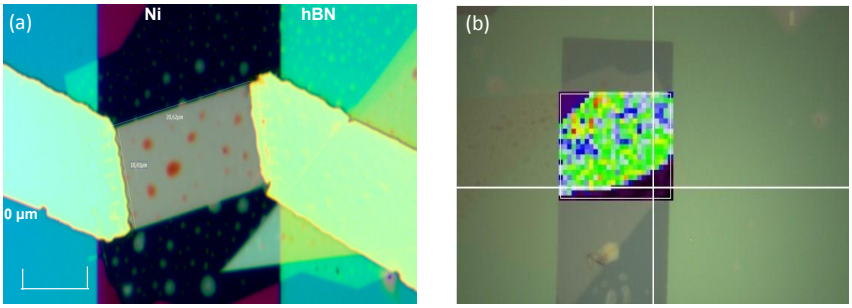

Fig. 2.3 *a) An optical microscopic image of the hBN-encapsulated graphene device with a semi-transparent Ni bottom gate electrode. b) Raman characterization of the hBN/graphene heterostructure during the fabrication process, the area with light color indicates the coverage of graphene.*

- **Step4**: Pick up of the hBN/graphene stack from SiO_2 substrate and repeat the step 1.

- **Step5**: Drop down the hBN/graphene stack on the bottom of the hBN. We transfer the encapsulated graphene on top of a 12nm thick nickel electrode, we measured the thickness and roughness of the hBN layer by using AFM spectroscopy (see Figure 2.3 a) .

The schematic the graphene/hBN phototransistor devices is reported in Figure 2.4. The hBN/graphene heterostructure, of dimensions $L \times W = 20\ \mu m \times 10.4\ \mu m$, is deposited on a Ni bottom gate electrode and equipped with Cr/Au edge contacts. The bottom hBN layer, of thickness 67 nm, limits electrostatic doping to the range $\pm 0.15 \times 10^{12}\ cm^{-2}$. The thickness of the Ni layer is set to 12 nm to be semi transparent to mid-infrared light with a measured transmission of T = 10.9%.

2.3 Experimental set-up for transport measurements

In order to measure the dark current flowing through the phototransistors and further the photocurrent, we build up an experimental set-up for transport measurements at low temperature. For transport measurements, the gate, source, and drain contacts are connected to three electrodes linked to three probe outputs through BNC jack attached on the cryostat neck. The gate port and the source port are connected to a 6-digit resolved programmed DC source carried by the BilT system shown in (Figure 2.5 bottom right). In between the phototransistor devices and the DC source, a switch box (Figure 2.5 up) with a home-made DC block filter is used to switch on/off the voltage and protect the devices

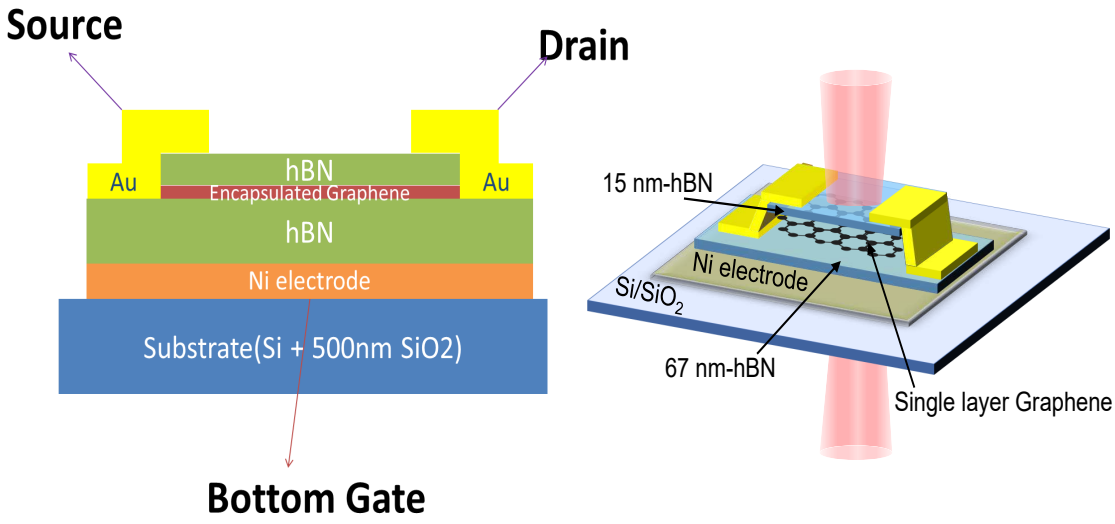

Fig. 2.4 *A schematic side view of the graphene/hBN phototransistor device, this device is composed of a hBN/graphene/hBN heterostructure, a semi-transparent Ni bottom gate and SiO_2/Si substrate.*

from external electrical surge. The drain contact is connected to a trans-impedance amplifier that converts the current into voltage with a high gain. It is permanently grounded, the bundled dark current and the photocurrent are magnified and split into two channels which are sent to a DC voltmeter device and a lock-in amplifier respectively. These types of equipment then send the data to the computer by the NI-GPIB card, the data acquisition is under control of Labview software.

We use a compact helium flow cryostat (Figure 2.5 bottom left) to control the temperature of the phototransistor samples from 4 K-300 K. The windows on the front and rear sides of the cryostat are transparent to the mid-infrared light. The BNC jacks at the neck are the extension from the internal cable which is for applying voltage.

2.4 The current properties in biased graphene

In the last decade, electronic transport in graphene has attracted much attention[118]. As an example, many studies have been devoted to the investigation of the unconventional behavior of carriers tunneling through an electrostatically-induced potential barrier in graphene. This behavior, which is called Klein tunneling [119], is due to the dispersion's conic shape. Further, theoretical and experimental studies on transport properties in graphene-based devices have shown that the current in biased graphene devices results from the interplay between Zener-Klein transport and nontunneling current. The Zener-

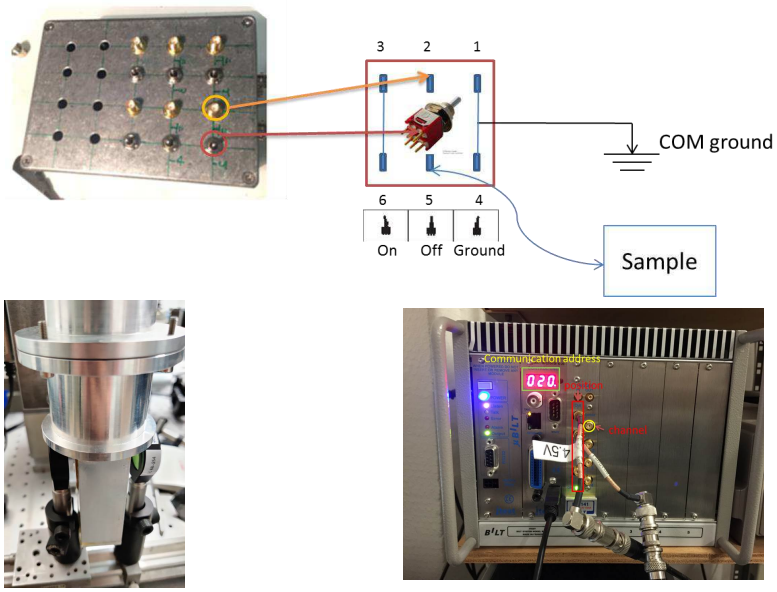

Fig. 2.5 *Up) The switch box is used to protect the sample from electrical surge or external static electricity, it has three shifts: on/off/ground, only the on-state can connect the DC source to the graphene/hBN phototransistor; off-state blocks the connection and ground the phototransistor; ground-state grounds all the components. Bottom) A photo of JANIS® cryostat between a set of aspheric lenses. BiLT system provides stable programmed DC outputs link to the gate, source and drain electrodes of the sample.*

Klein transport is the tunneling between different energy bands whereas the nontunneling current via defect scattering is associated with carriers that always remain in the same band.

Zener-Klein tunneling in graphene In graphene, due to its gapless band, an arbitrary small electric field is able to make electron carrier jumping from the valence band to the conductance band due to Zener tunneling. Moreover, due to the chiral nature of electron in graphene, there is a conservation of pseudo-spin in graphene. The importance of pseudo-spin is that it implies the absence of backscattering if an electron tries to backscatter in order to keep the pseudo-spin conservation as both $\mathbf{k}$ and σ needed to be reversed at the same time. The potential induced by impurity in graphene does not act in sub-lattice space and thus the pseudo-spin can not be reversed; this results in the backscattering to be impossible. The absence of backscatter makes it possible that the electron is transmitted and keeps the same direction while the momentum is reversed when it goes from a conductance band to a valence band. In other words, the carriers with the velocity parallel to the electric field experience Zener tunneling without being backscattered, a behavior that is markedly different from the one in conventional

semiconductors [120, 121, 122]. The physics is the same as for relativistic electrons tunneling through a barrier, a phenomenon called Klein tunneling. The Zener-Klein tunneling (ZKT) is illustrated in Figure 2.6 and describes the coexistence of a Zener tunneling and the Klein tunneling when an electric field is applied to the graphene.

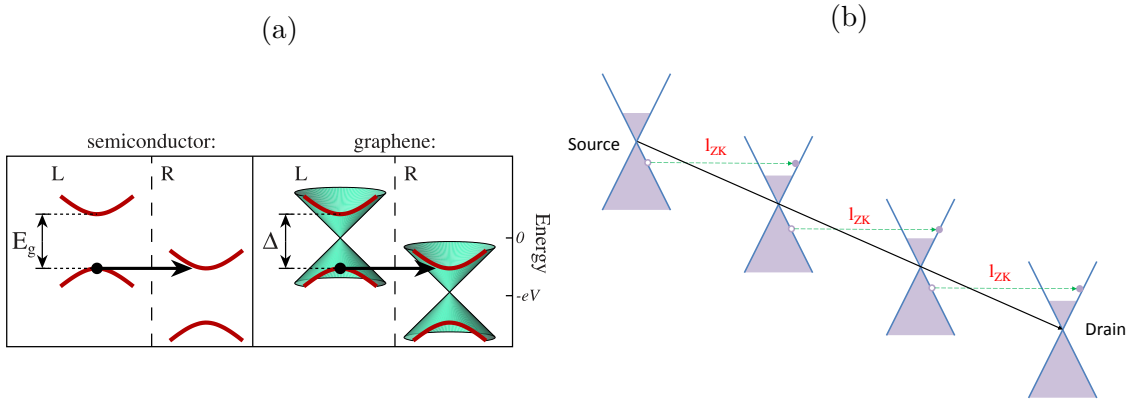

Fig. 2.6 *a): (Color lines) Bands of L and R contacts in a semiconductor and in graphene. The arrows represent the possible occurrence of Zener-Klein tunneling from [120]. b): Schematic of the Zener-Klein Tunneling process in a biased graphene channel from source to drain.*

Total current in graphene The total current in graphene-based devices includes the two distinct contributions that are the nontunneling current and the ZKT current. The nontunneling current, associated with carriers that always remain in the same band, is the usual intraband current via defect scattering, as well-known in conventional semiconductors. In graphene-based field-effect devices, the density of the carriers n can be varied by changing the gate voltage. For zero doping, there is no contribution from the nontunneling current as there are no free carriers and the current is entirely due to ZKT tunneling. It has been shown that the I-V characteristic is superlinear and is described by a power law $I \propto V^{\alpha}$ with $1 < \alpha \leq 1.5$. The exponent is higher when the mobility is lower. As soon as the graphene is doped, the ZKT current is no more dominant with respect to the nontunneling current, and for small bias, the I-V is essentially linear [120].

Charge puddles in graphene For a perfect graphene sheet free from impurities and disorder, the Fermi energy lies at the so-called 'Dirac point', where the density of electronic states vanishes. But in the inevitable presence of disorder, it has been shown that equally probable regions of electron-rich and hole-rich puddles exist. These puddles are responsible for the graphene's anomalous non-zero minimal conductivity at zero average carrier density[123]. These charge puddles in graphene have been observed microscopically

and directly by combined AFM-STM[124], and are well described by the self-consistent screening theory[125, 126]. These charge puddles induce a residual charge carrier density n_0 in graphene at the charge neutral point.

2.5 Dark current-bias characteristics of the graphene/hBN phototransistors

We start the investigation by measuring the transport properties of the graphene/hBN phototransistors with the aim to determine the mechanisms responsible for the dark current in these devices.

Low-bias resistance The resistance of the graphene/hBN phototransistors as a function of V_{GATE} at low bias (V_{DS} = 10 mV) and at low temperature (T = 4 K) is reported Figure 2.7. We observe that at large V_{GATE}, the resistance is low as the graphene layer is highly doped. It tends to the contact resistances that dominate over the resitance of the graphene channel. The contact resistance, observed at high positive V_{GATE}, is lower than the contact resistance observed at high negative V_{GATE}. Since it is known that 1D contact technique provides n-doped contacts, we deduce that positive V_{GATE} corresponds to the electron doping side and the negative V_{GATE} corresponds to the hole doping as indicated in Figure 2.7. As expected, close to zero, the resistance is maximum and this main peak corresponds to the charge neutrality point (CNP) of the graphene channel. The resistance at CNP is limited to charge puddles as discussed previously. Considering the contribution of both electrons and holes to the conductance of the graphene sheet, the total resistance of a device is expressed as:

$$\begin{aligned} R &= \frac{L}{W}\frac{1}{\sigma} + 2R_c \\ &= \frac{L}{W}\frac{1}{q(\mu_e n_e + \mu_h n_h)} + 2R_c \end{aligned} \tag{2.1}$$

with R_c the contact resistance of each electrodes and n the local carrier density:

$$n = \sqrt{(\frac{\epsilon_0 \epsilon_{BN} |V_{GATE} - V_{DP}|}{e_{BN} q})^2 + n_0^2}$$

with $\varepsilon_{BN} = 3.2$ the permittivity of the hBN layer, $e_{BN} = 67$ nm the bottom hBN thickness and n_0 the residual charge density induced by charge puddles. Using Equation(2.1) to fit the measured gate-dependent resistance of the phototransistor device (red curve in Figure 2.9), we extract a contact resistance of R_c = 650 Ω, a residual density n_0 of $\sim 4 \times 10^{14} cm^{-2}$ and an electron and hole mobility of 3.2 $m^2/(V \cdot s)$. The effect of

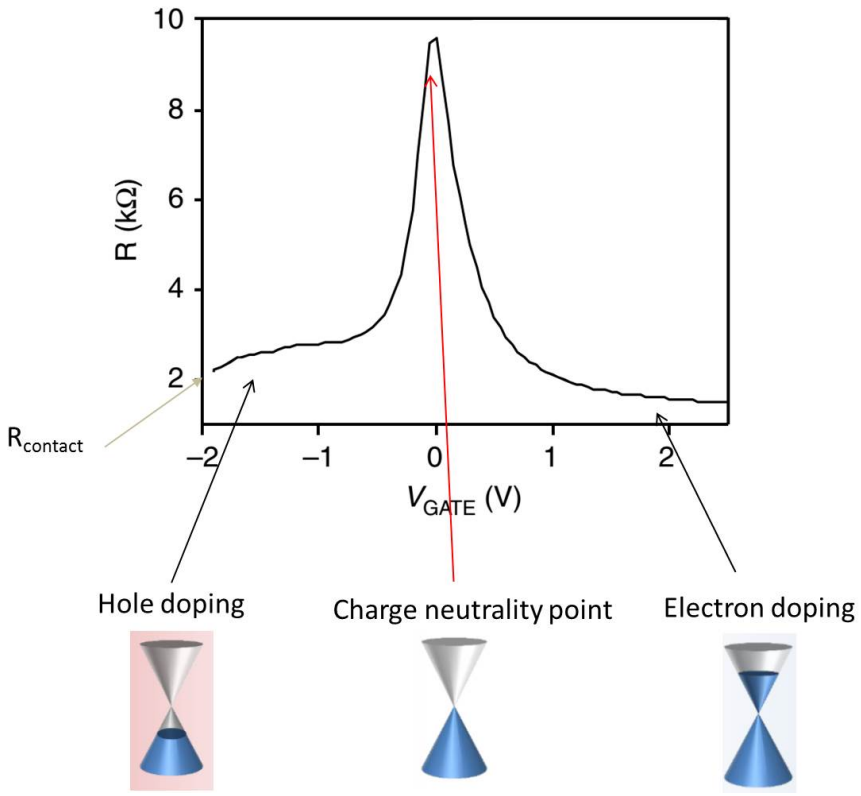

Fig. 2.7 *a) The resistance of the graphene/hBN phototransistors as a function of V_{GATE} at low bias (V_{DS} = 10 mV) and at low temperature (T = 4 K).*

the residual density n_0 on transport behavior of graphene is impactive near the Dirac point whereas it is negligible far away from Dirac point. Note that extracting the carrier mobility from Equation(2.1) is valid for gate induced net carrier density n larger than the residual charge carrier density n_0[127]. The gate capacitance, which mainly arises from the hBN dielectric capacitance with a negligible serial quantum capacitance, enables to access the Fermi energy range $E_F \sim \pm 80\ meV$ as shown in In Figure 2.8. The dashed lines represent the fluctuations of the Fermi-level energy induced by the residual carrier density $E_F = \hbar v_F \sqrt{\pi n_0} = 23.3\ meV$. Within this work, we will focus on the transport properties of carriers photogenerated at energies around 58 meV (corresponding to half the mid-infrared photon energy). The extraction of carrier mobility from gate-dependent resistance measurement is valid at energy close to the carrier photoexcitation energy of 58.5 meV since the fluctuations of the Fermi-level energy induced by residual carrier density than 23.3 meV.

Drain-doping compensation. To perform the dark-current bias characteristics, we take into account the drain doping effect. Indeed, as discussed above, it is essential in

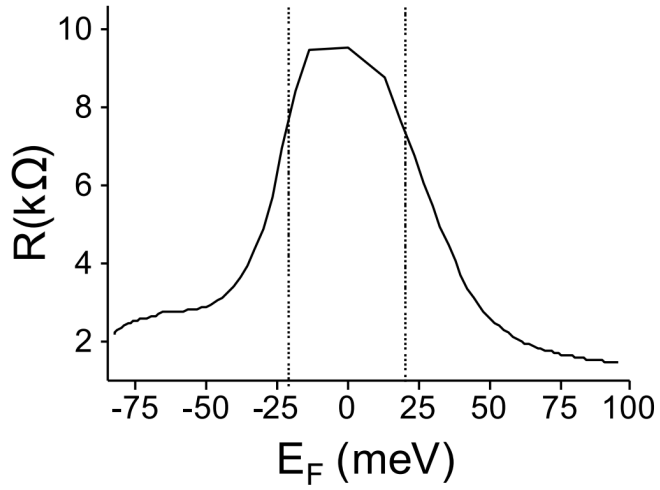

Fig. 2.8 *Low-bias resistance as a function of the Fermi-level energy in the graphene layer, calculated using the relation* $E_F = \hbar v_F \sqrt{\pi n}$ *with* $n = \sqrt{(C_g|V_{GATE}|/q)^2 + n_0^2}$.

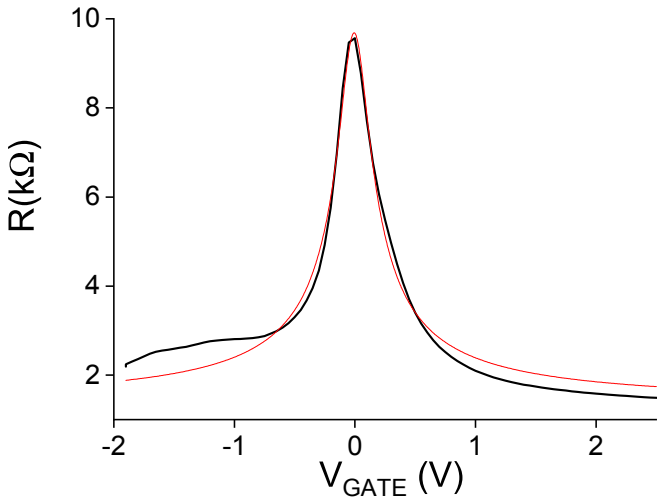

Fig. 2.9 *Low-bias resistance measured at 4 K and* $V_{DS} = 10$ *mV (black curve) and the fit using Equation*(2.1) *(red curve); a carrier mobility of 3.2* $m^2/(V \cdot s)$, *a residual carrier density of* $n_0 = 4 \times 10^{10}$ cm^{-2} *ascribed to residual charge puddles, and a contact resistance* $R_c = 650\ \Omega$ *are extracted from the fit.*

this experiment to keep a low (constant) doping so that the Fermi-level energy is weak compared to the incident photon energy allowing for interband absorption processes. To this end, we compensate for drain doping by a careful calibration of the gate voltage value at the CNP as a function of V_{DS}. Figure 2.10) shows the evolution of the dark current

as a function of V_{GATE} for V_{DS} ranging from -0.3 V to 0.3 V with a small interval of 20 mV. We found that the gate voltage at CNP evolves as $V_{CNP} = Const. + 0.56 V_{DS}$ where Const. is the gate voltage at CNP for $V_{DS} = 0$ and 0.56 is the linear coefficient (dashed line in Figure 2.10) [121]. This calibration needs to be done as the first experiment each time after cooling down the devices because the linear coefficient and intercept slight shift from the cooling-warming-cooling process day by day. This calibration is crucial to perform measurements of the current-bias and photocurrent-bias characteristics while keeping the phototransistors at CNP.

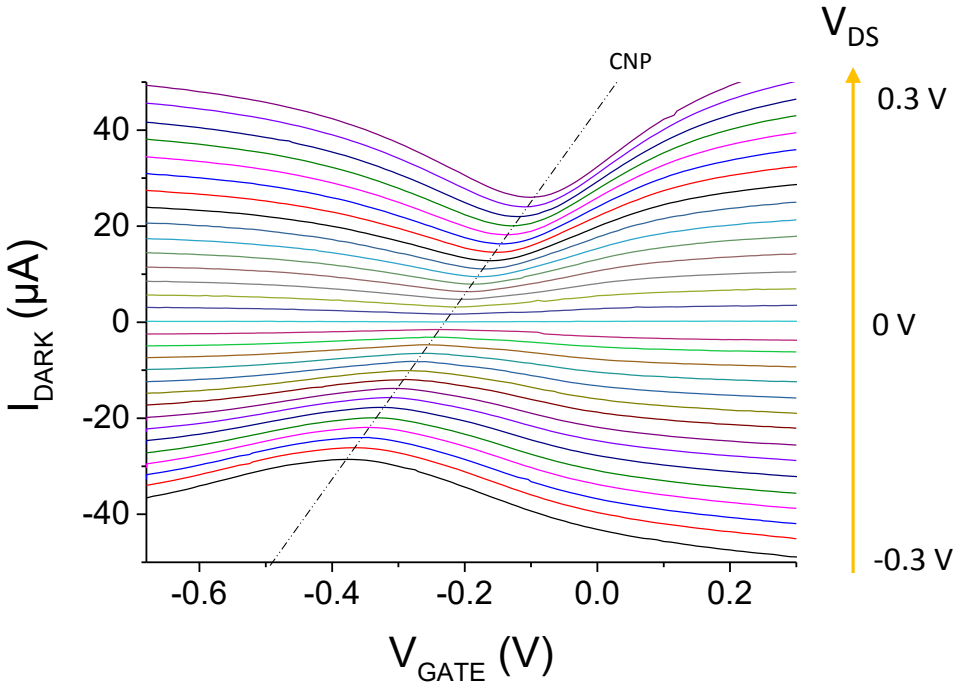

Fig. 2.10 *Evolution of the CNP in the graphene layer for V_{DS} ranging from -0.3 to 0.3 V due to the drain doping effect. The dashed line represents the linear evolution of $V_{CNP} = Const. + 0.56\ V_{DS}$*

Dark current-bias characteristics at CNP The dark current, I_{dark}, as a function of V^*_{DS} at the CNP and at 4 K is reported in Figure 2.11. V_{DS} is the total drop voltage at the two contacts and along the graphene channel. We deduce that the bias applied to the graphene channel only is given by $V^*_{DS} = V_{DS} - 2R_c I_{dark}$. The dark current is in the few hundreds of μA range. We observe that I_{dark} follows a superlinear bias dependence (black square symbols) in agreement with literature. The main contribution to the current in the graphene channel is ascribed to interband ZKT. Indeed, I_{dark} is well fitted a power

law, $I \propto V^{\alpha}$ with $\alpha = 1.3$ (red dashed curve) [121, 122]. At low bias a slight deviation is observed that we attribute to the finite charge puddles contribution. Note that the ZKT current is equivalent to an electrical pumping of non-equilibrium electron–hole pairs within the energy window $\epsilon < \pm\ 20meV$, as measured by noise thermometry[121]. In other words, the dc electric field acts as an electrical pumping of graphene/hBN heterostructures.

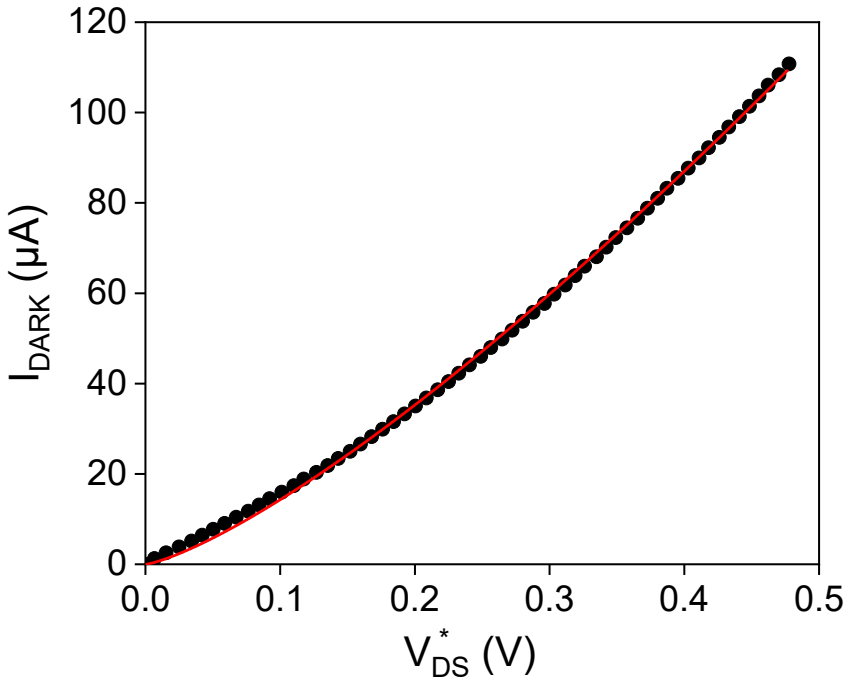

Fig. 2.11 *Dark current-bias characteristic (black square symbols) measured at 4 K and at the CNP (drain-doping effect is corrected). Calculated ZKT current with $\alpha = 1.3$ in red line.*

We further investigate the evolution of the dark current with the temperature. The range of temperature is set from T = 5 K to T = 250 K. We observe in Figure 2.12 that from 5 K to 20 K, the dominant mechanism involved in the current is ZKT. Indeed, we observe two similar superlinear curves likely in Figure 2.11. As the temperature is increased, the contribution of the intraband current, which evolves linearly with bias, is enhanced due to the increase of thermally excited non-equilibrium carriers. In return, ZKT contribution is decreasing due to Pauli blocking effect induced by the thermal distribution of carriers. As a result, the I_{dark}-V^*_{DS} curves evolve more and more linearly and the total current increases.

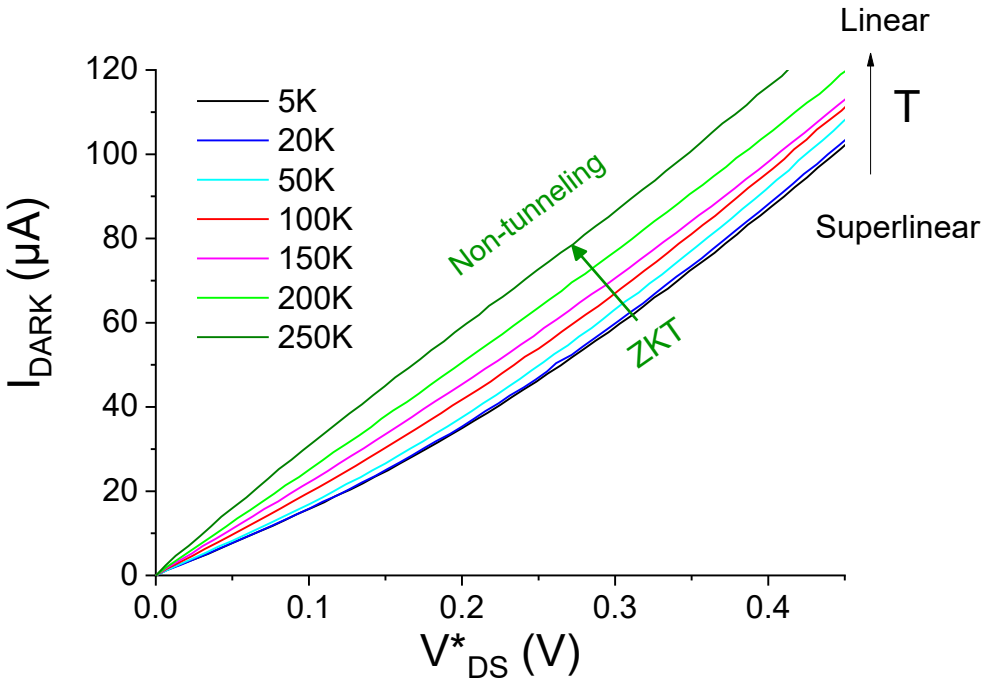

Fig. 2.12 *The dark current as the function of V^*_{DS} measured at different temperature ranging from $T = 5\ K$ to $T = 250\ K$.*

2.6 Conclusion

In this investigation of the transport properties of the graphene/hBN phototransistors, we have shown that at low temperature and at CNP, the current flowing in these devices is dominated by ZKT. Thus at finite bias, there are non-equilibrium electron-hole pairs within the energy window $\epsilon < \pm\, 20meV$ in the graphene channel. The dc bias acts as an electrical pumping of the graphene/hBN heterostructures.

Chapter 3

Photoresponse of graphene-hBN phototransistors under mid-infrared illumination

This chapter includes parts of our full article : Ultra-long carrier lifetime in neutral graphene-hBN van der Waals heterostructures under mid-infrared illumination, P. Huang et al., Nature Communications 11, 863 (2020) [97].

We have presented in the previous chapter, the investigation of the transport properties in graphene/hBN phototransistors. We found that the dark current, in the range of few tens of μA, is dominated by ZKT, which is equivalent to electrical pumping of non-equilibrium electron-hole pairs. In this chapter, we use photocurrent as an interesting probe to investigate the recombination process of non-equilibrium carriers created by optical pumping. The originality of our work is to investigate the recombination for photoexcited carriers at low density and energy in graphene/hBN heterostructures under dc bias control. Our optoelectronic experiment, which combines dc electric field and mid-infrared excitation, uniquely benchmarks the electrical and optical pumping of hBN/graphene heterostructures and provides a unique insight into their interplay.

The principle on which photocurrent generation relies is the conversion of absorbed photons into an electrical signal. Several different mechanisms by which this can be accomplished in graphene have been reported. These include photoconductive effect[128, 100], photovoltaic effect[107], photo-thermoelectric effect[129], bolometric effect[100, 130] and photogating effect[131]. In this work, we start our study by measuring the spatial profile of the photocurrent to identify the physical mechanism responsible for the photocurrent. Then we investigate successively three relevant photoconductive regimes: the linear

regime where both bias and optical power are low, the non-linear regimes where either power or bias exceed the linear photoconductive limit and the full photoconductive response including all the regimes.

In this chapter, we will first introduce the experimental set-up I have developed for phototransport measurements. Secondly, we will report on the spatial profile of the photocurrent and discuss on the mechanism involved in the photocurrent. Then, we will present the measurement of the photocurrent-bias characteristics in the three relevant photoconductive regimes.

3.1 Photo-transport in biased graphene/hBN phototransistor

3.1.1 Experimental set-up

To investigate the recombination for carriers at low photon energy and low fluence, we use a quasi-continuous mid-infrared laser excitation of wavelength $\lambda = 10.6$ µm (i.e. photon energy of 117 meV) and set graphene at charge neutrality point (CNP). This provides weak incident photon density and corresponds to photon energy between the Fermi-level fluctuations (~ 20 meV) and the optical phonons of graphene and hBN $\hbar\Omega =$ 170 - 200 meV. Thus, the absorption of the incident photons relies on interband process in the graphene layer. The optical setup is reported in Figure 3.1. It is made of three parts as below:

- **Power and polarization control of the incident light**: The quasi-continuous CO_2 laser delivers 10.6 µm wavelength light modulated at 5 kHz. The laser light firstly passes through a linear polarizer, this linear polarizer is able to knob the maximum power of incidence light, the second optical element is either a linear polarizer or a wave plate, it can rectify the polarization orientation to meet needs of the experiment. After that, the beam is split by a wedged ZnSe window into two arms. All the ZnSe windows in the optical setup except the cryostat are wedged to avoid the specular reflection back into the laser cavity, which can lead to instability.

- **Beam collimation and expansion**: Then, one arm is expanded to a diameter of 22mm for further focusing at the diffraction limit, the other arm is used to record the fluctuation of laser power in real-time.

- **Focus and collection**: In the transmission arm, a set of aspheric Germanium lenses are used to focus the beam onto the phototransistor-based device. The optical beam transmitted through the phototransistor device is collected by a mid-infrared photovoltaic multiple junction detector.

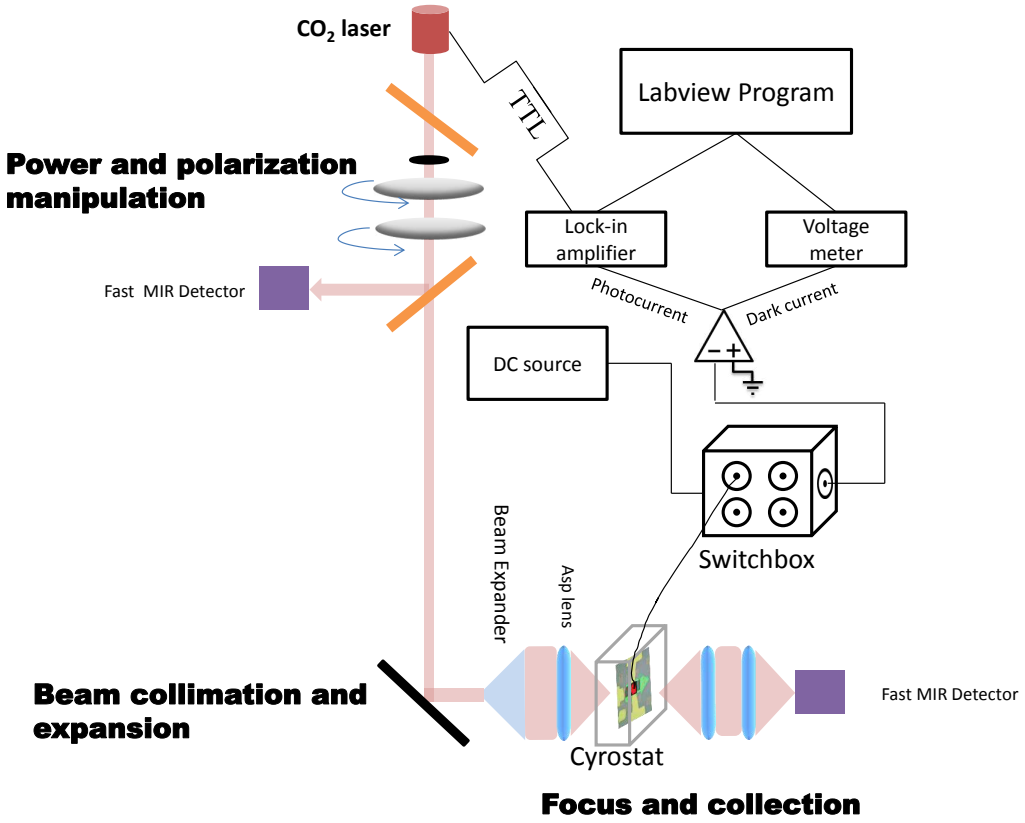

Fig. 3.1 *Schematic of phototransport experimental setup. The optical part includes the power and polarization light control, the beam collimation and expansion and the light focusing and detection; The electrical part contains connections and types of equipment for recording both the dark current and the photocurrent.*

The photocurrent is modulated at the laser light frequency modulation (5 kHz). The photocurrent and the dark current are transmitted to a trans-impedance amplifier connected to a lock-in amplifier synchronized to the laser modulation for recording the photocurrent and to a Keithley 2700 voltage meter for recording the dark current. In addition, we use two other lock-in amplifiers to record the signals detected by the photodetector used to measure the optical beam transmitted by the phototransistor device and by the photodetector used in the arm for power calibration.

3.1.2 Spatial profile of the photocurrent

Using this experimental set-up, we investigate the photoresponse of the graphene/hBN transistors at low temperature T = 4 K. We start by probing the spatial profile of the photocurrent to get insight on the physical mechanisms involved in the photoresponse.

The laser spot is focused on the device with a waist, $w_0 = 10.6$ µm, determined using usual knife-edge techniques. The sample of dimensions $10.4 \times 20 \mu m^2$ is moved using a motorized translation stage along the direction of the graphene channel and the photocurrent is measured for each sample position. For this experiment, we keep the chemical potential of the graphene at the CNP.

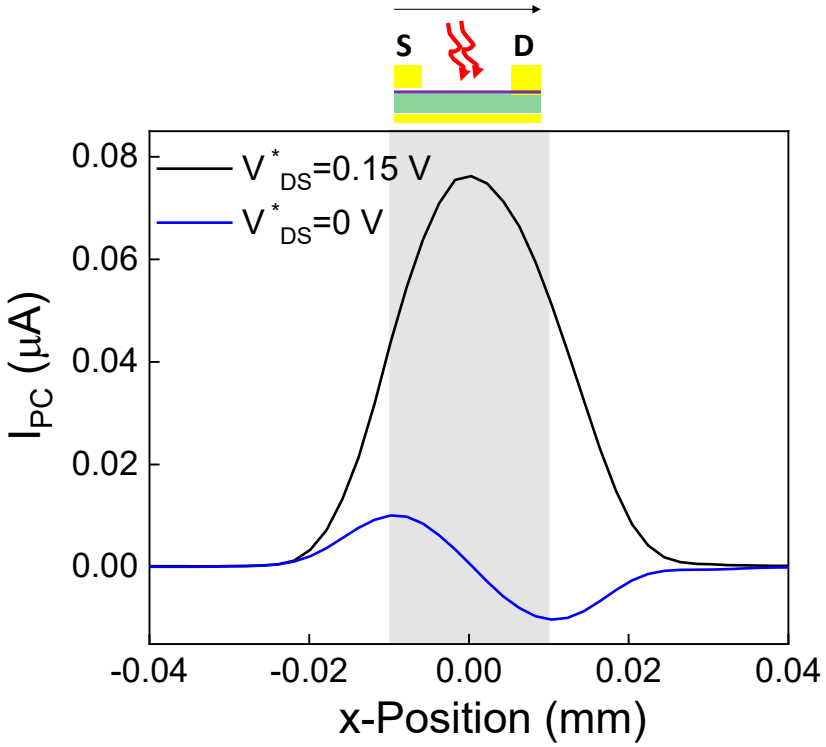

Fig. 3.2 *Photocurrent line scan profiles of the graphene/hBN heterostructure along the graphene channel for $V^*_{DS} = 0$ V (blue line) and $V^*_{DS} = 0.15$ V (black line) under continuous light excitation at 10.6* µm *wavelength measured at 4 K and at the CNP. The laser spot diameter is focused on the device with a waist of 21.2* µm *quasi-matching sample length. The gray shadow area represents the graphene-based sample.*

Figure 3.2 shows the spatial distribution of the photocurrent along the channel length at the CNP for V^*_{DS}=0 V (blue curve) and $V^*_{DS} = 0.15$ V (black curve). Note that, as discussed in chapter 2, due to the contact resistances, the potential drop along the graphene channel, V^*_{DS}, is distinct from the applied source-drain voltage. We calculate V^*_{DS} using the contact resistance values and the measured dark current using the expression $V^*_{DS} = V_{DS} - 2R_c I_{dark}$. At zero source-drain voltage, we observe that the photocurrent is antisymmetric with respect to the sample length with extrema in the immediate vicinity of the leads and a node at the center. It can be assigned to photocarriers generated at the contact junctions that are accelerated by built-in electric fields at the contact. Indeed,

due to the work function mismatch between graphene and the contact metal, a built-in electric field is induced in the regions close to the metallic leads (over typically 1 µm) owing to the band-bending. This photocurrent created by illuminating the contact regions can originate from both photovoltaic and thermoelectric effects[132]. By contrast, we observe a very distinct photoresponse at finite source-drain bias. Indeed, the photocurrent is symmetric with a maximum at the sample center. It has the same polarity as the dark current. Moreover, if we focus on the magnitude of this photocurrent, its maximum value is seven times larger than the maxima measured in the unbiased condition.

To go further, we evaluate the expected spatial profile of the photocurrent for a constant photoresponse along the graphene channel and considering the large size of the laser beam (diameter 21.2 µm). To this aim, we calculate the convolution (red curve in Figure 3.3) of a constant photoresponse along the graphene channel, given by a rectangular function $\prod(L)$ with the gaussian profile of the laser beam given by:

$$P_{inc} = P_0 e^{-\frac{x^2+y^2}{2\sigma^2}}$$

(with $\sigma = 5.3$ µm). We observe in Figure 3.3 a good agreement without any adjustable parameters between the normalized spatial profile of the measured photocurrent (black curve) and the convolution product (red curve). Thus, we conclude that the photoresponse at finite V^*_{DS} is constant along the graphene channel.

3.1.3 Competing mechanisms for photocurrent

Let us now discuss on the competing mechanisms responsible for this photocurrent at finite source-drain bias in graphene [100]. When a source-drain bias is applied, the uniform doping can be rendered asymmetric with a gradually effective doping along the graphene channel leading to the existence of thermoelectric effects in graphene. However, since only a weak gradient of temperature is induced by the large laser spot, the photocurrent contribution due to thermoelectric effect is expected to be very weak. Moreover, it has opposite in sign to the dark current. Thus, the thermoelectric effect could not be responsible for the photocurrent we measured at finite source-drain voltage. As well, the transport change produced by heating associated with the incident electromagnetic radiation produces a bolometric current. However, bolometric current shows a vanishing contribution at low electrostatic doping, i.e. at CNP. Moreover, it is opposite in sign to the dark current due to the decrease of the mobility with increasing temperature. Also, the bolometric effect could not be responsible for the photocurrent we measured at finite source-drain voltage. As a result, we attribute the dominating mechanism involved in the photocurrent measured at the CNP and finite source-drain bias to the photoconductive

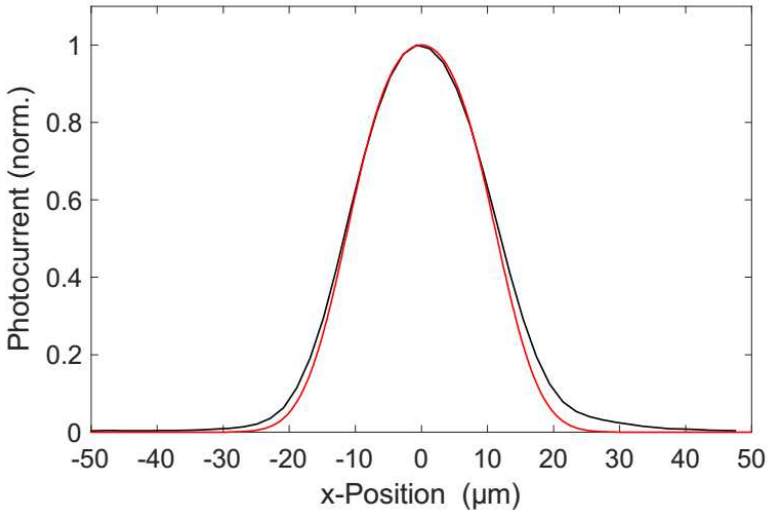

Fig. 3.3 *Normalized photocurrent line scan profile of the graphene/hBN heterostructure along the graphene channel for V^*_{DS}=0.15 V (black line) measured at 4 K and CNP. The red curve is the normalized convolution of an uniform photoresponse along the graphene channel given by the convolution of a rectangular function with the gaussian profile of the laser beam P_{inc}.*

effect. This photoconductive effect relies on the acceleration of photoexcited electrons and holes in opposite directions by an applied electric field. The photoexcited electrons and holes are created by the interband absorption of the incident mid-infrared photons. Indeed, interband absorption is allowed since the chemical potential in graphene is lower than half the photon energy.

Figure 3.4 shows the gate voltage dependence of the photocurrent for an illumination at the channel center. We show a sharp peak at charge neutrality (half-width $\sim$ 33 meV), narrower than the resistance peak itself (Figure 2.7). This dominates the photoresponse in the full doping range, in particular the negative photothermal response at large doping (at $|V_{GATE}| > 0.24$ V) relying on bolometric effects. Thus, we observe that this photocurrent that relies on the photoconductive effect is strongly sensitive to electrostatic doping as expected due to Pauli blocking effect. It constitutes the signal of interest in this work. Although observed in previous photo-transport experiments[130, 133, 134], these were in a regime of high-photon energy ($>$ 0.7 eV).

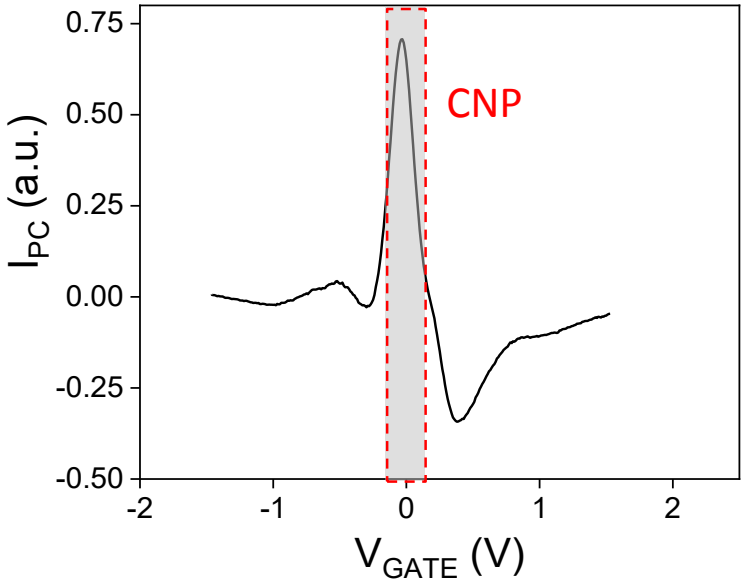

Fig. 3.4 *Photocurrent as a function of gate voltage for an illumination at the center of the channel and $V^*_{DS} = 0.1$ V. It shows a narrow peak with a half-width at half maximum of $\sim$ 33 meV. The gray shadow area represents gate range of interest in this work.*

In the following, we investigate successively three relevant photoconductive regimes:

- The linear regime where both bias and optical power are low.
- The non-linear regimes where either power or bias exceed the linear photoconductive limit.
- The full photoconductive response including all the regimes.

3.2 Linear photoresponse in biased graphene/hBN phototransistor

3.2.1 Photocurrent–bias characteristics

Figure 3.5 shows the photocurrent–bias characteristics at low-bias and low-incident mid-infrared power. The polarization of the incident light is linear, parallel to the graphene channel and the dc electric field. We observe a linear dependence of the photocurrent with bias over the optical power range from 0.1 to 1 mW. As the incident power is increased, the photocurrent is increased. These behaviours are fully expected for a photoconduction

process[130]. Note that the photocurrent reaches the μA range.

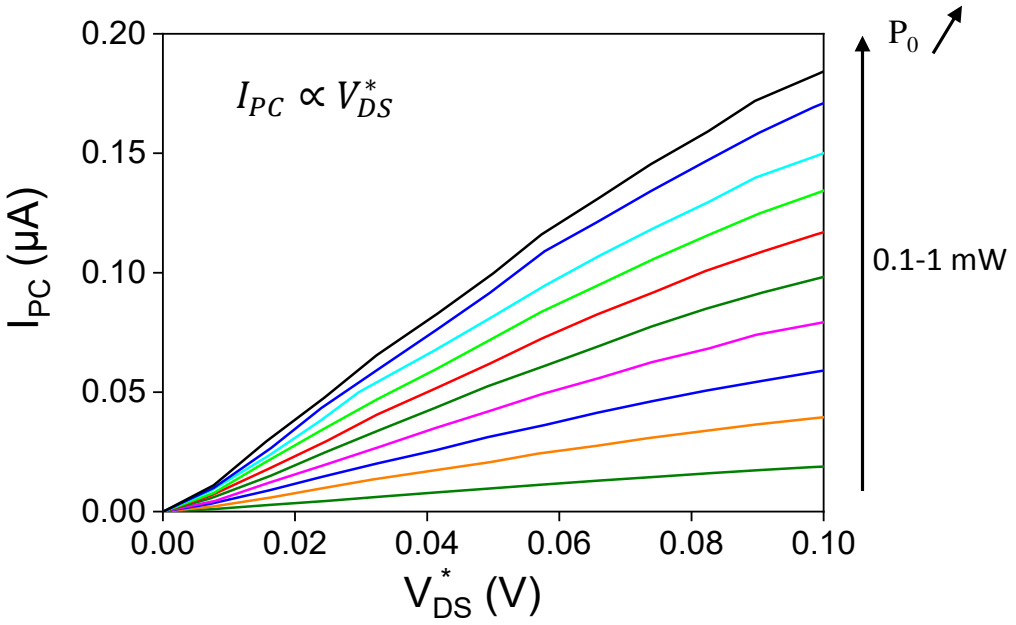

Fig. 3.5 *Linear photocurrent–bias characteristics measured at low bias for low incident power ranging from 0.1 to 1 mW. The measurements are performed at the CNP for a temperature of 4 K. The polarization of the incident light is linear, parallel to the dc electric field.*

3.2.2 Photoexcited carrier density

From these measurements and electrical characterization, we can extract the photoexcited carrier density using the drift-diffusion model and the charge conservation principle. The photons absorbed by the graphene layer generate electron-hole pairs at a rate G_0, and this process leads to an excess electron density n_e^* and hole density n_h^*. R is the recombination rate of the excess charges. The dynamic and transport of the charge carriers follow the equations :

$$\begin{aligned} \frac{\partial n_e^*}{\partial t} - \frac{1}{e}\nabla j_{pc_e} &= G_0 - R \\ \frac{\partial n_h^*}{\partial t} - \frac{1}{e}\nabla j_{pc_h} &= G_0 - R \end{aligned} \tag{3.1}$$

where the electrons J_{pc_e} and the hole J_{pc_h} current densities are:

$$\begin{aligned} J_{pc_e} &= q\mu_e n_e^* E_{DS} + qD_e \nabla n_e^* \\ J_{pc_h} &= q\mu_h p n_h^* E_{DS} + qD_h \nabla n_h^* \end{aligned} \tag{3.2}$$

μ and D are denoted as the mobilities and diffusion coefficients of each carrier types, and E_{DS} is the applied electric field to the graphene channel. Since the illumination is uniform, the contribution of diffusion is negligible. Thus, the total photocurrent that circulates within the structure is given by

$$I_{pc} = J_{pc}W = q(\mu_e n_e^* + \mu_h n_h^*)E_{DS}W$$

Thus, we can extract the photoexcited carrier density $n^* = n_e^* + n_h^*$ in this stationary regime at the CNP using $\mu_e = \mu_h = 3.2\ m^2/(V \cdot s)$ and $E_{DS} = V_{DS}^*/L$. The photoexcited carrier density as a function of the incident optical power is reported in Figure 3.6. We observe that it evolves from $< 0.1 \times 10^9$ to $\sim \ 0.7 \times 10^9\ cm^{-2}$. Note that the photoinduced electron and hole densities are significantly higher than the thermal electron and hole densities ($1.4 \times 10^7\ cm^{-2}$) in ideal intrinsic graphene at T = 4 K. However, it remains relatively weak compared to the residual carrier density. To attain insight into the efficiency of the carriers recombination process, we estimate the carrier lifetime from the photocarrier densities and the light excitation conditions[130].

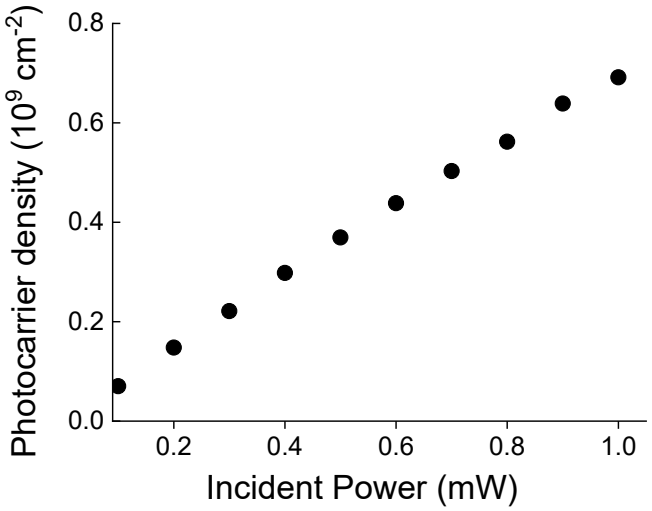

Fig. 3.6 *Photo-carrier density as the function of incident power in this low-bias regime extracted from photocurrent measurements and electrical characterization, we assume the carrier multiplication effect (M = 1). The carrier lifetime Figure 3.8 is independant to the increasing tendency of photo-carrier density.*

3.2.3 Carrier lifetime

Considering that along the graphene channel, the electric field is constant, then the Equation(3.1) reduce to:

$$\frac{dn_e^*}{dt} = -\frac{n_e^*}{\tau} + G_0$$
$$\frac{dn_h^*}{dt} = -\frac{n_h^*}{\tau} + G_0$$

with $G_0 = \alpha_0 \frac{P_o}{\hbar\omega S_{laser}} M$, where the M represents the factor of multiplication carrier. As the illumination involves continuous wave excitation, the system is under steady-state regime and the photocarriers density is given by:

$$n_e^* = n_h^* = G_0\tau = \frac{\alpha_0 P_o M \tau}{\hbar\omega S_{laser}}$$

where α_0 is the light absorption, S_{laser} the area of the laser spot, $\hbar\omega$ is the photon energy, τ is a phenomenological carrier lifetime. M is a carrier multiplication factor resulting from impact ionization effect that can lead to the creation of additional carriers contributing to the photocurrent[135]. P_o is the laser power incident on the sample. P_o is lower than the incident optical power P_{inc} by a factor 0.63 due to the larger size of the optical Gaussian beam with respect to the sample dimension. In our experimental conditions, M is predicted to be close to unity. Indeed Jago *et al.* have calculated that M is typically < 1.2 when photocarriers, with initial energy of 0.65 eV, evolve in a dc electric field[128]. Moreover, Tomadin *et al.* have predicted that M tends to unity when pump photon energy is lowered below 0.5 eV in undoped graphene sample[136]. The light absorption by the graphene layer α_0 is calculated considering the layered geometry of our device. We take into account the thickness and dielectric constants of each layer to find the electric field in the graphene plane. For this purpose, we use transfer-matrix method developed by Simon Messelot, PhD in my research group, to calculate the electric field distribution within the layered structure. The light wavelength is 10.6 µm, the thicknesses of the top and bottom hBN dielectric films are $\sim$ 67 nm and 15 nm respectively and the dielectric constant of hBN is 3.2. We have independently characterized the transmission of thin Ni films deposited on SiO_2/Si substrates to extract the dielectric constant of the 12 nm-thick Ni film and found $\varepsilon_{NI} = 9.06 + 37.87i$, which is consistent with M. A. Ordal *et al.*[137]. Figure 3.7 shows the calculated spatial profile of the electric field E normalized by the incident electric field E_0 along the layered structure. The electric field at the graphene plane is $E_{Graphene} = 0.217E_0$. Then the graphene absorption is given by $\alpha_0 = A(E_t/E_0)^2 = 0.11\%$ where A = 2.3% is the interband absorption in free space of a monolayer graphene. We verify that the transmitted light through the device and the semi-transparent Ni electrode is proportional to the incident optical power, indicating no

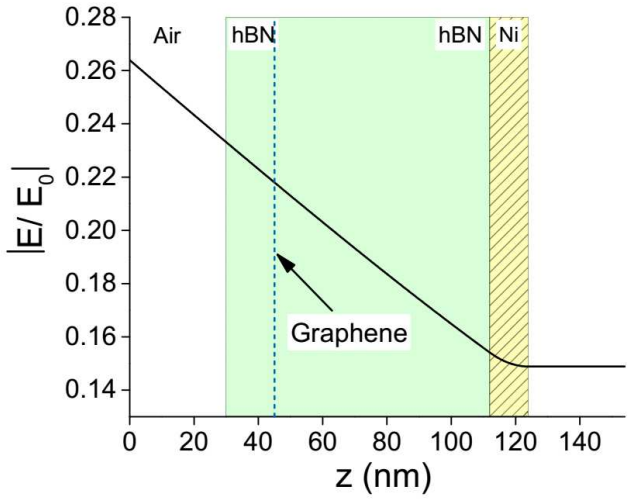

Fig. 3.7 *Calculated electric field distribution along the stack of the hBN/graphene heterostructure using a transfer-matrix method developed by S. Messelot. The dashed line represents the graphene layer.*

absorption saturation effect.

Figure 3.8 shows the carrier recombination time (denoted carrier lifetime) extracted from this analysis, assuming negligible carrier multiplication effect ($M = 1$). We report on an unprecedented carrier lifetime of > 30 ps ($\sim$35 ps in Figure 3.8), at low incident optical power and low bias, which is the main result of our work. This value is consistent with the slowing down of relaxation processes observed for low-energy carriers in graphene using pump–probe experiments, attributed to inefficient scattering via optical phonon emission[109, 110]. In contrast to pump–probe experiments, which directly measure the dynamics of photoexcited carriers but with no direct distinction between relaxation and recombination processes, our experiment provides an estimation but singles out the recombination times of the photoexcited carriers. Indeed, only interband processes where electron and hole recombine are involved in the carrier lifetime τ since the intraband processes that relax the photocarriers within their respective band do not suppress the photocurrent.

Note that the carrier recombination times reported in Figure 3.8 are underestimated if inhomogeneities of the Fermi level within the sample area due to charge puddles are considered since Pauli blocking reduces the effective absorbing area. Further, even if some carriers in the puddle region are taken into account in the calculation, the carrier lifetime still remains underestimated, as the mobility in the puddle region is lower than that in the linear region[138].

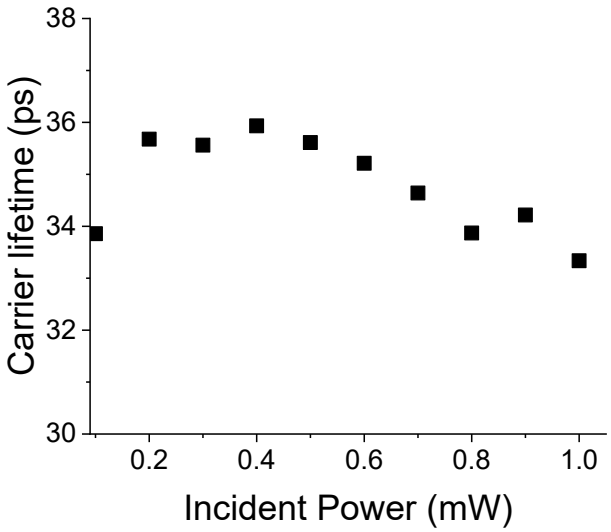

Fig. 3.8 *Carrier lifetime as a function of the incident power in this low-bias regime extracted from photocurrent measurements and electrical characterization and assuming negligible carrier multiplication effect ($M = 1$). Considering the layered geometry of our device and the size of the sample, the absorbed power $P_{abs} = 6.8686 \times 10^{-4} \times P_{inc}$.*

This raises the question of the physical mechanism responsible for this very slow recombination of the photoexcited carriers. Recombination mechanisms of hot carriers in graphene usually involve the interplay between carrier–carrier and carrier–phonon scatterings. However, in this regime of low power, low bias and low temperature, scatterings via optical phonon in graphene and via coupling with hyperbolic phonon in hBN are strongly suppressed by Pauli blocking, as $\hbar\omega$ is well below their energy band 170–200 meV. With $\hbar\omega = 117$ meV, one cannot rule out scattering by the lower 95–100 meV HPhP branch, a mechanism which is expected to be weak[139]. Acoustic phonon scattering cannot cause recombination because energy and momentum would not be conserved for interband transitions[132]. Indeed, the acoustic phonon mode, having an energy $\omega_q = c_s q$ with c_s smaller than the graphene band velocity v_F, does not provide a possible channel for interband transitions, which requires an energy greater than vFq. Emission of acoustic phonons is therefore only possible through intraband transitions[140]. The momentum mismatch issue can be circumvented by impurity-assisted phonon supercollisions[141, 142]; however, this mechanism is suppressed in high-mobility graphene. Radiative emission is very slow in graphene, typically at nanosecond timescale[143]. Consequently, at low-bias and low-photoexcited carrier density, interband Coulomb scattering (Auger recombina-

tion) is expected to be the remaining scattering mechanism involved in the recombination of non-equilibrium carriers (i.e. photoinduced carriers in excess to the dark ones) in hBN/graphene/hBN transistors.

The interband Coulomb scattering (Auger recombination) in graphene are depicted Figure 3.9a. They involve two distinct processes of electron-hole recombination. One occurs from conduction band: an electron with initial momentum k_1 in conduction band scatters off another electron in conduction band with initial momentum k_2, the electron(k_1) experiences an intraband transition, its momentum results in $k_1 + Q$ according to the conservation of momentum, and another electron(k_2) transits from conduction band to the valence band and its momentum results in $k_2 - Q$. The other process via pair of holes occurs from valence band in a mirrored way (see the CVVV process in Figure 3.9a).

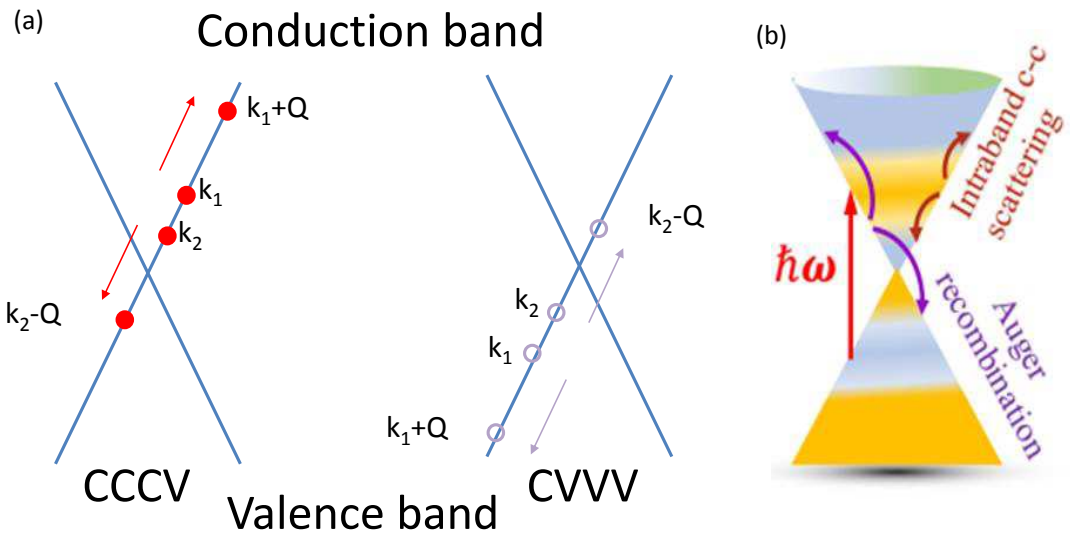

Fig. 3.9 *Sketch of electron-hole recombination in graphene from Coulomb scattering (Auger recombination). The two processes shown are symmetric to each other. b) Sketch of the dominating relaxation and recombination processes under low pumping and low bias in graphene/hBN phototransitors.*

Because of the requirement of energy and momentum conservation, the phase space of Coulomb scattering is restricted. According to the calculation reported by Farhan Rana [144] (see Figure 3.10), the recombination time (blue solid line) equals few tens of picoseconds when the electron (hole) density ranges from $10^8 - 10^9$ cm^{-2}. This theoretical work validates our assumption that the physical mechanism responsible for this very slow

recombination of the photoexcited carriers in graphene we extracted, is the interband Coulomb scattering. As well as, Alymov *et al.* have also predicted interband Coulomb scattering times for carriers close to the Dirac point in graphene of few to few tens of picoseconds range [143] . Note that we attribute the independence of the carrier lifetime to the incident optical power observed in Figure 3.8 to Auger recombination processes assisted by the large density of charges (Zener–Klein and residual carriers), which exceed the photoexcited carrier density at low incident power. As a result, the total charge density involved in the Auger recombination process remains essentially constant from 0.1 to 1 mW incident optical power.

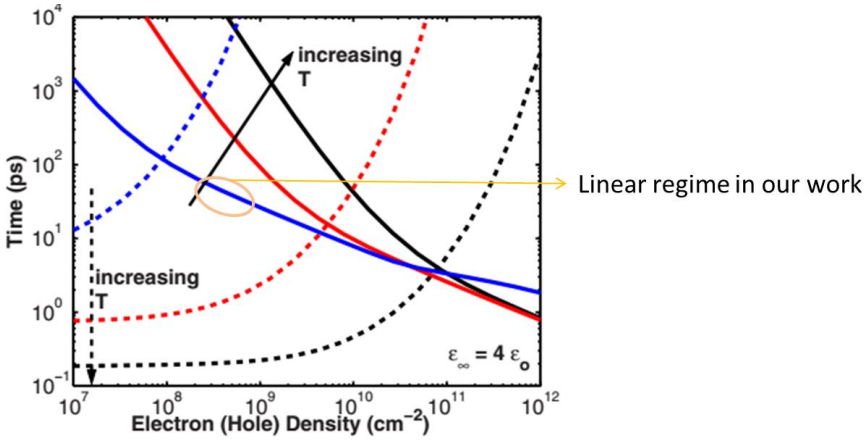

Fig. 3.10 *Figure extracted from [144], blue solid line shows the recombination time as the function of electron (hole) density at $T = 10$ K, assuming silicon dioxide on both sides of the graphene layer.*

3.2.4 Responsivity

The responsivity and internal quantum efficiency of the graphene/hBN heterostructure transistor are shown in Figure 3.11. Despite the high carrier mobility and the long carrier lifetime in the encapsulated graphene layer, the responsivity and internal quantum efficiency (IQE) are relatively low compared to other reported mid-infrared graphene detectors[145]. The main reason is the weak photoconductive gain due to the long carrier transit time, in the nanosecond range, compared to the carrier lifetime, which results from the large drain-source distance of 20 µm. This length was set here to match the large diffraction-limited spot size for mid-infrared light. However, advanced design such as antenna-assisted graphene detector, where optical antennas are used as both light-harvesting components and electrodes, can be implemented to greatly enhance simultaneously light-absorption and carrier-collection efficiency[146].

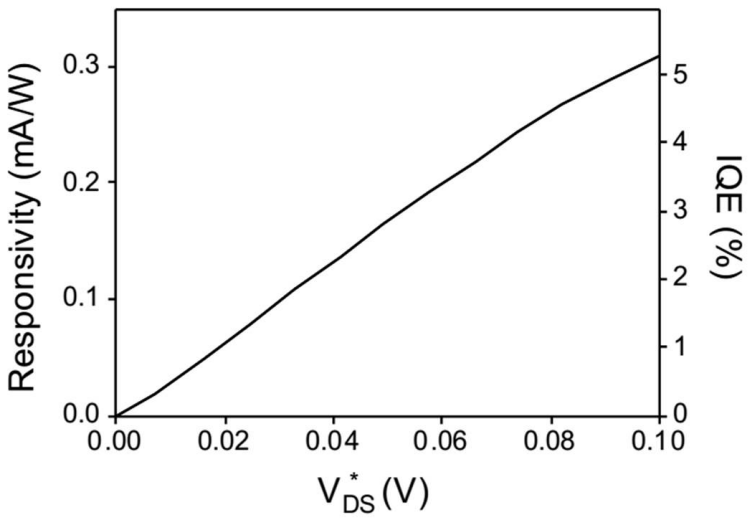

Fig. 3.11 *Responsivity and internal quantum efficiency (IQE) of the graphene/hBN phototransistor as a function of* V^*_{DS}.

3.2.5 Influence of light polarization

For further insight into many-body Coulomb scattering, we take advantage of both the asymmetry of the photocurrent induced by the dc electric field and the asymmetry of the initial distribution of photoexcited carriers in k-space induced by the polarization of the incident light. Indeed, illuminating graphene with linearly polarized radiation provides an initial anisotropic distribution of photoexcited carriers in k-space with two lobes in the direction perpendicular to the light polarization.

Figure 3.12 shows the ratio between the photocurrent measured when light polarization is perpendicular to the dc electric field over the photocurrent when light polarization is parallel to the dc electric field, indicating that the anisotropy of the photoexcited carrier distribution is not fully relaxed in this steady-state regime. This anisotropy is consistent with expectations even when considering that Coulomb scattering is predominantly collinear in graphene. As a matter of fact, non-collinear Coulomb scattering has been reported with a characteristic time of 2 ps[147]. Being much smaller than our recombination time, the polarization effect at the few percent scale agrees with our observation. The photocurrent and therefore the carrier lifetime is larger for perpendicular polarization, i.e. when the lobes of the photoexcited carriers are parallel to the shift induced by the dc electric field with respect to the Dirac point. In this configuration, Auger recombination processes are expected to be less efficient due to Pauli blocking by dark carriers, whose density is maximized in the direction of the dc electric field.

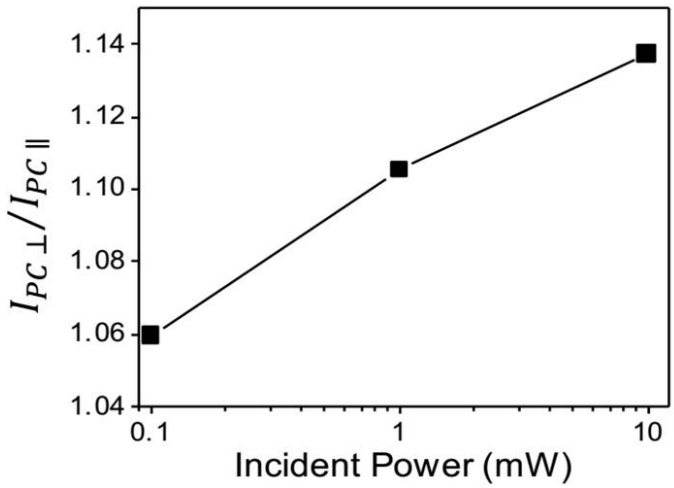

Fig. 3.12 *Ratio between the photocurrent measured when light polarization is perpendicular to the dc electric field over the photocurrent when light polarization is parallel to the dc electric field as a function of* P_{inc}.

In the following, we mainly use light polarization parallel to the dc electric field to minimize the interaction of photoexcited carriers with the out-of-equilibrium electron–hole pairs created by Zener–Klein tunneling.

3.3 Nonlinear photoresponses in biased graphene/hBN phototransistor

3.3.1 Non-linear regime in V^*_{DS}

We now turn to non-linear regimes to further explore the hBN/graphene heterostructure-based devices. Figure 3.13 shows the photocurrent as a function of V^*_{DS} at low-incident optical power. We observe strong deviations from the $I_{PC} \propto V^*_{DS}$ for $V^*_{DS} \geq$0.1 V leading even to a negative differential photoconductance for $V^*_{DS} \geq$0.17 V, independently of the optical power in the range P_{inc} = 0.1–1 mW. The contrasted behavior between low bias and high bias cannot be described by the usual photoconductive effects[130] and evidences the rise of an additional recombination channel for photoexcited carriers. The photocurrent drop, by more than a factor two, suggests that this additional recombination channel is highly efficient with a characteristic time significantly shorter than the low-bias recombination time of $\sim$ 30 ps. To get a more accurate determination of the voltage threshold for the ignition of this additional channel, we plot in Figure 3.14 the difference ΔI_{PC} between the extrapolated linear regime $I_{PC} = aP_{inc}V^*_{DS}$ (dashed red line in Figure 3.13) and the measured photocurrent. The obtained $\Delta I_{PC}(V^*_{DS})$ reveal a threshold at a voltage

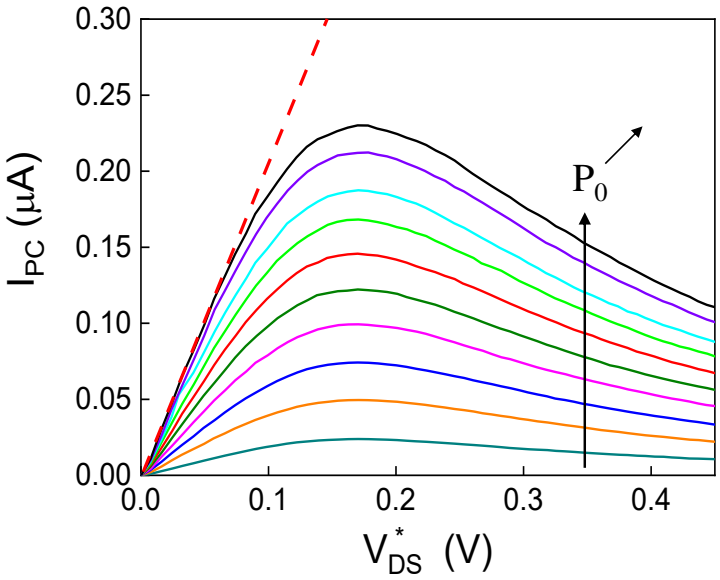

Fig. 3.13 *Graphene/hBN heterostructure phototransistor in the non-linear regime, the photocurrent as a function of bias beyond the linear regime.*

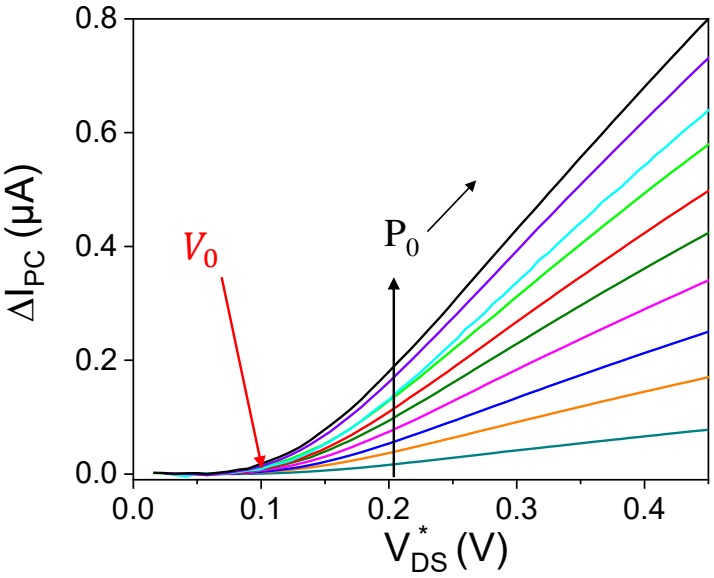

Fig. 3.14 *Difference ΔI_{PC} between the photocurrent expected for photoconductive regime at large bias (dashed line in a) and the measured photocurrent as a function of V^*_{DS} for P_{inc} ranging from 0.1 to 10 mW clearly showing a threshold behavior.*

bias $V_{DS}^{*} = V_0 \leq 0.1\ V$, indicating the switching of the additional recombination channel.

3.3.2 Emission of Hyperbolic Phonon Polaritons

The value of V_0, observed in two distinct samples, points to an activation energy close to energy of the upper HPhP band ($\hbar\Omega_{II}$ = 170–200 meV) with $eV_0 \sim (\hbar\Omega_{II} - \hbar\omega)$ ≈54–84 meV. We therefore attribute the additional recombination channel to the emission of HPhPs in hBN layer[148], consistently with previous works on similar hBN-encapsulated graphene where picosecond HPhP cooling times were reported[112, 149]. In particular, a similar threshold was observed in noise thermometric experiments using samples of similar mobility[121]. h-BN layer supports large number of propagating HPhP modes (electromagnetic modes originating in the coupling of photons to optical phonons) that can be very efficiently coupled to the carriers in graphene via near-field coupling (i.e. super-Planckian coupling). In [148], Principi *et al.* microscopically investigate how hot carriers in graphene can transfer their energy to the phonon polaritons in hBN in hBN/graphene/hBN heterostructures. They show that, in a van der Waals stack, where the distance of separation δ between hot carriers in graphene and HPP in hBN is lower than the thermal wavelength d_T ($\delta \ll d_T = \hbar c/(k_B) = 4 \times 10^{-4} m$ (T = 5 K)), the radiative heat transfer is no longer controlled by Stefen-Boltzmann law and it can exceed the blackbody limit.

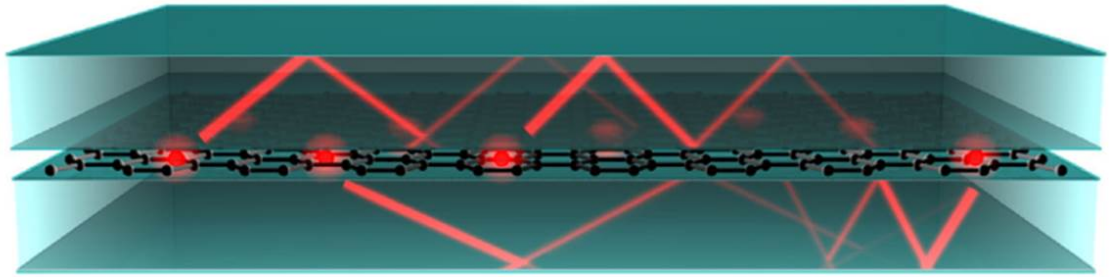

Fig. 3.15 *A schematic view of the physical system from [148]: hot carriers in graphene (red spherical balls) efficiently radiate energy into phonon-polariton modes in nearby hyperbolic crystal slabs (semi-transparent green parallelepipeds).*

Actually, there is a near-field thermal radiation transfer between hot carriers in graphene, which behave as a 2D gas of hot massless Dirac Fermion, and hyperbolic phonon polaritons in nearby dielectric slabs. The temperature of hot electrons T_e and the equilibrium temperature T_L in graphene satisfies the differential equation:

$$\partial_t T_e = -\frac{T_e - T_L}{\tau(T_e, T_L)}$$

where $\tau(T_e, T_L) \equiv C_n(T_e - T_L)/\mathcal{Q}$. Here $\mathcal{Q}$ is the rate of heat transfer between hot electrons and phonon polaritons, C_n is the electronic heat capacity at a constant density n. In the limit $\Delta T \equiv T_e - T_L \to 0$, one can expand $\mathcal{Q}$ for small values of ΔT and the ratio $(T_e - T_L)/\mathcal{Q}$ does not depend on T_e giving:

$$\tau^* \equiv \lim_{\Delta T \to 0} \tau(T_e, T_L) = \left(\frac{1}{C_n} \frac{\partial \mathcal{Q}}{\partial T_e} \Big|_{T_e = T_L} \right)^{-1}$$

τ^* acquires the physical meaning of a cooling time of hot carriers in graphene via HPP emission. The few very recent works focused on this superplanckian coupling have demonstrated a cooling relaxation time of hot carriers in graphene with HPP in hBN layer in the range of few picoseconds[148, 149, 139, 121]. Besides, these previous works have also demonstrated that recombination of electron–hole pairs in graphene through the direct coupling with intrinsic optical phonon in graphene (of comparable energy $\hbar\Omega_{OP} =$ 170–200 meV) plays a minor role in hBN/graphene heterostructures. This is because nonpolar optical phonons are coupled to electrons via the deformation potential, giving rise to a smaller relaxation rate.

We therefore attribute the additional recombination channel observed in our sample at large V^*_{DS} to this cooling process, giving rise to an additional scattering rate $\Gamma_2 = \tau_2^{-1}$, relying on the coupling of hot carriers in graphene with hyperbolic phonon polaritons (HPhPs) in the hBN layers.

Figure 3.16 shows the bias dependence of V^*_{DS}/I_{PC}, a quantity which is directly proportional to the total recombination rate $\Gamma(V^*_{DS})$ itself the weighted sum of the Auger rate Γ_1 and HPhP rate Γ_2. $\Gamma(V^*_{DS})$ increases strongly above the threshold V_0 illustrating that $\Gamma_2 > \Gamma_1$. The gradual increase of $\Gamma(V^*_{DS})$ for $V^*_{DS} > V_0$ indicates that the electric field enables an increasing number of carriers within the relaxed carrier distribution to gain energy for HPhP emission. In this picture, eV_0 is the onset of energy for HPhP emission. The photocurrent maximum in Figure 3.13 at $V^*_{DS} \sim 0.17$ V is larger than V_0 as a result of the combined effects of $\Gamma_2 > \Gamma_1$ and the broadening of energy/momentum carrier distribution. The relevance of a bias voltage criterion in governing the local carrier energy, $eV_0 \sim (\hbar\Omega_{II} - \hbar\omega)$, can be questioned in a diffusive regime. It is, however, supported by previous experiments using noise thermometry[121]. Our understanding relies on the carrier–carrier scattering rate ($\tau < 50$ fs), dominating over impurity scattering rate ($\tau <$ 0.3 ps deduced from the mobility). In graphene, carrier–carrier scattering is prominently collinear (due to momentum/energy conservation), meaning that it preserves momentum direction with respect to electric field orientation. Considering that Fermi velocity is energy independent in single layer graphene, the effect of electric field in carrier acceleration

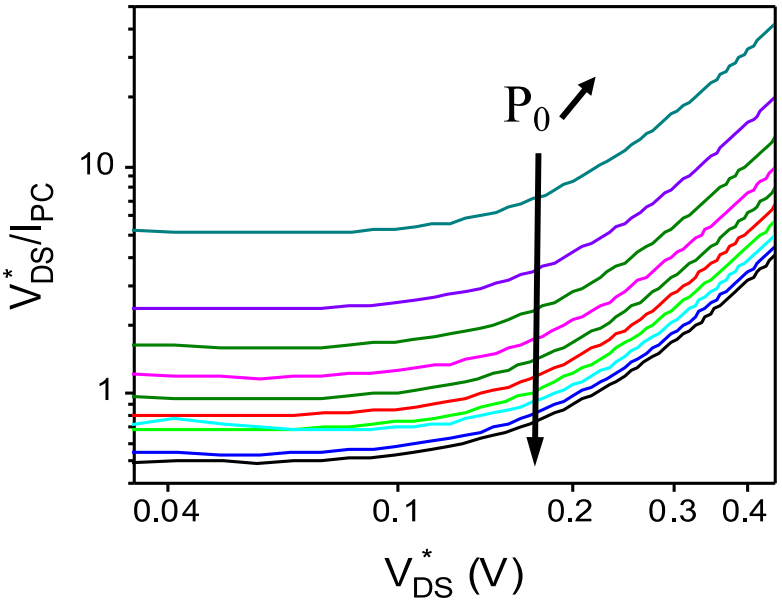

Fig. 3.16 *V^*_{DS}/I_{PC} as a function of bias in logarithmic scale for P_{inc} ranging from 0.1 to 10 mW; $V*_{DS}/I_{PC}$ is directly proportional to the total recombination rate $\Gamma(V^*_{DS})$, itself the weighted sum of the Auger rate Γ_1 and HPhP rate Γ_2.*

is independent of energy relaxation and therefore reminiscent of a ballistic case. In this picture, the electric field (bias) dependence maps the photocarrier energy distribution with respect to the HPhP energy. Figure 3.13 and Figure 3.16 show that it is broadened while keeping track of the optical pumping energy in the onset threshold $eV_0 = (\hbar\Omega - \hbar\omega)$ < 0.1 eV. The bias dependence thus provides an energy spectroscopy of the local carrier energy distribution.

3.3.3 Non-linear regime in P_{inc}

Keeping low-bias conditions, we measure the photocurrent as a function of the optical power. Figure 3.17 shows the photocurrent as a function of the optical power, for V^*_{DS} =20, 50, 90 mV. We observe nonlinear behaviors as a function of the optical power above 1 mW. We have verified independently that the absorption is still constant and does not saturate over this optical power range. The photocurrent obeys a standard saturation law:

$$I_{PC} = a\frac{P_{inc}}{1+\frac{P_{inc}}{P_{sat}}}$$

(plain lines in Figure 3.17), with a P_{sat} ≈15 mW. This saturation law is independent of the graphene bias and corresponds to an absorbed optical power of 10 μW. To explain this non linearity, let us consider that under large illumination, intraband carrier–carrier

interactions (with ultrashort relaxation times of $\sim$ 20 fs) become more efficient, leading to a broadening of the hot carrier distribution within the electron and valence bands. Some fraction of hot carriers gain energy, potentially exceeding $\hbar\Omega_{II}$, enabling some photoexcited electron–hole pairs to efficiently recombine in the hyperbolic optical phonon modes of the hBN layer. Consequently, we attribute the photocurrent saturation observed at high incident optical power to the enhancement of photoexcited carrier rates that efficiently recombine into HPhPs.

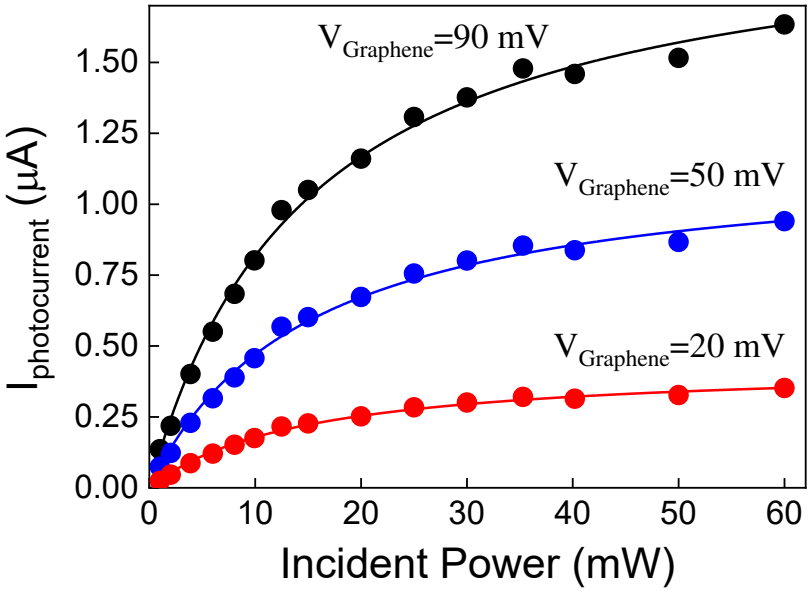

Fig. 3.17 *Photocurrent as a function of incident power beyond the linear regime. The measurements are performed at CNP for a temperature of 4 K. The plain lines in b represent standard saturation laws defined by* $I_{PC} = aP_{inc}/(1 + P_{inc}/P_{sat})$*, with a saturation power* P_{sat} *~15 mW* ($P_{abs} \sim 10\ \mu W$) *constant for all graphene bias.*

We investigate how the nonlinear behavior of the photocurrent with the incident power depends on light polarization at low bias. The saturation effect is attributed to efficient intraband carrier-carrier scatterings under intense illumination that lead to a broadening of the hot carrier distribution within the bands. Thus, some photoexcited electron-hole pairs are shifted to energetically higher states where they efficiently recombine in the hyperbolic optical phonon modes of the hBN layer. As out-of-equilibrium Zener-Klein carriers provide both an increased number of available intraband Coulomb scattering partners to the photoexcited carriers and also Pauli blocking at low energy, intraband carrier-carrier

scatterings and thus saturation effects are expected to be enhanced when the lobes of the photoexcited carriers are parallel to the dc electric field where the Zener-Klein carrier density is maximized, i.e. for light polarization perpendicular to the dc electric field. Our analysis is well supported by Figure 3.18 that highlights a more pronounced photocurrent saturation effect with the incident power for light polarization perpendicular to the dc electric field (i.e. for lobes of photoexcited carriers along the DC electric field). This is a result of out-of-equilibrium Zener–Klein carriers that provide both an increased number of available intraband Coulomb scattering partners to the photoexcited carriers as well as Pauli blocking at low energy. Thus the photoexcited carriers are redistributed towards higher energy states and their coupling to HPhP are enhanced.

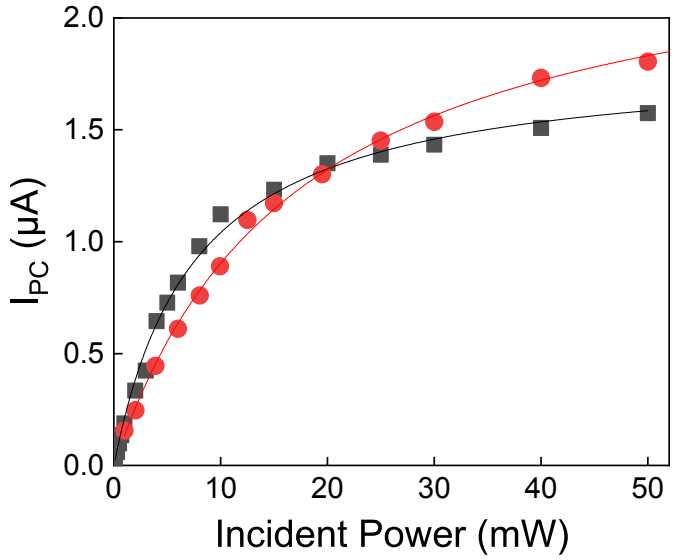

Fig. 3.18 *Photocurrent measured for light polarization perpendicular (black square symbols) and light polarization parallel (red circle symbols) to the graphene channel and the dc electric field. Using the standard saturation law given by* $I_{PC} = aP_{inc}/(1 + P_{inc}/P_{sat})$ *(plain lines) we extract saturation powers of* $P_{sat} \sim 15$ *mW and 7.5 mW for light polarization parallel and perpendicular to the graphene channel respectively.*

3.3.4 Photoexcited carrier density

We investigate the steady density of photoexcited electron–hole pairs supplied to the HPhP emission in these two distinct nonlinear regimes. Applying Equation(3.2), we extract in Figure 3.19(left) the photoexcited carrier density Δn_{photo} couple to the HPhP in the hBN layer at large V^*_{DS}, which falls in the range of 0.5×10^9 cm^{-2} for P_{inc}=1 mW. We also extract the corresponding power drained away by HPhP emission given by $P_{HPP} = \Delta n_{photo} \hbar \omega_{HPP}/\tau$ which scales with the μW level. As well, at large P_{inc}, we

extract Δn_{photo} (see Figure 3.19 (right)) from the difference between the photocarrier density expected for photoconductive regime at large incident power (dashed blue line) and the photocarrier density estimated from Equation(3.2) and measurements (blue circle symbols). The photoexcited carrier density Δn_{photo} that couple to HPhP in the hBN layer (square black symbols) is in the range of 10^9 cm^{-2} and also follows a threshold behavior.

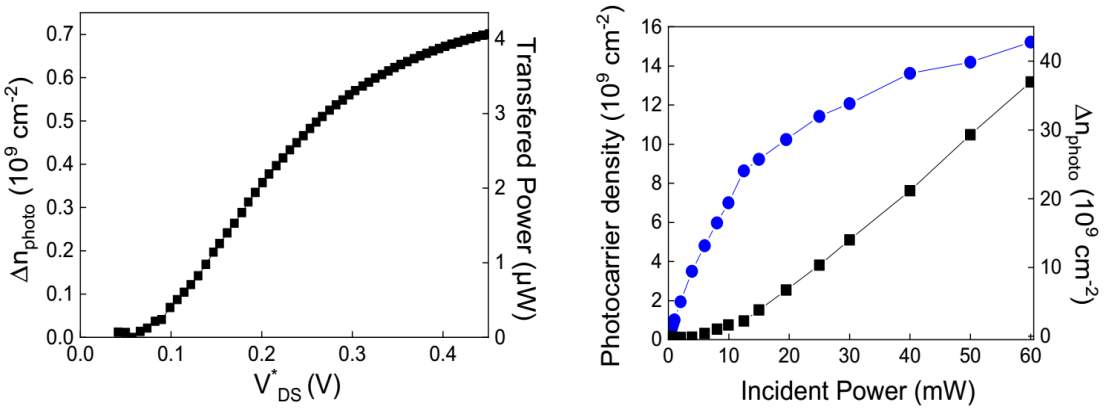

Fig. 3.19 *Left: Photoexcited carrier density Δn_{photo} couple to the HPhP in the hBN layer and the power drained away by HPhP emission as a function of bias for P_{inc} = 1 mW extracted from ΔI_{PC}. Right: Photocarrier density, n_{photo}, as a function of the incident power (blue circles and left vertical axis) and Δn_{photo} (black squares and right vertical axis) the difference between the photocarrier density expected for photoconductive regime at large incident power (dashed blue line) and n_{photo}.*

3.3.5 Full photoconductive response including all regimes

Finally, we enlarge scope to the full photoconductive response including bi-non-linear effects. Figure 3.20a,b represent the carrier lifetimes as a function of V^*_{DS} (at P_{opt} = 0.5 mW) and P_{opt} (at V^*_{DS} = 0.1 V). They show that both V^*_{DS} and P_{opt} act as distinct control knobs to switch on the pathway for hot carriers in graphene to recombine via HPhP emission in the hBN layer. Indeed, at low dc electric field and low optical power, the carrier lifetime is long, $\sim$ 35 ps, and mainly governed by Auger recombination process, whereas we note that the ignition of the competing ultrafast HPhP recombination pathway is observed at large dc electric field and incident optical power. These results highlight the interplay between Auger recombination process and electron–hyperbolic phonon recombination channel. We deduce in Figure 3.20a the characteristic time of the electron–hyperbolic phonon recombination process, corresponding to the carrier lifetime at very large bias, to picoseconds in full agreement with the picosecond hyperbolic cool-

ing times measured in previous reports for hBN-encapsulated graphene[112, 148]. This agreement confirms the validity of our method of carrier lifetime extraction. This two-recombination rate analysis is supported and quantified by theoretical fits of $\tau = \Gamma^{-1}$ in Figure 3.20a,b (red lines) with $\Gamma = \Gamma_1 + \Gamma_2(V^*_{DS} - V_0)^2$ and $\Gamma = \Gamma_1 + \Gamma_2(P_{inc} - P_0)$, respectively. We deduce $V_0 = 0.07$ V, $P_0 = 0.5$ mW, $1/\Gamma \approx 35$ ps, and a unique $-1/\Gamma_2 \approx 0.7$ ps for both fits. Remarkably, the two different determinations of the threshold, from the onset in Figure 3.14 on the one hand and by adjustment of large bias data in Figure 3.20a on the other hand, give consistent values of the threshold voltage $V_0 \sim \hbar(\Omega_{II} - \omega)/e$.

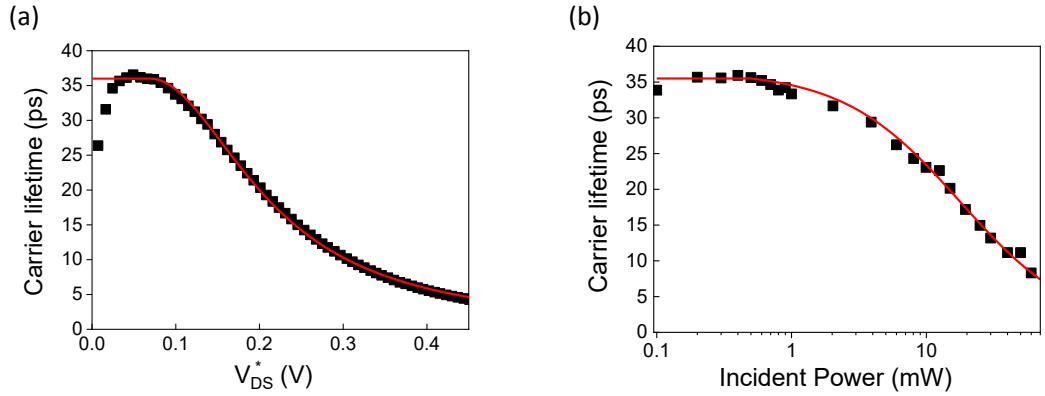

Fig. 3.20 *Electrical and optical pumping of graphene/hBN phototransistor. Carrier lifetimes as a function of V^*_{DS} a) and P_{inc} b) for $P_{inc} = 0.5$ mW and $V^*_{DS} = 0.1$ V, respectively, showing that both dc electric field and incident optical power act as distinct control knobs to switch on the non-linear response of the graphene/hBN phototransistor. Red lines in a, b are theoretical fits of $\tau = \Gamma^{-1}$ with$\Gamma = \Gamma_1 + \Gamma_2(V^*_{DS} - V_0)^2$ and $\Gamma = \Gamma_1 + \Gamma_2(P_{inc} - P_0)$, respectively.*

Figure 3.21 summarizes the interplay between optical and electrical pumping. It shows a color plot of the full scope of these two methods of pumping the hBN/graphene heterostructures. The ratio $I_{PC}/(V^*_{DS}P_o) = A\mu\tau$ with $A = Wq\alpha_0/(L\hbar\omega S_{laser})$ is represented as a function of the electrical Joule power $P_{elec} = I_{dark}V^*_{DS}$ and the absorbed optical power P_{abs}. The linear regime appears as a red plateau; the non-linear regimes of Figure 3.20a,b are represented by dashed lines. The symmetrical effects of electrical and optical powers are remarkably reflected in the color plot, including the first diagonal where both powers are comparably involved. This means that the photoresponse at charge neutrality merely measures the total number of excited carriers irrespective of their pumping pathway, presumably due to ultrafast intraband carrier–carrier scattering shuffling carrier energy. The non-linear regime at high Joule power and high absorbed optical power uniquely provides a true opto-electrical excitation of HPhPs. Combining mid-infrared illumination and large

bias dc electric field in hBN/graphene heterostructure is very promising for developing sources for HPhP optics. It promotes graphene/hBN heterostructures as a platform for studying the interplay between optical and electrical pumping of HPhP.

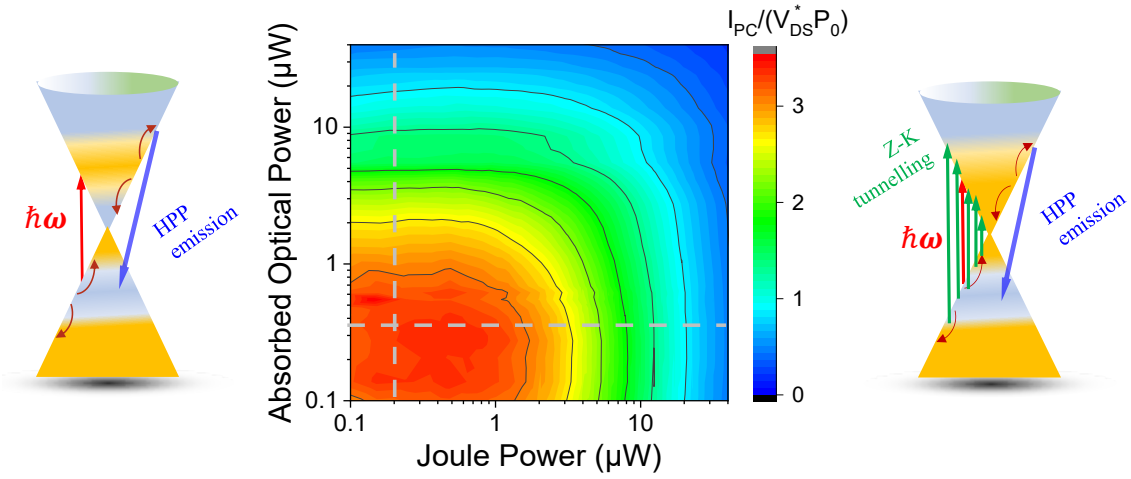

Fig. 3.21 *Sketch of the dominating relaxation and recombination processes under high optical pumping at a low bias (left) and under a weak optical pump at large bias (left). The intraband carrier–carrier interactions become more efficient at high optical pumping leading to a broadening of the hot carrier distribution providing enough energies to some photoexcited electron–hole pairs to efficiently recombine through HPhP emission (right). Under large dc electric field and efficient carrier–carrier scattering owing to the presence of a large Zener–Klein carrier density, a fraction of carriers gains energies exceeding energy of 170 meV, enabling some photoexcited electron–hole pairs to efficiently recombine through HPhP emission (left). Center: Contour plot of the ratio of the photocurrent to the product of the bias times the incident optical power, $I_{photo}/V^*_{DS}P_o$, as a function of the electrical Joule power $P_{elec} = I_{dark}V^*_{DS}$and P_{abs} highlighting the interplay between optical and electrical pumping and the opto-electrical pumping of HPhPs in the hBN layer at high Joule power and high optical power. The two dashed lines represent the non-linear regimes of Figure 3.20a,b*

3.4 Conclusion and Perspectives

In conclusion, using mid-infrared photoconductivity measurements we have investigated recombination processes of carriers photoexcited at low density and energy in graphene/hBN Zener–Klein transistors. We have shown remarkable long carrier lifetime $\sim$ 30 ps, in quasi-intrinsic graphene, ultimately limited by interband Auger processes. Long carrier lifetime in graphene/hBN heterostructures could have important implications for THz lasing and highly sensitive THz photodetection. We have also unveiled

the possibility to switch on at finite dc bias or mid-infrared optical power the very efficient electron–hyperbolic phonon recombination channel. This allows the carrier lifetime control, which falls below a few picoseconds upon ignition of HPhP relaxation. Investigating recombination processes for non-equilibrium carriers at low density and energy in alternative materials such as bilayer graphene and topological insulators could provide unique basic physic knowledge. Furthermore, we have investigated the interplay between optical and electrical pumping and demonstrated the opto-electrical pumping of HPhPs in the hBN layer at high Joule power and high optical power. These works could promote graphene/hBN heterostructures as a platform for phonon polariton optics and nanoscale thermal management.

Chapter 4

Graphene based metal-dielectric waveguide

4.1 Introduction

To improve the maturity of THz technology and expand the field of THz applications, the development of new passive devices with advanced performances are needed. For instance, to increase the point-to-point distances of wireless telecommunication near 300 GHz [8, 150], the power budget must be increased for an error-corrected transmission. Thus, using efficient compact THz amplifiers, considerably point-to-point distances $>$ 100 m will be possible. Modulators are also key components to support the capabilities of THz technology. Indeed, optical modulators are widely used for beam manipulation, high-speed imaging, and active mode-locking. For THz wireless communications, optical modulators would be used to encode information on the THz carrier frequency.

Despite these needs, the development of fast and efficient amplifiers and modulators operating at THz frequencies are in their early stages. Several material systems have been considered as the active material for realizing THz amplifiers. Among them, graphene is very promising since owing to its zero bandgap, THz photons can induce interband transitions in this 2D material, which have no equivalent in usual semiconductor materials. Interband processes at THz frequencies could provide optical gain in population-inverted graphene. This perspective is supported by the demonstration of population inversion in graphene close to the Dirac point under intense optical excitation[151, 101, 86].

For THz optical modulator, graphene is also very appealing since its intraband absorption at THz frequencies is electrically tunable through a simple gate electrode and electron mobility is high in graphene at room temperature. As a result, large modula-

tion efficiency and high working bandwidth are reachable. Moreover, graphene can be mechanically placed onto arbitrary substrates and thus is easily integrated with other components based on silicon technologies or with THz quantum cascade lasers.

However, the inherent thinness of graphene severely limits its interaction with normal incident light. For instance, interband absorption of monolayer graphene is limited to 2.3% when light penetrates the graphene at normal incidence. Thus enhancing light-matter interaction is crucial for the development of efficient graphene-based optoelectronic devices.

In recent years, several strategies have been proposed to enhance the interaction between a graphene layer and a THz optical field with the aim to develop THz modulators and amplifiers. These strategies can be divided into two main categories: the resonant and non-resonant approaches.

Resonant approaches The insertion of graphene layer into an optical cavity provides enhanced interaction of THz light with the 2D material in a resonant way. S. Lee *et al.* have integrated graphene layers into two-dimensional metallic metamaterials with gate control. They demonstrated an amplitude modulation efficiency of 47% and a modulation speed exceeding 100 kHz at room temperature. B. Sensale-Rodriguez *et al.* have developed an electro-absorption modulator by integrating graphene within a reflector structure and demonstrated modulation at 4 THz with a modulation depth of 64% and low insertion loss $\sim$ 2 dB[152]. Y.Yao *et al.* have developed a modulating device composed of optical antennas on graphene incorporated into a subwavelength-thick optical cavity, achieving 100 % of modulation depth with speed 20 GHz over a broad wavelength range (5–7 µm) [153]. Liang *et al.* have integrated a graphene modulator within a surface-emitting THz QCL operating at 3.2 THz. They demonstrated a 100% modulation depth with a modulation speed greater than 100 MHz. The bandwidth of the modulator was mainly limited to the linewidth of the cavity resonance[154]. Additionally, the insertion of a graphene layer into a THz cavity has been theoretically studied for THz amplification and lasing. V. Ryzhii *et al.* have proposed a structure based on a stack of graphene layers on SiC as an active layer placed between the highly reflecting metal mirrors. Under optical pumping of 6.4x10^4 W/cm^2, they predicted lasing at 1 THz at room temperature[155].

These approaches, limited to resonant interaction of THz photons with the graphene, result in narrow bandwidth devices. Non-resonant approaches for enhancing the THz light-graphene interaction are preferred for the development of broadband THz devices.

Non-resonant approaches Non-resonant approaches mainly rely on integrating the graphene layer within THz waveguides to increase the interaction length of THz light with the graphene layer. M. Mittendorff *et al.* [64] have developed an original approach relying on a graphene layer buries within the middle of a silicon waveguide optimized for THz frequencies. They demonstrated experimentally 90% of modulation depth with 5 GHz modulation speed from 0.2 THz to 0.7 THz for a 10 mm-long waveguide. Theoretically, Locatelli *et al.* [156] have proposed advanced structures based on a coupler with a graphene sheet inserted between two THz silicon waveguides providing a modulation depth as high as 82%. Besides, to improve optical gain at THz frequencies in graphene, V. Ryzhii *et al.* have numerically investigated the enhancement of light-matter interaction by integrating multilayer graphene into slot-line dielectric waveguides and surface plasmonic metal waveguides [106]. Several theoretical works have also proposed strategies of burying the graphene layer in between two different layers of different dielectric materials to enhance THz light-graphene interaction[157, 158, 159]. The main limitation of these approaches is that they are based in conventional dielectric, ridge or strip waveguides[160] for which the components of the propagating electric field that can interact with the graphene layer (in-plane components) are confined in the core of the waveguide with their maximum at the center of the waveguides. As a result, the graphene layer is inevitably buried within the middle of the waveguides requiring difficult technical fabrication processes. This can explain why large quantities of works are limited to numerical investigations.

During my thesis work, I have investigated original hybrid metal-dielectric waveguides coupled to a graphene layer that provide significant enhancement of the THz light-graphene interaction. An important advantage of our approach is that the graphene layer is deposited on top of the waveguides, without the need to be buried, making these devices easy to fabricate[161]. Moreover, their design has great potential to be potentially integrated to other optoelectronic devices such as THz QCL to build up THz optoelectronic circuits.

This chapter is firstly dedicated to the description of these original graphene-coupled dielectric-metal waveguides. Then, we will present the numerical investigation we performed on the properties of the modes propagating along these original waveguides, their interaction with a graphene layer deposited on top and on the potential of these devices as THz modulators and THz amplifiers. This numerical analysis provides an important insight into the properties of the electromagnetic eigenmodes propagating within these waveguides and how they interact with graphene. This step is essential for optimizing the design of the graphene-coupled dielectric-metal waveguides, with the aim to realize THz

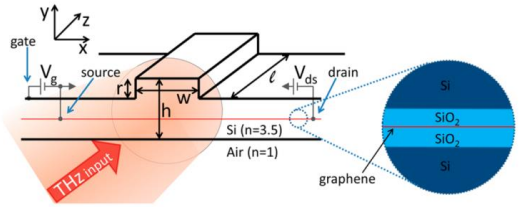

M. Mittendorf *et al.*

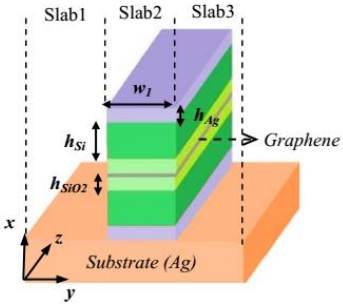

S. Hosseininejad *et al.*

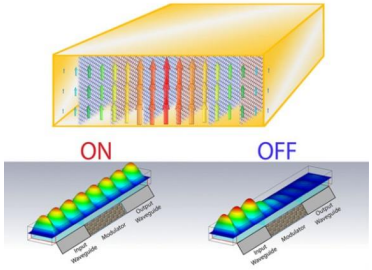

I. Khromova *et al.*

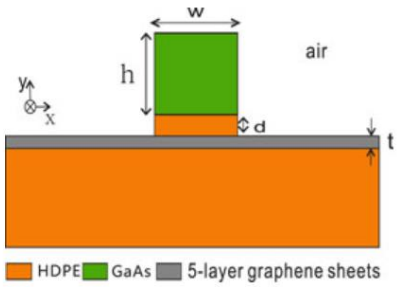

X.Zhou *et al.*

Fig. 4.1 *Few examples of previous reports on graphene coupled to dielectric waveguides. The graphene layer is buried within the dielectric core of the THz waveguides.*

modulators and THz amplifiers.

4.2 Description of the graphene-coupled dielectric-metal waveguides

Figure 4.2a shows a schematic of the hybrid dielectric-metal waveguides coupled to a graphene layer. This graphene-coupled waveguide structure is composed of monolayer graphene, a dielectric strip made up of intrinsic silicon or GaAs (or alternative dielectric material) and a metallic layer. The monolayer graphene is deposited on top and two small electrodes are deposited on the graphene layer that is connected to the external electrodes. Such electrodes allowing apply source-drain voltage, V_{DS}, and gate voltage, V_{GATE}. To perform transport characterization, the drain electrode is connected to the ground, the source electrode is connected to the voltage supply and the bottom metallic

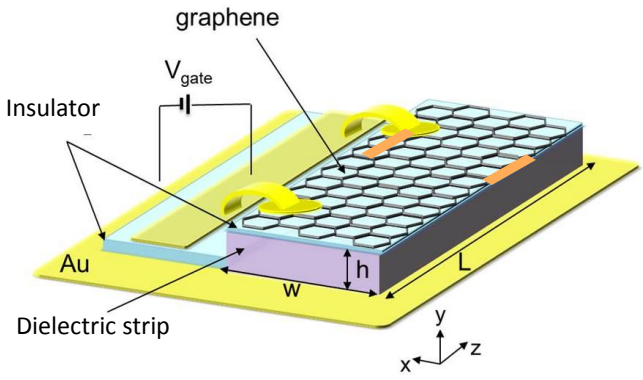

Fig. 4.2 *Sketch of the 2D material coupled to the waveguide structure.*

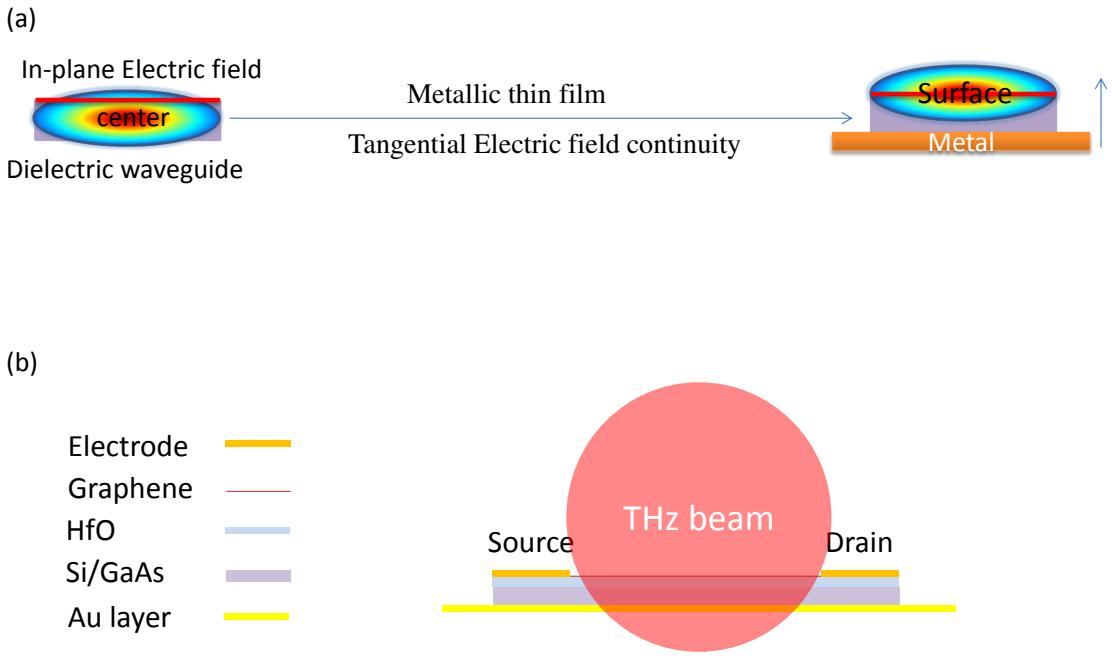

Fig. 4.3 *a) The electric field of TE mode moves from center of the dielectric strip to its top after introducing a metallic layer at the bottom. b) Front view of the waveguide and cross-section of the incident THz beam.*

layer is connected to a bottom gate voltage. In between the graphene and the dielectric layer, there is a 40 nm thick insulator layer of HfO that acts as the gate isolating layer. The bottom metallic layer is made by 500 nm-thick Au, which has a high refractive index in the THz range. This metallic layer plays a key role by pushing up the components of the electric field parallel to the graphene layer to the top of the dielectric strip. As a result, the electric field is maximized at the top of the dielectric strip where is located the graphene layer (or any other 2D materials). This feature is distinctive from conventional dielectric waveguides, as shown in Figure 4.2b. Figure 4.2c shows the facet of the waveguide and the large cross-section of a free-space THz incident beam. An important advantage of our approach is that its fabrication relies on well mastered technological processes.

4.3 Mode analysis of waveguides based on FEM method

We start our study by the numerical characterization of the fundamental modes propagating along these hybrid waveguides. First, we consider the hybrid waveguides without any graphene layer on top and then analyse their interaction with a graphene layer on top.

4.3.1 Full vector mode analysis in 2D

In our work, we use a 2D model based on the finite element method (FEM) carried by COMSOL Multiphysics (Electromagnetics module: Electromagnetic Waves, Frequency Domain and Electromagnetic Waves). The FEM is a powerful tool in the mode analysis of waveguides as it is usually formulated on a variational expression by using the Galerkin procedure, which results in so-called *'weak formulation'*. For waveguide analysis, the weak formulations include (but not limited to) the full-H, full-E[162]. To perform with high efficiency the full vector mode analysis, we assume that the waveguide is infinitely long along the z-direction. We draw the waveguide cross-sections and set an out-of-plane propagation. In other words, we assume that the geometry is mathematically extended to infinity in both directions along the z-axis and that the electromagnetic fields propagate along the z-direction (their wave vectors are out-of-plane). Additionally, we assume that all the dielectric materials are homogeneous and isotropic. We use the time-harmonic representation of COMSOL Multiphysics with out-of-plane direction and solve for the propagation constants. The spatial variation of the fields along the z-direction can be isolated in the general solutions giving the following expressions for the electric and the magnetic fields :

$$\vec{E}(\vec{r},t) = \mathrm{Re}(\widetilde{\mathbf{E}}_0(x,y)e^{i\omega t - i\widetilde{k}z})$$
$$\vec{H}(\vec{r},t) = \mathrm{Re}(\widetilde{\mathbf{H}}_0(x,y)e^{i\omega t - i\widetilde{k}z})$$

The out-of-plane wave number $\widetilde{k} = 2\pi\widetilde{n_{eff}}/\lambda$ is a complex number with $\widetilde{n_{eff}}$ is the complex effective index of the propagating modes. The propagation constant is equal to the real part of $\widetilde{k}$ and the imaginary part of $\widetilde{k}$ represents the damping along the propagation direction.

We select meshing of the cross-section of the waveguide into the form of polygons as triangles to avoid singularity issues. For the different elements involved in this hybrid waveguide structure, different meshing patterns are used to optimize computing efficiency. The domains, which contain important information such as the vicinity of the top surface of the dielectric layer and the metallic layer, have a finer mesh; the size of the triangular mesh unit has a minimum of $\lambda/500$. The *'air box'* surrounding the upper part of the waveguide is at least 10 times larger than the wavelength since we need to simulate an infinite boundary. As those domains out of the waveguide area do not contain critical information, we use a sparse meshing density with a meshing unit size of up to 2λ. Moreover, to properly resolve the electromagnetic waves, we verify that the meshing uses about 10 linear elements per wavelength. The finite element method approximates the solution within each element, using some elementary shape function that can be constant, linear, or of a higher order.

4.3.2 Boundary conditions

We set boundary conditions to simulate the electromagnetic waves that penetrate into the waveguides from the front facet and propagate along the waveguide length. The governing equations for the electromagnetic fields is presented in subsection 4.3.1. According to the boundary condition, at y=$-t_{metal}$ where the lower edge of metallic layer locates, $E_x = 0$ and $E_z = 0$ (see Figure 4.4). Although both Re($\widetilde{n}_{metal}$) and Im($\widetilde{n}_{metal}$) have high values at THz frequencies, there is a nonnegligible penetration of the electromagnetic waves in the metal due to the skin effect in the metallic layer; typically $\sim$ 50nm at 2 THz for Au. As a result, the thickness of the metallic layer is set exceedingly to avoid skin effect down to the lower edge of the metallic layer. Thus, the zero electric field is satisfied at the lower edge. Moreover, we apply the wave equations on all domains and set the lower edge as Perfect Electric Conductor(PEC):

$$\vec{n} \times \vec{E} = 0$$

The perfect electric conductor boundary condition is an ideal condition for the electric field that vanishes the tangential component of the electric field to zero. As a result, the continuity of the electric field from the bottom of the whole 2D model is satisfied. Other outer boundaries are applied with PEC conditions to approximate infinite distance.

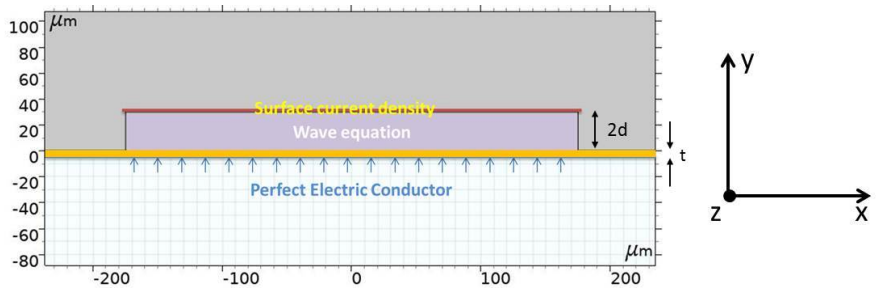

Fig. 4.4 *Sketch of the boundary conditions we applied for the 2D simulation.*

a) Defining graphene in COMSOL

An essential point for our analysis is to simulate accurately the atomically thin graphene layer. In this model, all the domains have their geometry scale from 100 nm to 1000 µm while the monolayer graphene has only a thickness of 3.35 Å that is three orders of magnitude less than the second smallest scale. These very different scales involved in the simulation could lead to less efficient processing and most probably could prevent from convergence or produce system crashes. To overcome this issue, the graphene layer can be fully described through its surface dynamic conductivity [163], with fundamental boundary conditions. Therefore, instead of constructing a domain with a height of 3.35 Å and applying boundary on this domain, we set the graphene layer as an edge boundary condition surface current density. We employ the magnetic field boundary condition, which states that the difference of the tangential magnetic fields on the opposite sides of the boundary has to be proportional to the tangential electric field at the boundary, with the surface conductivity as the factor of proportionality :

$$\vec{n} \times (\vec{H_1} - \vec{H_2}) = \vec{J_s} = \sigma \vec{E}$$

where $\vec{n}$ is the surface normal unit vector, $\vec{H_1}$ and $\vec{H_2}$ are the magnetic fields on the opposite sides of the boundary. The surface current density vector is given by:

$$\vec{J_s} = \vec{J_{sx}} + \vec{J_{sy}} + \vec{J_{sz}}$$

In graphene, the surface conductance $\vec{J_s}$ is parallel to the surface, so the y component $\vec{J_{sy}} = 0$. The complex conductivity of the graphene layer $\widetilde{\sigma}(\omega)$ contains both intraband $\widetilde{\sigma}_{intra}(\omega)$ and interband contributions $\widetilde{\sigma}_{inter}(\omega)$, which are expressed as:

$$\begin{aligned} \widetilde{\sigma}_{intra}(\omega, T) &= D\tau/\pi(1 - i\omega\tau) \\ D &= \frac{2e^2}{\hbar^2} k_B T \cdot ln[2cosh(\mu/k_B T)] \end{aligned} \tag{4.1}$$

and

$$\widetilde{\sigma}_{inter}(\omega,T)=\frac{\pi e^2}{4h}[tanh(\frac{\hbar\omega+2\mu}{4k_BT})+tanh(\frac{\hbar\omega-2\mu}{4k_BT})] \tag{4.2}$$

where D is the energy-dependent density of states in graphene, τ is the electron momentum scattering time, μ is the chemical potential, T is the temperature and $\hbar\omega$ is the photon energy. The total conductivity is $\widetilde{\sigma}(\omega)=\widetilde{\sigma}_{intra}(\omega)+\widetilde{\sigma}_{inter}(\omega)$. Figure 4.5 shows the real part of the total conductivity and the absorption of a graphene monolayer for a light of frequency 1 THz incoming at normal incidence (without any waveguide), at room temperature, as a function of the chemical potential μ of the graphene layer.

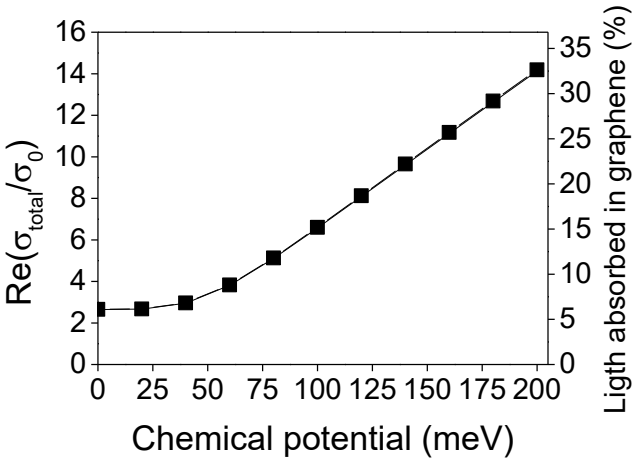

Fig. 4.5 *Calculated real part of the total conductivity and the light absorbed by a single layer graphene illuminated by a light of frequency 1 THz incoming at normal incidence as a function of the chemical potential.* $\sigma_0=\pi G_0/4$ *and* $G_0=2e^2/h$ *is the quantum of conductance[164].*

We observe interestingly that, at T = 300 K, the conductivity in the graphene layer in the THz spectral range combines intraband and interband processes. For a very high chemical potential, the absorption at 1 THz reaches 30%. However, at a very low chemical potential where intraband processes are negligible and interband processes dominate, the light absorption is limited to only a few percents. We clearly observe from these values calculated for free-space illumination at a normal incidence that enhancing the THz light-graphene interaction is crucial for the development of powerful THz amplifiers and efficient THz modulators.

b) Refractive indices of GaAs and Au in the simulation

Another two important frequency-related parameters in the simulation are the complex refractive indices of GaAs and Au. For GaAs, we refer to the parameters from [165, 166]. For the Au element, we refer to the parameters given by [167].

4.3.3 Dispersion relation of the fundamental modes

We start by investigating the fundamental modes propagating along these hybrid metal-dielectric waveguides, without any 2D material on the top of the semiconductor strip. We consider a semiconductor strip made of high-resistivity silicon with a width w = 300µm and a height h = 30 µm. The thickness of the gold layer is set to 900 nm. From computation, we observe a multitude of modes with two first fundamental modes. A fundamental mode with a weak electric field component along the propagation direction compared to the transverse electric field components, $|E_z| < |E_x|$, which is considered as a quasi-TE mode. Another fundamental mode with a weak magnetic field component along the propagation direction compared to the transverse magnetic field component, $|H_z| < |H_x|$, which is considered as a the quasi-TM. Figure 4.6a) shows the spatial distribution of the two dominant electric field components E_x and E_z for the quasi-TE mode. Note that both components can interact with a 2D material deposited on top of the strip. Actually, the

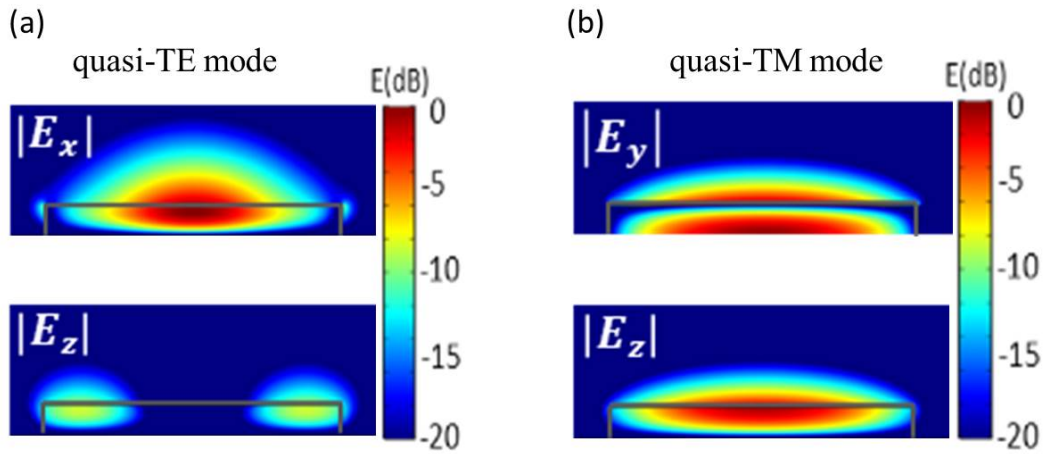

Fig. 4.6 *Calculated electric field components in the x- and z-directions of the fundamental quasi-TE mode (a) and in y and z directions of the fundamental quasi-TM mode (b) for a hybrid metal-silicon waveguide with a strip height of 30* µm *and a strip width of 300* µm *at a frequency of 1 THz.*

strength of the electric field E_x is the highest and the longitudinal electric field E_z reaches maximum $0.374E_x$. The component E_y remains 15 dB weaker. Owing to the metal layer that acts as a reflector, the strength of E_x and E_z are maximized at the antinode of the

optical field, localized in our geometry at the air/dielectric interface.

For the quasi-TM mode, the two dominant electric field components shown on Figure 4.6b) are E_y and E_z. Thus, only the longitudinal component E_z can interact with a 2D material deposited on the top of the strip. The electric field strength is nearly equally distributed between E_y and E_z since the maximum of E_z reaches 90% of the maximum of E_y. The strength of the in-plane electric field component E_z is highest at the dielectric/air interface that is promising for interacting with 2D material on top. To go further, we examine the properties of these two eigenmodes as a function of the dimensions of the waveguide strip.

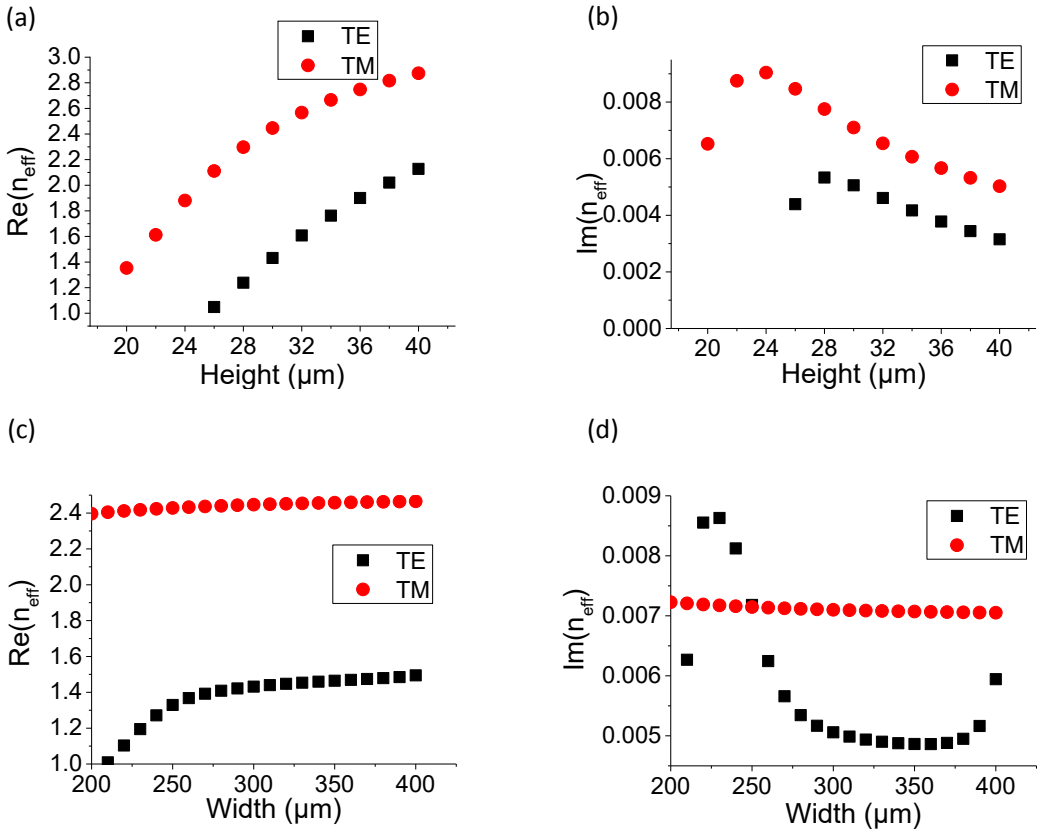

Fig. 4.7 *(a) Real and (b) imaginary parts of the effective index $\widetilde{n}_{eff}$ of quasi-TE and quasi-TM modes as a function of the stripe height h (for w = 300 μm) at 1 THz. (c) Real and (d) imaginary parts of the effective index $\widetilde{n}_{eff}$ of quasi-TE and quasi TM modes as a function of the strip width w (for h = 30 μm) at 1 THz.*

Figure 4.7 a-d report the evolution of the real and imaginary part of the effective mode index $\widetilde{n}_{eff}$ of the two fundamental modes as the function of the height and the width of

the semiconductor ridge. We observe a cut-off for the quasi-TE mode in the evolution of $\widetilde{n}_{eff}$ as the function of the strip dimensions. Indeed, for small dimensions of the strip, such as $h < \frac{\lambda}{4\,\mathrm{Re}(\widetilde{n}_{eff})}$ or $w < \frac{\lambda}{2\,\mathrm{Re}(\widetilde{n}_{eff})}$, the quasi-TE mode is no longer a guided mode. In return, for large dimensions of the strip, the quasi-TE mode is well guided and $\mathrm{Re}(\widetilde{n}_{eff})$ saturates. A cut-off of the quasi-TM mode is also observed but only as the height of the stripe is reduced. For $h < \frac{\lambda}{4\,\mathrm{Re}(\widetilde{n}_{eff})}$, the mode is no longer a guided mode. The free-carrier absorption of the electromagnetic components that penetrate into the metal layer is mainly responsible for $\mathrm{Im}(\widetilde{n}_{eff})$ for both quasi-TE and quasi-TM modes. This effect results in propagation losses described by a linear absorption coefficient given by:

$$\alpha_{WG} = -4\pi \frac{Im(\widetilde{n}_{eff})}{\lambda} \tag{4.3}$$

An important result is that the propagation losses of the hybrid waveguides are relatively small, < 1.1 dB/mm and < 1.9 dB/mm for quasi-TE and quasi-TM modes respectively over a large range of strip dimensions.

The dispersion relation of the quasi-TE and quasi-TM modes as the function of the wavelength are shown in Figure 4.8 from 200 µm (f = 1.5 THz) to 400 µm (f = 0.75 THz). We clearly see that these hybrid metal-dielectric waveguides are relatively broadband, making them interesting for guiding THz pulses.

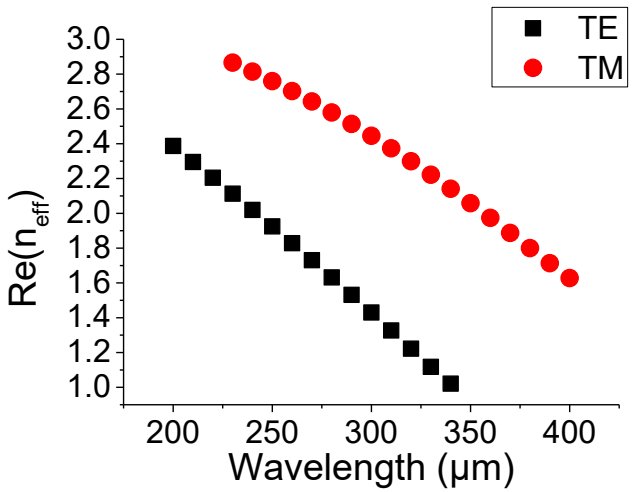

Fig. 4.8 *Dispersion relation of the quasi-TE and quasi-TM modes from 200* µm *(f = 1.5 THz) to 400* µm *(f = 0.75 THz) for a metal-silicon waveguide with a strip height of 30* µm *and a width of 300* µm.

This analysis shows that the quasi-TE mode is reminiscent of the quasi-TE mode of

a rectangular dielectric waveguide surrounded by air [168], except that it is perturbed by the metallic layer that pushes up to the dielectric/air interface the electric field components tangent to the metallic layer. On the other hand, the quasi-TM mode has all the characteristics of a Goubau mode; it is bound to a finite conductivity metal stripe coated with a thin dielectric layer, the longitudinal field component is maximal at the dielectric/air interface and the mode shows a cut-off for height $h < \frac{\lambda}{4\,\mathrm{Re}(\widetilde{n}_{eff})}$ [169].

An important outcome of this work is that owing to the metallic layer that pushes up the tangential electric components, the strength of the electric field at the top of the waveguide is reinforced at a location where a 2D material can be easily deposited. This result shows the potential of our original hybrid waveguide to enhance THz light-graphene interaction through their efficient coupling over a long distance (the length of the waveguide). Moreover, this waveguide enables the propagation of tangential electric field components for both fundamental modes.

4.3.4 Graphene coupled to the hybrid dielectric-metal waveguide

We now investigate how evolve the properties of the two fundamental modes propagating along the hybrid dielectric-metal waveguides when a graphene layer is deposited on the top of the ridge. We investigate two main regimes: The graphene conductivity is dominated by intraband process, i.e. $|\mu| > \hbar\omega/2$ and the graphene conductivity is dominated by interband process, i.e. $|\mu| < \hbar\omega/2$. Whereas the first regime is optimal for the development of THz modulators, the later one is adapted to the realization of THz amplifiers. To illustrate these two regimes, I report on Figure 4.9a) an example of the graphene conductivity with preponderant intraband process in the THz range obtained for $\mu = 200$ meV (T = 10 K, $\tau = 10$ fs) and on Figure 4.9b)an example of the graphene conductivity with preponderant interband processes in the THz range obtained for $\mu = 0\ meV$ (T = 10 K, $\tau = 10$ fs).

a) Intraband absorption in graphene coupled in waveguide

For $\hbar\omega/2 < |\mu|$, the optical conductivity in graphene at THz frequencies is governed by intraband processes described by Equation(4.1). In our calculation, we assume that $\tau = 10\ fs$ in agreement with litterature[170]. We first focus on the similar waveguide geometry than in subsection 4.3.3: w = 300 µm, h = 30 µm. The calculated effective mode indices of the bare waveguides at 1 THz are $\widetilde{n}_{eff} = 1.432 + 0.005i$ and $\widetilde{n}_{eff} = 2.4452 + 0.007i$ for the quasi-TE and quasi-TM mode respectively. By adding the graphene layer on the top of the ridge, both the real part and imaginary part of $\widetilde{n}_{eff}$ are expected to be modified. We study the evolution of $\widetilde{n}_{eff}$ for both fundamental

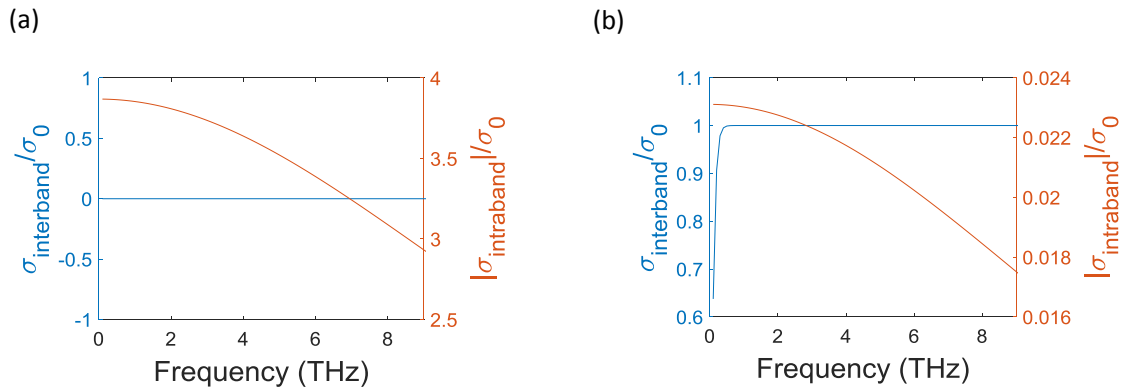

Fig. 4.9 *Interplay between interband and intraband processes in the conductivity of a graphene monolayer at $T = 10$ K and scattering time $\tau = 10$ fs. a) The optical conductivity dominated by intraband processes, $\mu = 200$ meV. b) The optical conductivity dominated by interband processes, $\mu = 0$ meV.*

eigenmodes as a function of μ. We tune μ from 0 to 200 meV as such chemical potential range is easily accessible practically in graphene monolayer with a simple gate electrode.

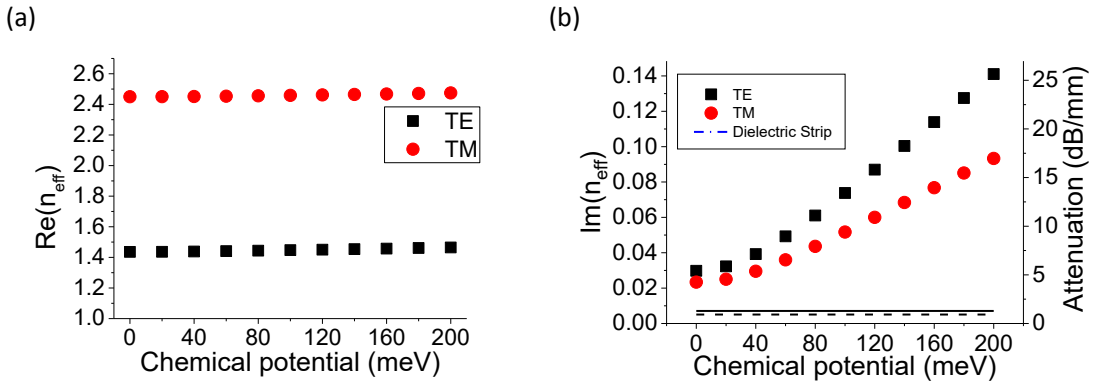

Fig. 4.10 *Real (a) and imaginary (b) parts of the effective mode index as a function of the chemical potential of the single graphene layer coupled to a metal-Si waveguide ($h = 30$ µm, $w = 300$ µm) at 1 THz for quasi-TE and quasi-TM modes. The corresponding attenuation in dB/mm is shown in b).*

Figure 4.10 shows that $\mathrm{Re}(\widetilde{n}_{eff})$ remains relatively constant as μ increases whereas $\mathrm{Im}(\widetilde{n}_{eff})$ increases significantly for both fundamental modes. We interpret these results by the fact that $\mathrm{Re}(n_{eff})$ is dominated by the spatial distribution of the modes between the dielectric layer and the cladding layer (air); thus the monolayer graphene has a negligible impact on it. In return, as the waveguide geometry is optimized to enhance the

THz light-graphene interaction, the graphene efficiently absorbs the THz light leading consequently to an increase of Im($\widetilde{n}_{eff}$) for both fundamental modes. As expected, we observe on Figure 4.10 that the quasi-TE mode has more interaction with graphene than the quasi-TM mode.

Figure 4.10b shows the attenuation of the quasi-TE and quasi-TM modes propagating along the hybrid waveguide coupled to a graphene layer. The attenuation is calculated using the Equation (4.3). It reaches up to 24.7 dB/mm and 15.6 dB/mm at μ=200 meV for quasi-TE and quasi-TM mode respectively. Since this attenuation is proportional to Re($\sigma_{graphene}$)Γ with Γ the overlap factor between the single graphene layer and the mode field [171] , these results demonstrate the enhancement of the light-matter interaction provided by the waveguide geometry. Note that as the quasi-TM mode possesses a longitudinal component (in contrast to usual dielectric waveguides) the graphene layer also absorbs the quasi-TM mode, making these waveguides very attractive for modulating the quasi-TM polarized light.

We further investigate the possibility for these devices, which rely on graphene coupled to hybrid waveguides to act as efficient modulators of THz light. To estimate the modulation efficiency of these devices, we calculate the attenuation of a THz beam in dB/mm and the modulation depth. The modulation depth which corresponds to the magnitude variation of the THz intensity, is expressed as :

$$m = \frac{T_{LowDoping} - T_{HighDoping}}{T_{LowDoping}}$$

where T is the transmission coefficient. In this calculation, the low doping and the high doping corresponds to μ = 0 meV (undoped) and μ = 200 meV respectively, so the modulation depth is given by:

$$m = \frac{T_{\mu=0\ meV} - T_{\mu=200\ meV}}{T_{\mu=0\ meV}}$$

We focus on 3 distinct frequencies, f = 1 THz, f = 2.5 THz and f = 4 THz. The frequencies f = 2.5 THz and f = 4 THz are typical frequencies delivered by usual QCL and for these frequencies, we choose GaAs material as the semiconductor stripe to ensure compatibility with QCL technology. We select the optimum dimensions at each considered frequency that are for f = 1 THz: h = 30 µm and w = 300 µm, for f = 2.5 THz: h = 11 µm and w = 120 µm and for f = 4 THz: h = 7.5 µm and w = 94 µm. Figure 4.11a reports Im($\widetilde{n}_{eff}$) and the attenuation in dB/mm of the quasi-TE and quasi-TM modes as a function of the chemical potential in the graphene. We observe that attenuations of 49 dB/mm and 34.7

dB/mm are obtained at f = 2.5 THz for quasi-TE and quasi-TM modes respectively. For comparison, the plain and dashed black lines represent the intrinsic attenuation of the waveguide structure (without graphene on top) due to the losses in the dielectric strip and the bottom metal.

The calculated modulation depth achievable with a single layer of graphene coupled to these hybrid waveguides is reported in Figure 4.11b. We observe a large modulation depth of more than 90% for both quasi-TE and -TM modes for a 1 mm-long waveguide. For longer waveguide L > 1.5 mm, full modulation for both quasi-TE and -TM modes is reachable at f = 2.5 THz and f = 4 THz with optimized dimensions. At f = 1 THz, a full modulation is obtained after 1.5 mm of propagation for both quasi-TE and -TM modes.

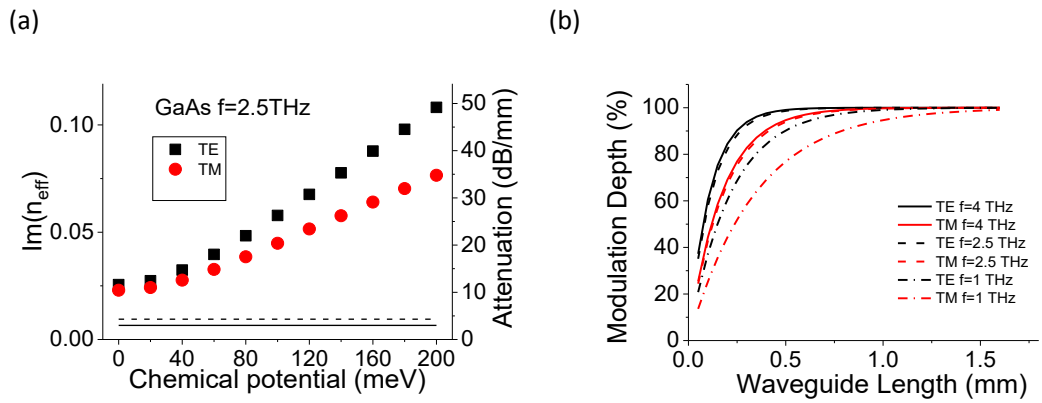

Fig. 4.11 *a) $\mathrm{Im}(\tilde{n}_{eff})$ and attenuation of the modes as a function of the chemical potential of a single graphene layer coupled to a metal-GaAs waveguide at 2.5 THz. b) Calculated modulation depth for a metal-Si waveguide at f = 1 THz (h = 30 µm and w = 300 µm), a metal-GaAs waveguide at f = 2.5 THz (h = 11 µm and w = 120 µm) and a metal-GaAs waveguide at f =4 THz (h = 7.5 µm and w = 94 µm) as a function of the waveguide length L.*

An important point is that the metal-dielectric waveguides we propose have the advantage to be fully compatible with well-mastered wafer bonding processes and it does not require unconventional fabrication steps to bury the 2D layer within the guiding structure. Besides, the possibility to modulate the quasi-TM opens the way to the integration of these devices with a QCL to build up an on-chip optoelectronic system, as illustrated in Figure 4.12.

Besides, as a perspective, this study that focuses on graphene layer could be extended to other 2D materials such as doped black phosphorus and doped transition metal disulfide (TMD) materials (i.e. MoS_2 and WSe_2) that also possess intraband conductivity in the THz range[172, 173, 174, 175, 56].

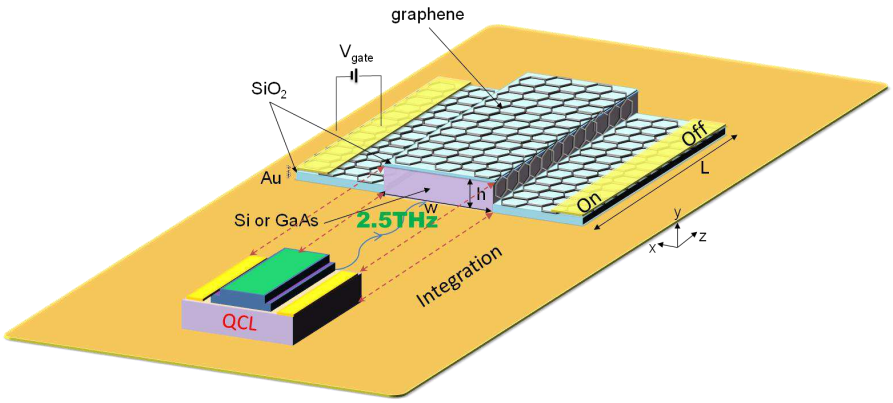

Fig. 4.12 *Schematic of the integration of a metal-GaAs waveguide with optoelectronic devices such as THz-QCL to realize on-chip optoelectronic circuit.*

b) Interband absorption in graphene coupled to waveguide

For $|\mu| < \hbar\omega/2$ and at low temperature, the optical conductivity in graphene at THz frequencies is mainly governed by interband processes. Such interband conductivity, described in Equation(4.2), has been recently demonstrated at THz frequencies in multilayer epitaxial graphene by my research group[85]. By achieving population inversion in graphene, an optical gain can thus be accessible at THz frequencies, which opens a very attractive perspective towards the realization of THz amplifiers. To improve the potential optical gain, which is limited to the universal value 2.3% when light passes through the monolayer graphene at normal incidence, enhancing the interband absorption is crucial. In this study, we assume low temperature, T $\sim$ 10 K, so that Pauli blocking effect induced by thermally excited carriers is limited. Thus, we consider the interband conductivity to be equal to $\sigma_0 = e^2/4\hbar = 6.08 \times 10^{-5}\ S$. In this condition, we calculate the interband absorption of the graphene layer coupled to the hybrid metal-dielectric waveguides for incident light at f = 2.5 THz and f = 4 THz as the function of the length of the waveguide for both quasi-TE and quasi-TM modes. At f = 2.5 THz, we consider high-resistivity silicon as the ridge material since it is compatible with silicon technology and at f = 4 THz, we consider intrinsic GaAs as the ridge material since it is compatible with QCL technology. As shown in Figure 4.13a, the graphene coupled to the hybrid waveguide

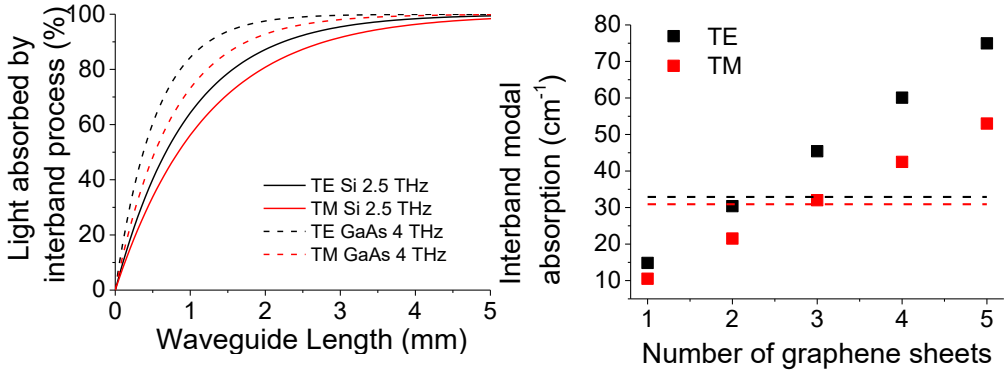

Fig. 4.13 *Right: Interband light absorption in a single graphene sheet coupled to hybrid metal-dielectric waveguide as a function of L. Left: Calculated interband modal absorption at 4 THz as a function of the number of independent graphene sheets of an Au-GaAs hybrid waveguide ($h = 7.5$ µm, $w = 94$ µm). The dashed black and red lines represent the total losses for quasi-TE and quasi-TM modes respectively for a waveguide length of 2 mm.*

can absorb 90 % of the THz light when the device length reaches 3 mm under all configurations. This result clearly demonstrates the enhancement of light-matter interaction provided by the waveguide geometry.

For a single graphene layer, the interband modal absorption reaches 18.5 cm $^{-1}$ and 16.5 cm^{-1} for the quasi-TE and quasi-TM mode respectively at f = 2.5 THz. These values show the high potential of graphene coupled to metal-Si waveguides for THz amplification. Besides, such devices show also attractive properties for THz photodetectors based on photoconductive effect. The THz amplification in this graphene-coupled hybrid waveguide is expected to be more realistic at f = 4 THz since it has been predicted that this frequency is the minimum frequency at which optical gain can be achieved in population-inverted graphene at low temperature, due to the efficient carrier-carrier scattering assisting absorption[171]. Moreover, previous theoretical works[171] have demonstrated that, due to intraband absorption that effectively competes with interband amplification, the maximum achievable optical gain in population-inverted graphene is limited to typically $0.75\alpha_{interband}$. To improve the potential achievable optical gain at THz frequencies, a stack of graphene layers can be deposited on the top of the strip. Figure 4.13 (right) shows the total interband absorption at f = 4 THz as the function of the number of independent graphene layers deposited on the top of the hybrid metal-GaAs waveguide. For achieving THz lasing, this value has to dominate the total losses. The dashed lines in Figure 4.13 (left) represent the total losses $\alpha_{total} = \alpha_{WG} + \alpha_m$ for both modes for a 2 mm-long waveguide. The absorption of waveguide α_{WG} equal to 15.3 cm^{-1} and 21.9

cm^{-1} for quasi-TE and quasi-TM mode respectively. The mirror loss α_m due to the finite mirror reflectivity of the facts is defined by $\alpha_m = -ln(R)/L$ where L is the waveguide length and $R = |\frac{\widetilde{n}_{eff}-1}{\widetilde{n}_{eff}+1}|^2$. The mirror loss α_m equal to 17.6 cm^{-1} and 9 cm^{-1} for quasi-TE and quasi-TM mode respectively. We observe that the insertion of 3-4 layers of graphene within the waveguide structure can provide enough optical gain for THz lasing. Note that at room temperature, the interband conductivity is lowered due to thermal carrier distribution as shown in Figure 4.14 and the number of graphene sheets required for achieving THz lasing is higher.

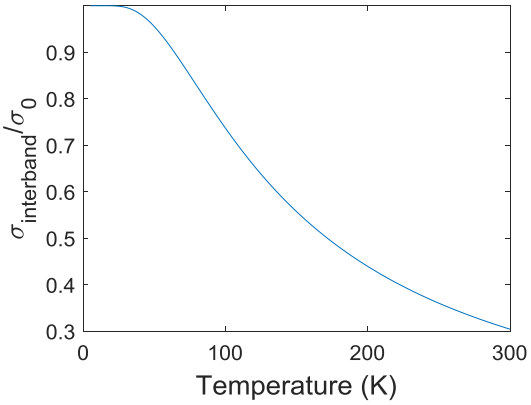

Fig. 4.14 *The interband conductivity in a single graphene as the function of temperature for $\mu = 0$ meV at $f = 4$ THz.*

4.4 Conclusion

In conclusion, this chapter reports an original hybrid metal-dielectric waveguide that provides high interaction between 2D materials deposited on top and THz photons. We investigate the fundamental quasi-TE and quasi-TM modes propagating along these hybrid metal-dielectric waveguides and show that owing to the high reflectivity and low loss of metals at THz frequencies, the strength of in-plane electric field components of the propagating modes is maximized at the top of the dielectric strip on which the 2D material is deposited. Our simulation predicts 100% modulation of the THz light by tuning the Fermi level of a graphene sheet coupled to 1mm-long hybrid metal-dielectric waveguides, which is very attractive for THz modulation applications. We also show the potential of graphene multilayers under interband regime coupled to these hybrid metal dielectric waveguides for achieving lasing at THz frequencies. Our approach relies for fabrication on well-mastered wafer bonding techniques, does not require incorporating the 2D materials into the core of a dielectric waveguide, and is compatible with CMOS technology or THz quantum cascade lasers.

Chapter 5

THz characterization of the graphene coupled hybrid waveguides

Based on the numerical study presented in section 4.3, we establish a correspondence between the parameters of the hybrid waveguides and the spatial distribution of the electromagnetic fundamental modes. We show that the E_x component of the quasi-TE can be maximized at the top of the waveguide ridge so as the E_z component of the quasi-TM mode. Consequently, the interaction of the electric components of these two eigenmodes with a graphene layer deposited on top is enhanced, opening promising perspectives for the realization of THz wave modulators and THz amplifiers.

In this chapter, we will experimentally investigate the properties of metal-GaAs waveguides with and without a graphene monolayer on top. We will first present the preliminary characterization we performed on these hybrid waveguides using Raman spectroscopy and electrical measurements. Then, we will characterize the THz waveforms propagating along these hybrid waveguides using a THz time-domain spectroscopy experiment. We will also focus on the impact of modulating the chemical potential of the graphene layer on the transmitted THz pulses. At last, we will analyze the experimental observations by calculating the contribution of the propagating THz electric fields.

5.1 Fabrication and process characterization

To go toward the experimental investigation of such devices based on graphene coupled to hybrid waveguides, we collaborate with the group of Miriam Vitiello from NEST, Istituto Nanoscienze – CNR and Scuola Normale Superiore (Italy) that has state of the art expertise on graphene-based devices for THz technology. Alessandra Digaspare and Miriam Vitiello have fabricated a series of several bare hybrid waveguides (without graphene on

top) and hybrid waveguides with graphene on top. They used graphene CVD provided by Graphenea for the fabrication. Details of the fabrication are provided in Appendix B. After receiving them, we first characterize the fabrication process using Raman spectroscopy and DC electrical measurements. The main aim is to probe the continuity of the graphene layer deposited on the top of the waveguides and to test the electrical contacts devoted to the tuning of the graphene chemical potential.

5.1.1 Characterization of the graphene coverage

A critical issue of the fabrication process is to cover without any discontinuity at the top of the waveguide with the graphene layer. Thus, it is essential to investigate the quality of the graphene coverage after the fabrication process. The length of the waveguides is in the millimeter scale and any discontinuity along this long-distance prevents from the possibility to supply homogeneous gate voltage to the graphene layer; it can lead to several areas of the graphene layer that are not gated. Another critical issue is that no conducting material, such as graphene or gold, is extending from the top of the strip to the outside bottom metallic layer since it may give rise to an undesirable short cut. For this characterization, we use mapping Raman spectroscopy carried by RENISHAW inVia™ confocal Raman microscope. We follow two strategies, shown in section B.1, to distinctively evaluate the graphene coverage and the leakage risk. Indeed, probing leakage risk requires more resolution and more integration time to obtain information on the sides of the waveguides (from dielectric strip surface to the metallic surface). By applying these two configurations, we are able to efficiently perform map scans on the hybrid waveguides with a high signal-to-noise ratio (SNR) and avoid burning the single-layer graphene.

Figure 5.1 shows the Raman spectrum on one pixel (2 µm × 2 µm). We identify the single-layer graphene by G-peak and 2D-peak at 1585 cm^{-1} and 2700 cm^{-1} respectively with 1% of laser power and 1s of integral time. In Figure 5.2a, the rectangular map shows the coverage of graphene. The intensity is represented by the rainbow Lookup Table. We can note that the central area has a higher intensity than the head and the tail area, due to the misalignment of the beam focus along the waveguide length. Indeed, we set the optimal focus at the center of the waveguide, whereas there is a non-negligible small dip angle which misaligns the focus for $\sim$ 10 µm. The Raman spectra in Figure 5.2b show the misalignment-induced out of focus thus decrease the intensity. The black curve is at the optimal focus, which has the highest intensity, the red and blue curves have a misalignment of $\pm$5 µm respectively; this well explains the intensity decrease observed at the two extremities of the waveguides that are out of focus.

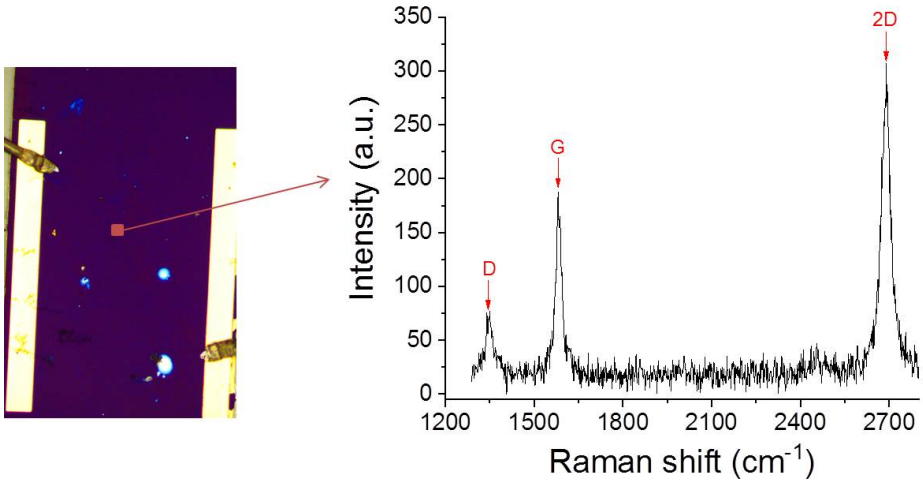

Fig. 5.1 *Raman spectrum on one pixel of the whole waveguide top surface*

Figure 5.2c gives an example of a processed waveguide, which has an unwanted graphene area on the left edge of the ridge. Combining with optical microscopy and measurements of the leaky current, we are able to screen out those waveguides with low coverage rates or leaking issues.

5.1.2 Electrical characterization

Subsequently, we perform electrical characterization of the processed waveguides. Here, we present a typical investigation of the sample WG-400-1-2500. The electrical characterization is performed twice, before bonding and after bonding respectively. We perform low-bias resistance measurements at room temperature. Figure 5.4a and c, report the resistance R_{ds} as a function of gate voltage obtained for $V_{ds} = 10\ meV$. Considering the contribution of both electron and holes to the conductance of the graphene sheet, the total resistance of a device can be calculated as: $R = \frac{L}{W}\frac{1}{\sigma} + 2R_c = \frac{L}{W}\frac{1}{q(\mu_n n + \mu_p p)} + 2R_c$, with R_c the contact resistance of each electrodes, L = 250µm the effective distance between two electrodes on the graphene, W = 700µm the width of the electrode and n, the local carrier density. The local electron density is expressed as $n = \sqrt{(C_g|V_{GATE} - V_{DP}|/q)^2 + n_0^2}$, with $C_g = \epsilon_0\epsilon_{HfO}/e_{HfO}$ and $\epsilon_{HfO} = 25$ is static dielectric coefficient of Hafnium dioxide (HfO)[176], $e_{HfO} = 40$ nm is the thickness of HfO and n_0 is the residual charge density induced by charge puddles. We fit the resistance as a function of gate voltage (red curve) and extract a mobility $\mu = 2215 \pm 93\ cm^2/(V \cdot s)$ ($\mu_n = \mu_p$) and a residual carrier density of $n_0 = 1.09 \times 10^{12} \pm 3 \times 10^{10}\ cm^{-2}$ before the bonding process. The mobility is reduced to $\mu = 749.8 \pm 5\ cm^2/(V \cdot s)$ and the residual carrier density is increased to $n_0 = 4.28 \times 10^{12} \pm 2 \times 10^{10}\ cm^{-2}$ after the bonding process. From the carrier

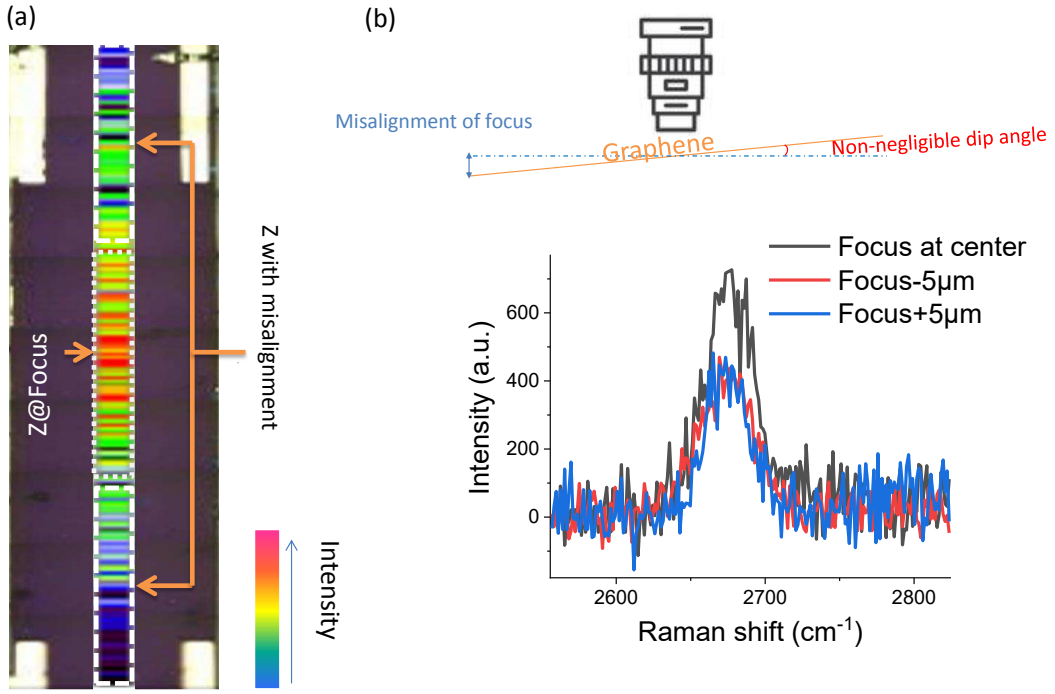

Fig. 5.2 *a) The map obtained by Raman spectroscopy along the waveguide at the center. b) The Raman spectra at the same position (middle of the waveguide) with different focuses. Schematic of the focus misalignment along the y-axis during the scan since two extremities of the waveguide do not have equal altitude due to a small dip angle, a 5µm of height difference induced by this angle can result to 50% of the difference in received reflecting intensity.*

density, we calculate the chemical potential of the graphene layer given by $E_F = \hbar v_F \sqrt{\pi n}$.

Note that the mobility before bonding is two times higher than that of after bonding and the residual conductance before bonding is 120 meV lower than that of after bonding. Additionally, by comparing Figure 5.4a and Figure 5.4c, we observe that the doping effect on electron and hole sides has better symmetry before bonding than after bonding. This is maybe due to impurities induced by the metallic electrodes and by the free contact with ambient atmosphere since the graphene layer is either not protected in the vacuum or passivated.

After characterizing the process of all waveguides we received, we have selected for further THz characterization, 4 hybrid waveguides listed below for which the fabrication

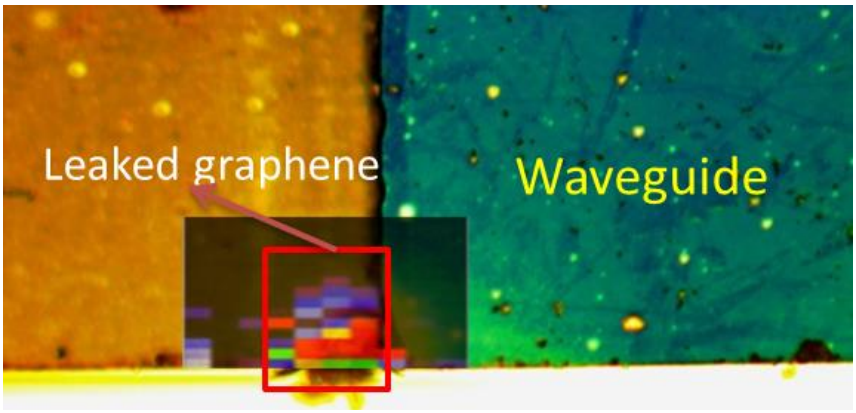

Fig. 5.3 *Illustration of a fabrication issue: an undesired flake of graphene on the edge of the waveguide that introduces leakage current*

Reference Name	**Length(mm)**	**Width(mm)**
WG-1A	2	0.4
WG-2A	3	0.6
WG-400-1-2500	2.5	0.4
WG-600-2-2500	3	0.6

Table 5.1: Hybrid waveguides, bare and with graphene on top, selected for further THz characterization.

process has been successful. For all of these samples, two distinct hybrid waveguides are processed on the same chip with similar dimensions but only one of them has a graphene monolayer deposited on top. Thus, one waveguide is a "bare waveguide" and the other is a "graphene waveguide", as illustrated in Figure 5.5. In between these two waveguides, there is a gap of 1.1 mm.

5.2 THz characterization of the devices

After the characterization of the fabrication process performed by the group of Miriam Vitiello, we use a THz time-domain spectroscopy experiment to characterize the properties of these original hybrid waveguides coupled to a graphene layer.

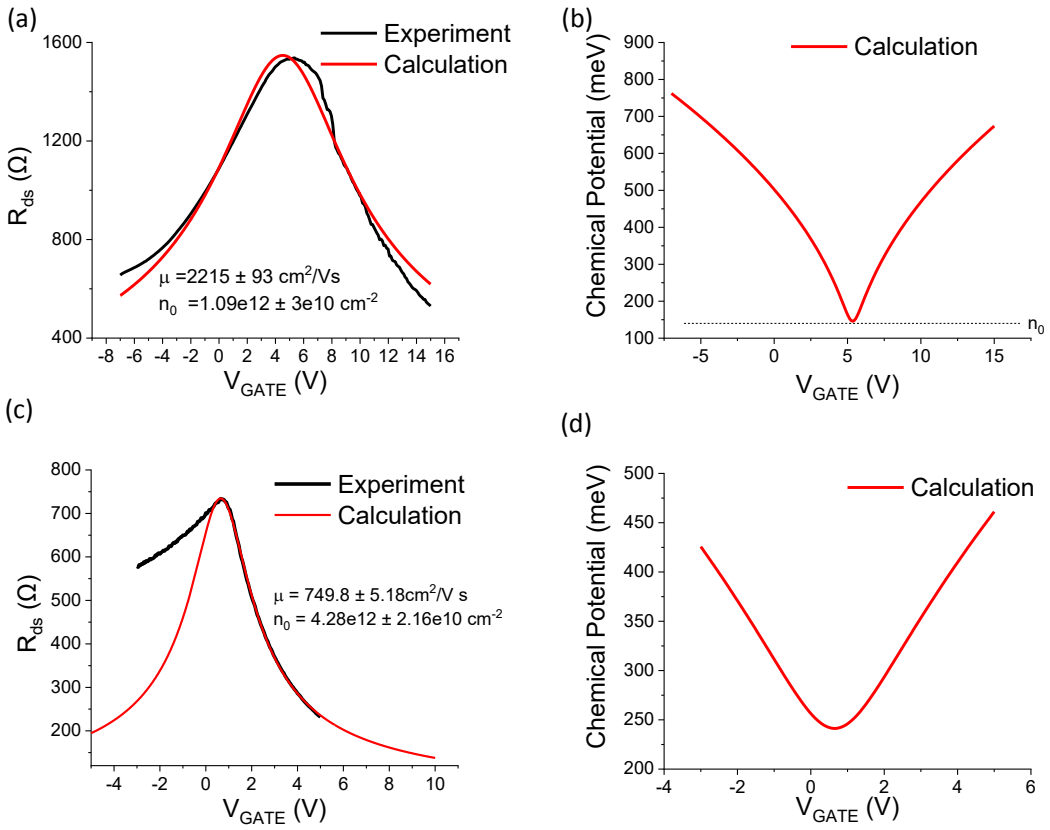

Fig. 5.4 *a) and b) are the characterization of waveguide WG-400-1-2500 before bonding, a) shows the R_{ds} as the function of V_{GATE}, the black and red curve are the experimental result and the corresponding fitting curve respectively; b) shows the chemical potential calculated on basis of fitting parameters in a). c) and d) are the characterization of waveguide WG-400-1-2500 after bonding, c) shows the R_{ds} as the function of V_{GATE}, the black and red curve are the experimental result and the corresponding fitting curve respectively; d) shows the chemical potential caculated on basis of fitting parameters in c)*

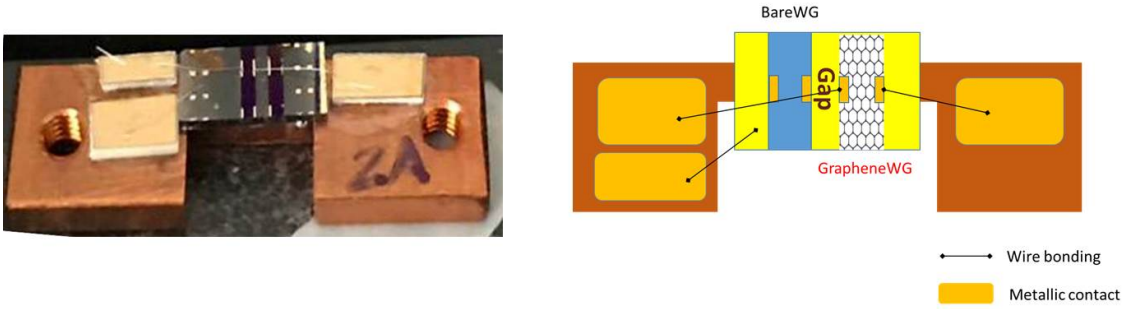

Fig. 5.5 *Left: A photography of the two waveguides of sample WG-2A. Right: Schematic image from top view of the chip composed of the two waveguides separated by a gap.*

5.2.1 THz time-domain spectroscopy system

THz time-domain spectroscopy (TDS) is a contact-free powerful technique for probing the electrical and optical properties in the THz spectral range of a wide range of materials such as 2D materials, metals and semiconductors[177]. Indeed, THz light allows for direct coupling to low-energy (meV scale) excitations such as the interaction of electrons, spins and phonons, as well as vibrational and rotational modes of molecules. This makes THz-TDS systems very attractive for a wide range of disciplines including physics, chemistry, engineering, astronomy, biology, and medicine. In our work, we use THz-TDS system for characterizing the properties of the modes propagating along the hybrid metal-semiconductor waveguides. To probe how these modes can be modulated by a graphene layer deposited on the top of their ridges, we modulate the gate voltage of the graphene layer and we use a double modulation technique explained in subsubsection b).

a) Experimental set-up

For this study, we use a THz-TDS system, which was developed by Sylvain Massabeau, a PhD of my research group. The THz-TDS system measures the time-resolved electric fields of THz radiation propagating through a sample and compared to a reference beam. Our system, illustrated in Figure 5.6, is based on an ultrafast optical laser that provides a set of femtosecond pulses centered around 800 nm with an average power of $\sim$ 300 mW. The optical pulse train is split to two arms, one arm illuminates a photoconductive antenna giving rise to a transient current that generates THz pulse train. The emitted THz pulse is collected and collimated by a parabolic mirror (P1) and then focused by another parabolic mirror (P2) onto the sample under investigation. A third parabolic mirror (P3) is used to collect the THz beam after passing through the sample and a fourth parabolic mirror (P4) focuses the THz electric field onto an electro-optic crystal. In the meantime, the second optical beam (probe beam) passes through a delay line that modifies the path length and is also focused onto the electro-optic crystal to synchronously probes the transient THz electric field.

Indeed, the quasi-static electric field of the THz signal interacts with the optical probe beam in the electro-optic crystal inducing a refractive-index difference between the ordinary and extraordinary ray of the optical probe beam after propagating through the crystal, expressed as:

$$\Delta n = \Delta n_0 + \Delta n_{E_{THz}}$$

with Δn_0 represents the intrinsic birefringence of the electro-optic crystal and $\Delta n_{E_{THz}}$ is induced by the THz electric field and follows the linear electro-optic effect:

$$\Delta n_{E_{THz}} = \frac{1}{2} n^3 r E_{THz}$$

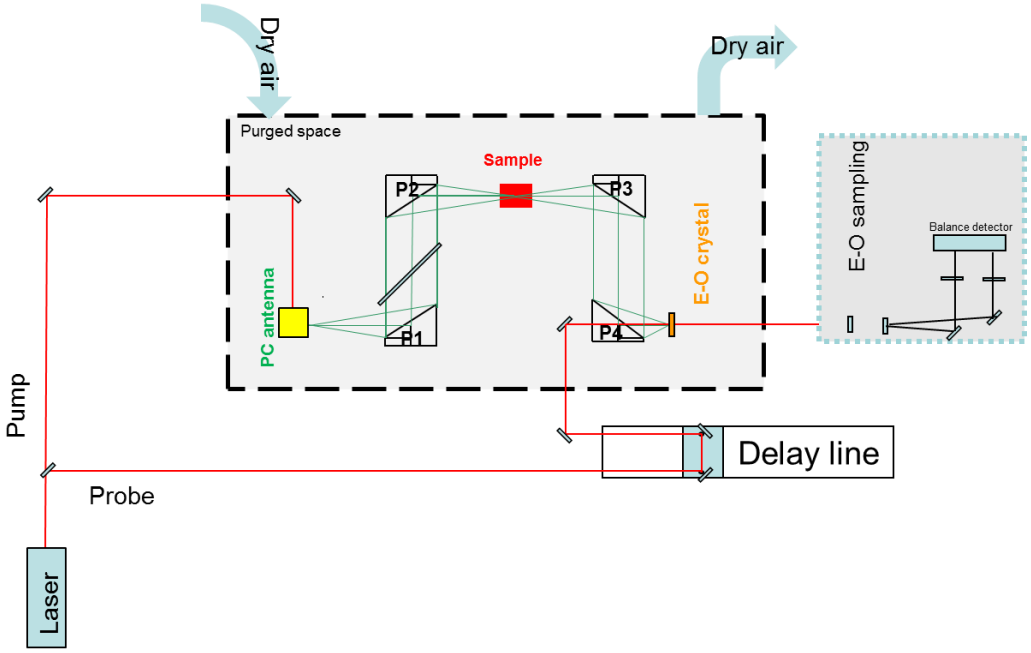

Fig. 5.6 *A schematic view of conventional THz-TDS setup .*

with r and n corresponds to the electro-optic coefficient and the unperturbed refractive index respectively. This refractive-index difference induces phase retardation that is proportional to the amplitude of the THz electric field. Then, by delaying the timing of the optical probe pulse to the optical pulse that drives the THz photoconductive emitter, the temporal waveform of the THz pulse incident on the electro-optic crystal is recorded with fs resolution. For the characterization of the hybrid dielectric-metal waveguides, we place them at the focus plane of the THz beam, i.e. in between the pair of the metallic parabolic mirrors, P2 and P3; the coordinate of the sample is set as shown in Figure 5.9, z as the propagation orientation, x and y are in the axis of the cross-section of the hybrid waveguides. Note that in the THz-TDS system, the THz beam is a transverse electromagnetic wave, linearly polarized, with the electric field parallel to the x-axis. Thus, the incident THz electric field is parallel to the width of the ridge for bare waveguides and to the graphene layer for graphene coupled waveguides.

Both the amplitude and the phase of the THz radiation are obtained by a Fourier transform of the recorder temporal waveform. For the detection of the temporal THz

waveform, we use two different electro-optic crystals, a ZnTe crystal of 1 mm-thickness and a GaP crystal of 200 µm thickness. The transient electric field measured with these two distinct crystals are reported in Figure 5.7a). The corresponding amplitude spectra obtained by Fourier transform calculation are reported in Figure 5.7b). We observe that the use of a ZnTe crystal allows detection up to $\sim$ 3.5 THz whereas the GaP crystal provides broader detection up to $\sim$ 7 THz. The S/N ratio of the experiment reaches up to 10^4 owing to the coherent detection technique as shown in Figure 5.7b). We also observe that the S/N ratio is higher at low frequency with a ZnTe crystal whereas it is higher with a GaAs crystal at high frequencies, as expected. The choice of the electro-optic crystal will depend on the S/N required in a specific spectral range. Since the amplitude and the phase of the THz electric field are recorded simultaneously, the complex refractive index of the sample under investigation is then directly obtained without requiring the use of Kramers-Kronig relation.

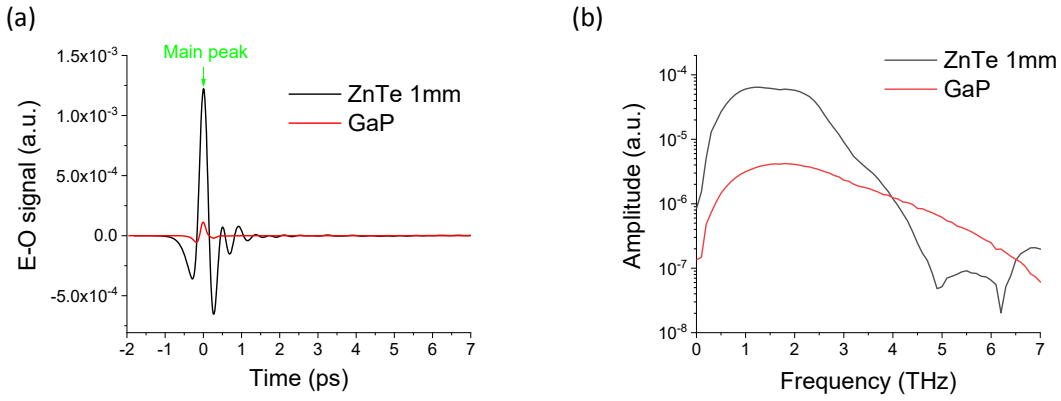

Fig. 5.7 *a) THz-TDS of 1mm-thick ZnTe crystal (black curve) and 200* µm*-thick GaP crystal (red curve). b) The corresponding amplitude spectra obtained by fast Fourier transform in logarithmic scale.*

b) Double modulation technique

We expect only a small proportion of the THz signal to be effectively modulated by the graphene layer due to the weak coupling between the incoming THz signal and the hybrid waveguides. Indeed, the THz beam size extends over a few hundreds of micrometers that is large compared to the typical dimensions of the cross-section of the waveguides and we do not use any coupling element. To overcome this issue, we combine a double modulation technique with the regular THz-TDS technique. First, let us consider the signal measured using a regular THz-TDS system (without double modulation technique). The THz pulse emitted by the photoconductive antenna is modulated by a square bias applied to the

photoconductive antenna with a period T_2 and with a duty cycle of 50%. Thus, the detected electro-optic signal is expressed as :

$$Signal_{THz} = \frac{A}{2} + \frac{4A}{\pi}\left(\sin(\omega_2 t) + \frac{1}{3}\sin(3\omega_2 t) + \frac{1}{5}\sin(5\omega_2 t) + ...\right)$$

where $\omega_2 = 2\pi f_2 = 2\pi/T_2$. The lock-in amplifier multiplies the modulated THz signal with a pure sine wave at the reference frequency f_2 given by the trigger signal of bias source of the photoconductive antenna. As all components of the THz input signal are multiplied by the reference locked to f_2, the detection will single out only the first component. It yields a DC output signal proportional to the component of the signal at frequency f_2; as a result, the measured electro-optic signal is $4A/\pi$.

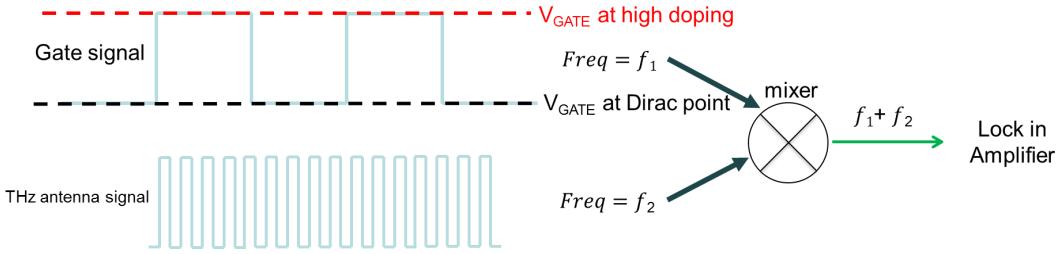

Fig. 5.8 *The schematic working principle of double modulation acquisition*

For the double modulation detection, the main idea is to apply an additional modulation that is, in our case, a square gate voltage V_{GATE} to the graphene layer with a period T_1 and a duty cycle of 50%; it induces a modulation of the chemical potential of the graphene layer. Then, we use a FPGA-based homemade frequency mixer(type: Nexys 3 FPGA Board) to sum up the fundamental frequency $f_2 = 1/T_2$ of the incoming THz signal with the fundamental frequency of the gate voltage applied to the graphene layer $f_1 = 1/T_1$. In this case, at the sum frequency $f_1 + f_2$, the $Signal_{DM}$ is written as:

$$Signal_{DM} = \frac{A'}{2} + \frac{4A'}{\pi}\left(\sin((\omega_1 + \omega_2)t) + \frac{1}{3}\sin(3(\omega_1 + \omega_2)t) + \frac{1}{5}\sin(5(\omega_1 + \omega_2)t) + ...\right)$$

So if the detection is locked to a reference signal at $f_1 + f_2$ (triggered by a TTL signal from the mixer), the output DC signal given by the lock-in amplifier is $\frac{4A'}{\pi}$. Under this condition, the detected electro-optic signal corresponds to the difference of the THz signals $Signal_{THz}$ at two different gate voltage values. Note that the low pass filter of the amplifier removes the signals and the noise at other frequencies. Since there is no signal when the gate voltage modulation does not affect the THz signal propagating along the waveguides, the sensitivity of the measurement is significantly improved.

5.2.2 THz characterization of the hybrid waveguides

a) Positioning the waveguide

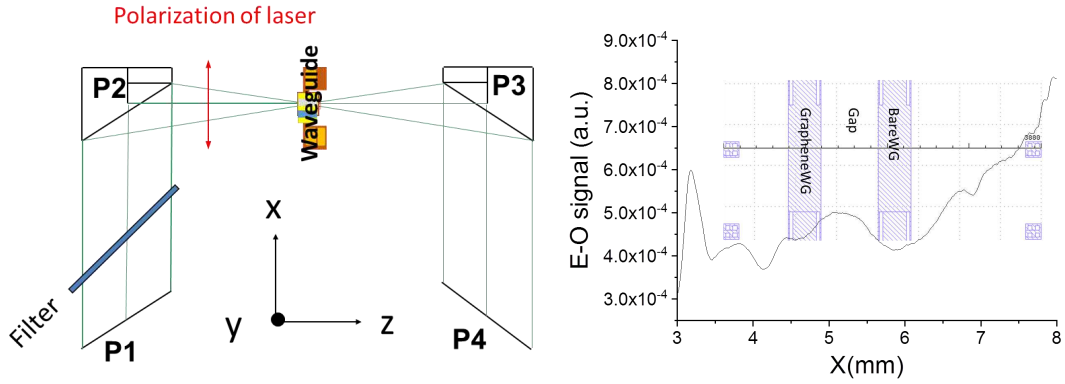

Fig. 5.9 *Left) A schematic image of scanning measurements based on THz-TDS system to place the hybrid waveguide based device at the focus of the THz beam and well centered. Right) Electro-optical line x-axis scan profile at zero delay measured at the focal point of the focused THz beam.*

As the THz-TDS system is based on THz radiation propagating in free space, the THz spot size at the focus, even if being diffraction-limited, is significantly larger than the waveguide dimensions. Consequently, for this study, the first critical step is to align the hybrid waveguide under characterization with the incident THz beam. The objective here is to place the waveguide-based device at the focus of the THz beam and in its center. We first measure the THz pulse without a sample, which provides a reference signal. Then by scanning the evolution of the main peak of the THz electric field as a function of the position of the waveguide as illustrated in Figure 5.9 (left), we determine the position at which the waveguide is located at the focus of the THz beam and well centered.

As an example, Figure 5.9 (right) reports the main peak of the electric field, i.e. the electro-optic signal at zero delay, as a function of the x-axis. We observe two deeps that we attribute to the alignment of the incident THz beam with the bare waveguide and the graphene waveguide. Indeed, the THz beam that is coupled to the waveguide encounters an additional delay compared to free space (since $n_{effWG} > n_{air} = 1$) and thus leads to a decrease of the electro-optic signal at zero delay. Thus, from the XYZ profile, we are able to position the waveguide samples well centered with regards to the THz beam for their optimized characterization in the time domain.

b) THz characterization of the bare and the graphene waveguides

Then, we focus on the temporal waveforms of THz pulses transmitted through the bare and the graphene waveguides. We start by measuring two distinct reference signals. Firstly, we measure the THz pulses fully propagating in the air and secondly the THz pulses after propagating along the gap in between the two waveguides. In this latter case, we estimate that typically half of the incident THz signal passes through the air and the other half passes through the GaAs substrate on which the waveguide is wafer-bonded.

The transient electric fields transmitted in the air, through the bare and graphene waveguides and also though the gap between the two waveguides of the sample WG-1A are reported in Figure 5.10. The measurement is performed within a time window limited to 21 ps after zero delay. We observe that the main peak of the THz signals transmitted through the gap and the two waveguides are half the value of the one propagating in the air. In addition, we observe a transmitted pulse for these three THz signals, 17 ps after the zero delay. We attribute this signal to the reflection of the THz pulse at the end facet of the GaAs substrate used for wafer bonding. Indeed, we can estimate the delay for one round-trip propagation of the THz pulse within the GaAs substrate to be expressed as

$$t_{delay} = \frac{(n_{GaAs} - n_{air})L_{WG}}{c} = 17.72\ ps$$

with $L_{WG} = 2$ mm the length of the waveguides of sample WG-1A, and $n_{eff} = 3.7$ the mean refractive index of GaAs material at THz frequencies. The amplitude of this signal transmitted through the GaAs substrate is relatively weak due to the absorption in the GaAs substrate and to the losses introduced by the gold layer on the top of the GaAs wafer (beneath the waveguides). Thus, the decrease of the main peaks at zero delay for the THz signals transmitted through the gap and the two waveguides compared to the one propagating in free-space is attributed to the transmission of a part of the THz signal through the GaAs wafer used for wafer bonding.

An important observation is that both THz signals passing through the graphene and the bare waveguides possess additional oscillations after the main peak compared to the two reference signals (Free space and Gap signals). These oscillations are more pronounced on the waveform transmitted through the bare waveguide. We can observe that these additional oscillations persist during more than 10 ps. We further analyze these measurements by calculating the corresponding amplitude spectra using fast Fourier transform and a time windowing lower than 17 ps to not include the echo observed at 17 ps. The amplitude spectra of the THz pulses propagating through the gap between the two waveguides, through the bare and graphene waveguides are reported Figure 5.11. We

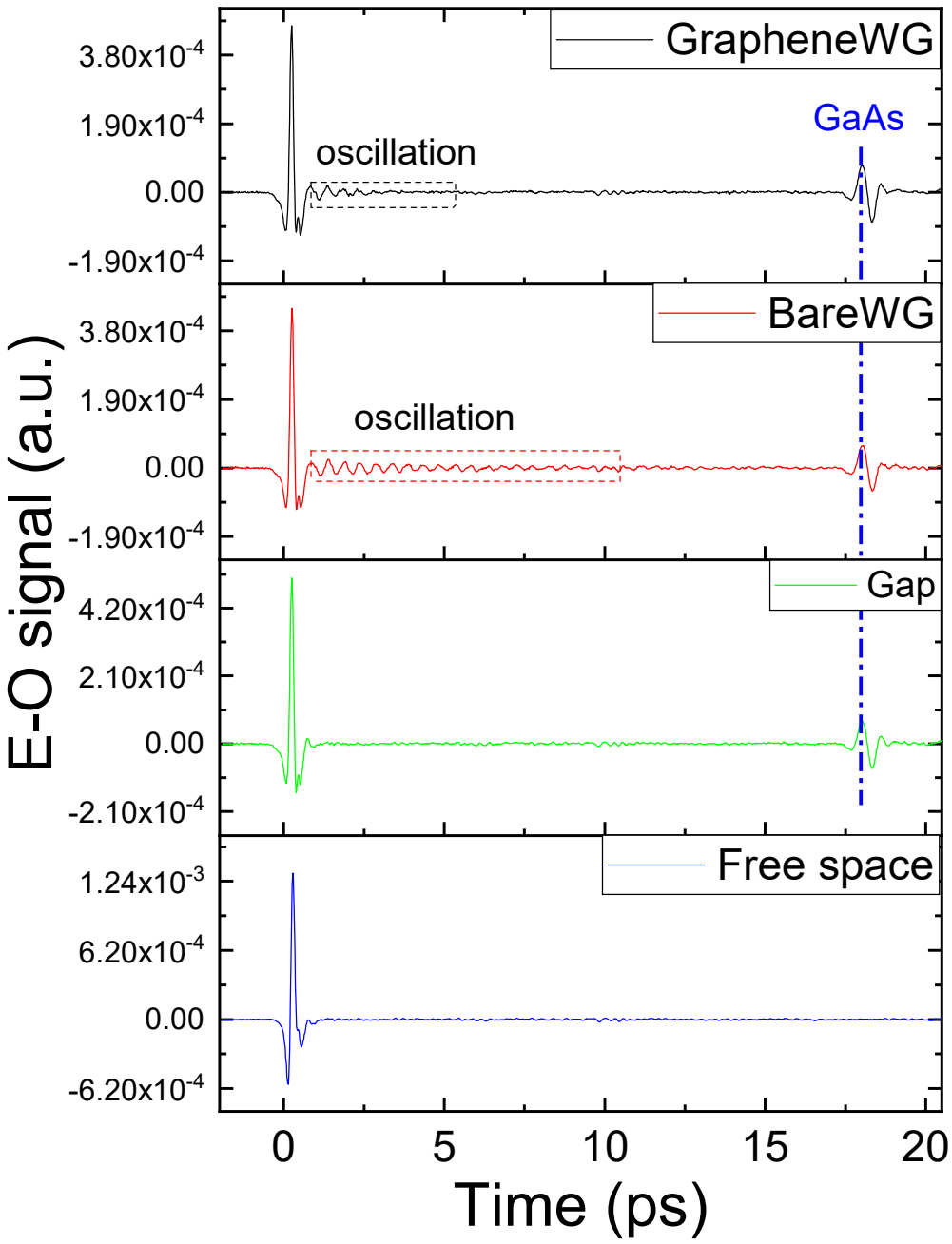

Fig. 5.10 *THz-TDS in graphene waveguide, bare waveguide, substrate between two waveguides and free space on sample WG-1A.*

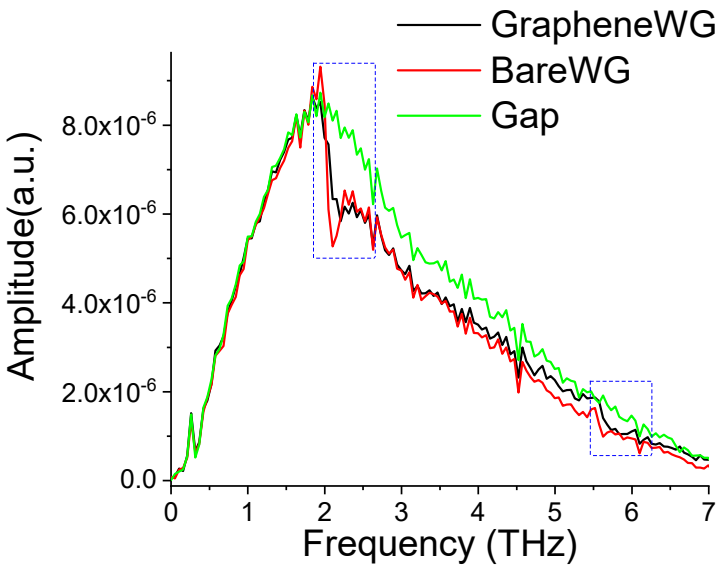

Fig. 5.11 *Amplitude spectra of waveguide WG-1A in graphene waveguide, bare waveguide , and gap.*

observe a decrease of the amplitude spectra of the THz pulses propagating through the waveguides above 2.1 THz. We also observe two deeps at frequencies of 2.1 THz and 5.6 THz.

Further, we probe other waveguide-based samples with different widths and the same height. We observe similar tendencies in all samples we tested. As an example, Figure 5.12 shows the transient THz pulses measured in WG-600-2-2500; the temporal oscillations are also clearly observed after the main peak. As well, the amplitude spectra, reported in Figure 5.13 show quite similar features: an absorption at frequencies higher than 2.1 THz for the graphene waveguide and two deeps at 2.1 THz and 5.6THz. We expect an uncertainty in positioning the waveguides during the experiment that could be responsible for the absence of the broad absorption at frequencies higher than 2.1 THz for the bare waveguide.

The two deeps observed at 2.1 THz and 5.6 THz can be related to the cut-off frequencies of the quasi-TE modes propagating along these hybrid waveguides. Indeed, Comsol simulation predicts that for a height of 11 µm, the low cut-off frequencies of the TE_0 mode is around 2.1 THz. As a result, the coupling of the incident THz pulses to the waveguides can occur only at frequencies $>$ 2.1 THz. This is consistent with the observation of the decrease of the spectra amplitude above 2.1 THz since the waveguides introduce losses compared to free space propagation. The simulation also predicts the existence of TE_1

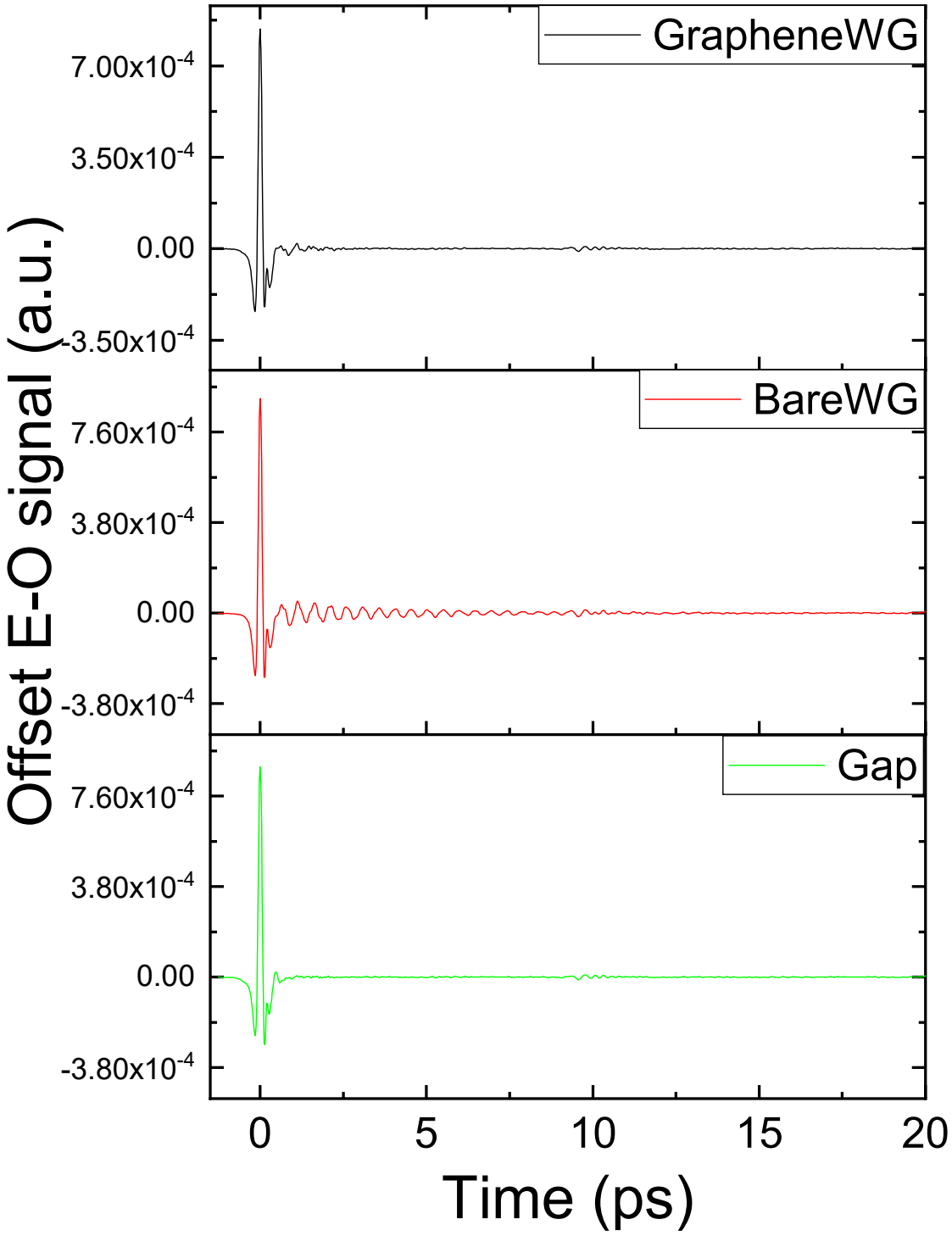

Fig. 5.12 *Transient temporal signal in graphene waveguide, bare waveguide, and gap of waveguide sample WG-600-2-2500.*

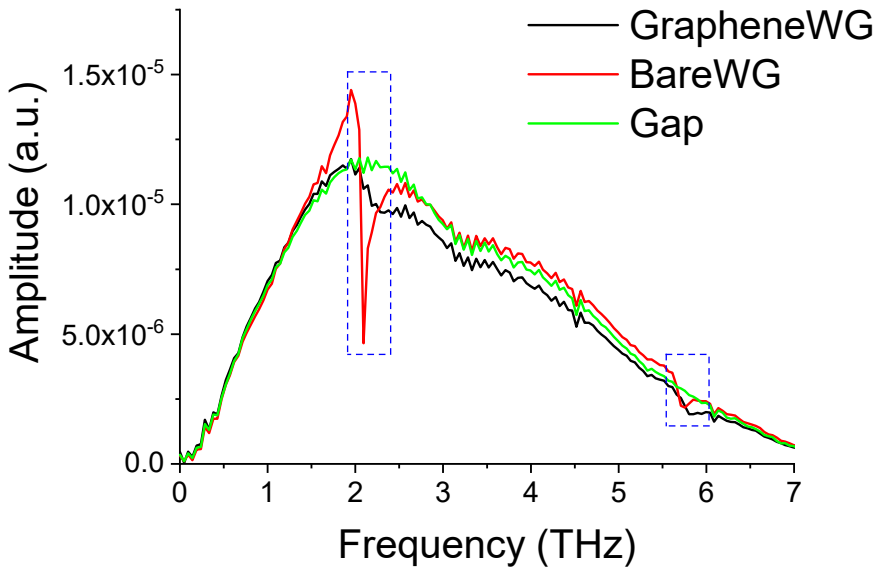

Fig. 5.13 *Spectra of sample WG-600-2-2500 transformed from 20ps time window.*

mode as discussed later and illustrated in Figure 5.23. This TE_1 mode exists at wavelength smaller than $\lambda < \frac{4hn_{eff}}{3}$, corresponding to a low cut-off frequency around 6 THz. The observation of two deeps at the same frequencies for all samples of different widths but the same height is consistent with the fact the cut-off frequencies of both TE_0 and TE_1 modes depend only on the height of the waveguides.

c) THz characterization of gate-modulated graphene waveguides

We now investigate the impact of the chemical potential of the graphene on the propagation of the THz electric fields. For this purpose, we use a double modulating detection technique. We apply a square gate voltage to the graphene layer with a fundamental frequency $f_2 = 416$ Hz and we detect the electro-optic signal at the sum frequency $f_3 = f_1 + f_2$ with $f_1 = 35$ kHz, the fundamental modulation frequency of the photoconductive antenna. Such a technique is very sensitive since no THz signal is recorded if not being modulated by the gate voltage. Using this technique, we can measure the modulation of the THz electric fields propagating along the waveguides, induced by the modulation of the graphene chemical potential. We measure the electro-optic signal at f_3 after passing through the graphene covered waveguide. Figure 5.14 displays the electro-optic signal recorded with a square gate voltage that tunes periodically the graphene chemical potential from close CNP to a high doping value (black curve). As a reference, the electro-optic signal recorded after passing through the bare waveguide is reported in

the red curve. Note that we added a Polyethylene filter in the THz path to block the specular infrared light incident on the graphene covered waveguide. As a result, we overcome any optical excitation in the GaAs waveguide[178].

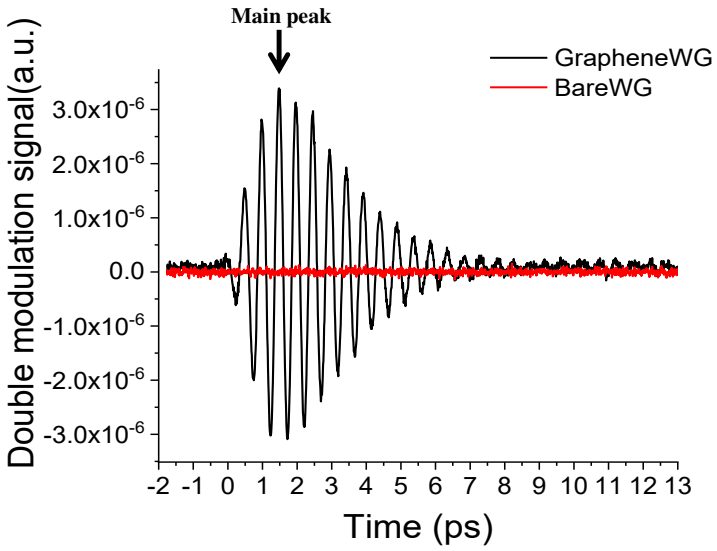

Fig. 5.14 *Electro-optic signals detected at f_3 of THz pulses transmitted by the graphene coupled waveguide and the bare waveguide with similar same gating condition.*

We observe large oscillations in the electro-optic signal when the graphene coupled waveguide is centered in the incident THz beam and no detectable signal when the bare waveguide is centered in the incident THz beam. Both waveguides are gated in the same condition synchronously. We set the time delay at the main peak of the oscillating signal and run an x-axis profile along the front facet of the waveguide. We observe in Figure 5.15 that the electro-optic signal follows a gaussian shape with its maximum at the position of graphene waveguide. The FWHM of the Gaussian shape is 500 µm, which is consistent with the convolution of the THz beam profile and the waveguide width of 400 µm. From these measurements, it is clear that there is no modulated signal from the bare waveguide. Thus, the modulated signal is fully provided by the graphene layer on the top of the waveguide. By analyzing the amplitude spectra of this electro-optic signal detected at f_3, we observe two peaks at 2.1 THz and 5.6 THz(see Figure 5.16) corresponding to the two deeps previously observed in the spectra of Figure 5.11 and Figure 5.23. The signal is zero at the other frequencies indicating the gate voltage modulation only impacts these two deeps within the sensitivity of our THz-TDS system.

We further investigate how the electro-optic signal modulated at f_3 evolves as a function

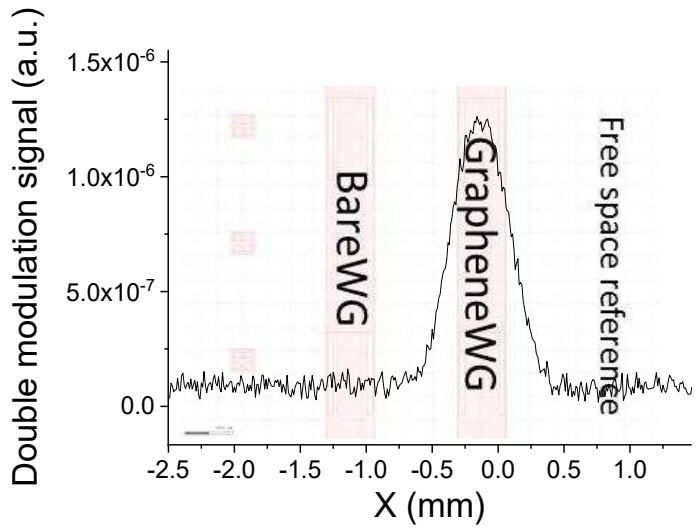

Fig. 5.15 *The x-axis profile at the main peak of electro-optic signals detected at f_3.*

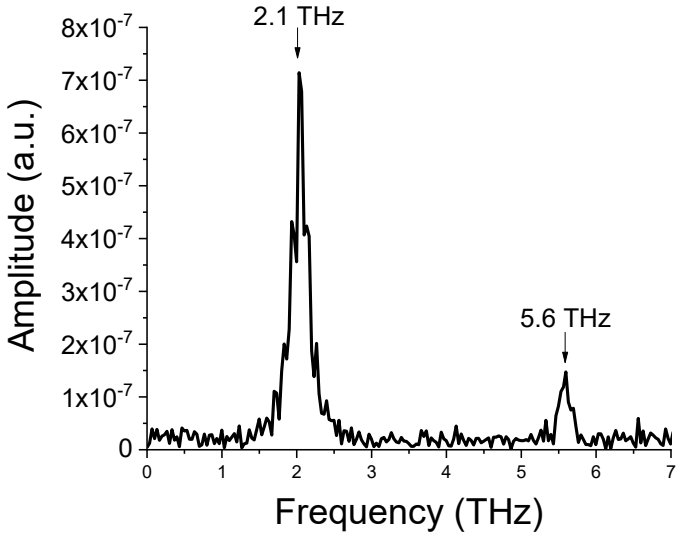

Fig. 5.16 *The spectra of a double modulated THz time-domain signal on sample WG-400-1-2500 which has two peaks at 2.1 THz and 5.6 THz*

of the modulation amplitude of the gate voltage applied to the graphene layer. We apply different modulation amplitudes on the WG-400-1-2500 sample. The gate voltage is modulated from a constant low value defined by V_{CNP} to a varying higher gate voltage value V_{GATE}. We observe in Figure 5.17a that only the amplitude of the electro-optic signal at f_3 is increased as the amplitude of the gate voltage modulation is increased. The delay, as well as the periods of the oscillations, are constant for all applied gate voltage modulation. In the frequency domain, it results in an increase of the peak locating at 2.1 THz with the increase of the gate modulation as observed in Figure 5.17b. The maximum signal corresponds to $V_{GATE} = 9\ V$. The increase in peak at 5.6 THz is not very clear due to the noise.

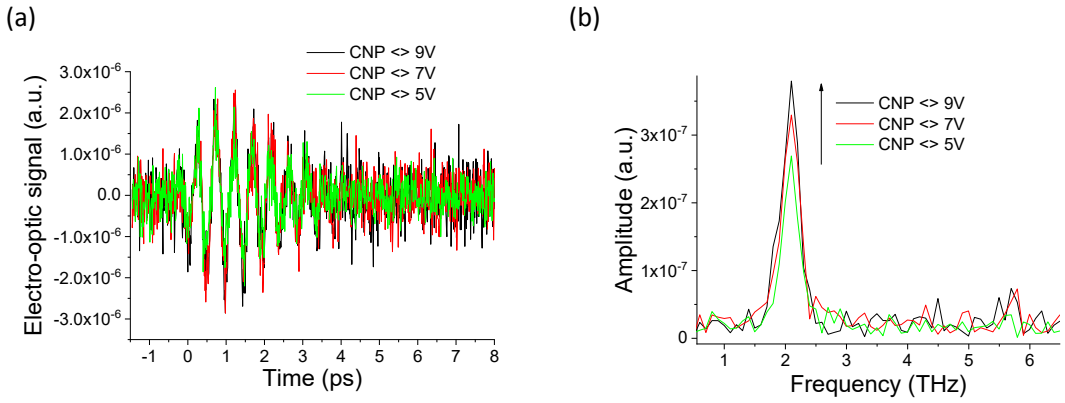

Fig. 5.17 *a) Electro-optic signals detected at f_3 of the THz pulses transmitted by the graphene coupled waveguide under different chemical potential modulation, (V_{CNP} ⇔5V, V_{CNP} ⇔7V, V_{CNP} ⇔9V) b) Corresponding amplitude spectra of electro-optic signal in Fig(a).*

To investigate the relation between the magnitude of chemical potential modulation and the amplitude of the electro-optic signals measured with the double modulation technique, we report on Figure 5.18a the electro-optic signal at the peak measured at f_3 and the resistance of the graphene layer coupled to the waveguide as a function of $V_{GATE} - V_{CNP}$. We observe that the two curves have the same monotonicity on the two doping sides and their maximum both locate at the CNP. We attribute the asymmetry of the curves between the two doping sides to the asymmetry of the doping efficiency resulting from the large area of monolayer graphene.

From the gate-dependence resistance, we are able to extract the intraband conductivity of the graphene layer using the relation $\sigma = \frac{L}{W(R-R_c)}$, where L = 250 µm is the distance between two electrodes on the graphene surface, W=700 µm is the width of an electrode and R_c is the sum of contact resistance that we estimate to 400 Ω. The estimated

intraband conductivity of the graphene layer is shown by the red curve in Figure 5.18b. The blue curve in Figure 5.18b is the intraband conductivity calculated by Equation(4.1) at T = 300K and $\tau = 12.8\ fs$. We observe that the tendencies of all the curves are remarkably similar, providing evidence that the graphene layer modulates the two deep peaks observed in the THz spectra.

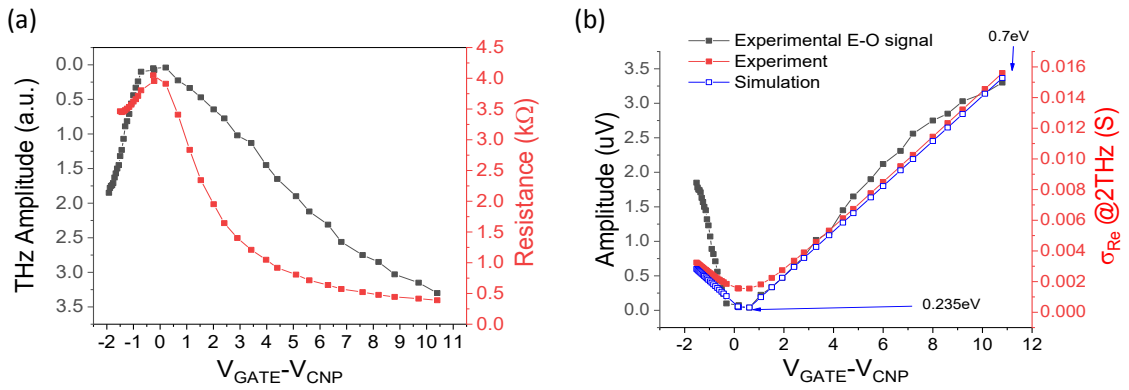

Fig. 5.18 *a) The amplitude of double modulated signal at main peak (black line) and the resistance (red line) as function of $V_{GATE} - V_{CNP}$ of the graphene coupled waveguide 400-1-2500. b) The amplitude of double modulated signal at the main peak (black line) and the real part of the optical conductivity at 2 THz obtained from the experiment (red line) and calculation (blue line) as a function of $V_{GATE} - V_{CNP}$.*

5.2.3 Interpretation based on interference effect

We now turn to the investigation of the origins of these experimental observations and the absorption observed in amplitude spectra above 2.1 THz and the two deeps at 2.1 THz and 5.6 THz. As discussed previously, the simulation results predict that the low cut-off frequency of the TE_0 mode for waveguides of 11 µm height of 2.1 THz. As a result, we attribute the decrease of the transmission spectra above 2.1 THz to the THz field coupled to the bare and graphene waveguides that introduce some losses. As these broad losses are not modulated by the gate voltage modulation, we attribute them to the intrinsic losses of the hybrid waveguides, which result from the intrinsic losses of the GaAs material of the strip and to the metal layer. These losses by the imaginary part of the effecitve index of the bare waveguides are predicted to be in the range of 3dB/mm (see chapter 4).

To explain the additional oscillations observed in time domain measurements, which

result in the two deeps at 2.1 THz and 5.6 THz, we investigate a possible interference effect. To explore such physical mechanism, we calculate the electric fields after propagating through the waveguides. For this calculation, it is important to consider that the coupling efficiency of the incident transverse electromagnetic fields with the waveguides is weak. Indeed, as mentioned previously, we do not use any coupling element, such as Si lens, whereas the THz beam size extends over a few hundreds of micrometers that is large compared to the dimensions of the cross-section of the waveguides. As a result, parts of the incident THz field are not coupled to the waveguides and propagate through the air above the waveguide on one hand and through the GaAs substrate below the waveguide on the other hand (see Figure 5.19). These two parts of the incident THz beam not coupled to the waveguides can be estimated by studying the THz signal measured after propagating in the gap between the waveguides. Indeed, the part of the THz radiation that propagates through the air above the metallic layer corresponds to the transient electric field recorded around zero delay and the part of the THz radiation that propagates through the GaAs wafer beneath the waveguide corresponds to the transient electric field recorded 17 ps after zero delay. To eliminate the part of the signal that propagates through the GaAs substrate, we consider in the calculation only the transient THz signal within the first 15 ps after the zero delay. This transient THz signal within the first 15 ps after the zero delay, E_{Gap}, which propagates in the air above the metallic layer, is the THz radiation that can be coupled to the waveguides. Thus, we assume that the THz electric field incident onto the waveguides is $E_{inc} = E_{Gap}$.

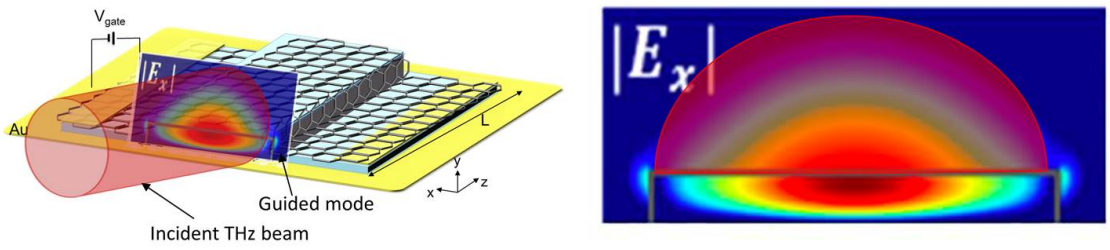

Fig. 5.19 *Left: Schematic image of the large THz beam incident onto the hybrid waveguide. Right: Cross-section of the hybrid waveguide: the main component of the quasi-TE mode, $|E_x|$, can interfere with the part of the THz beam not coupled to the waveguide that propagates in the air above the waveguide (red area).*

As the incident THz beam, E_{inc}, extends over larger dimensions than the cross-section of these waveguides, its coupling efficiency to the hybrid waveguide has to be carefully considered in the calculation. The coupling efficiency strongly depends on the spatial ex-

tension of the modes as it relies only on mode matching between the incident THz beam and the quasi-TE mode of the hybrid waveguides. To get insight into this coupling, we use Comsol simulation to calculate the spatial extension of the quasi-TE mode above the waveguides as a function of frequency. Figure 5.20 reports the spatial distribution above the waveguide (along the y-axis) of the main component of the quasi-TE mode, $|E_x|$. We clearly see that the spatial extension of the mode strongly depends on the frequency, with larger extension as the frequency is decreasing and get closer to the cut-off frequency of the waveguides. From this evolution, we extract in Figure 5.20 (right) the distance, $r_{1/e}$, that separates the top surface of the waveguides where $|E_x|$ is maximum and the position where $|E_x|$ is reduced by a factor at 1/e. We found that $r_{1/e}$ ranges from $70\mu m$ to $7\mu m$ as the frequency is increasing from 2.1 THz to 6 THz.

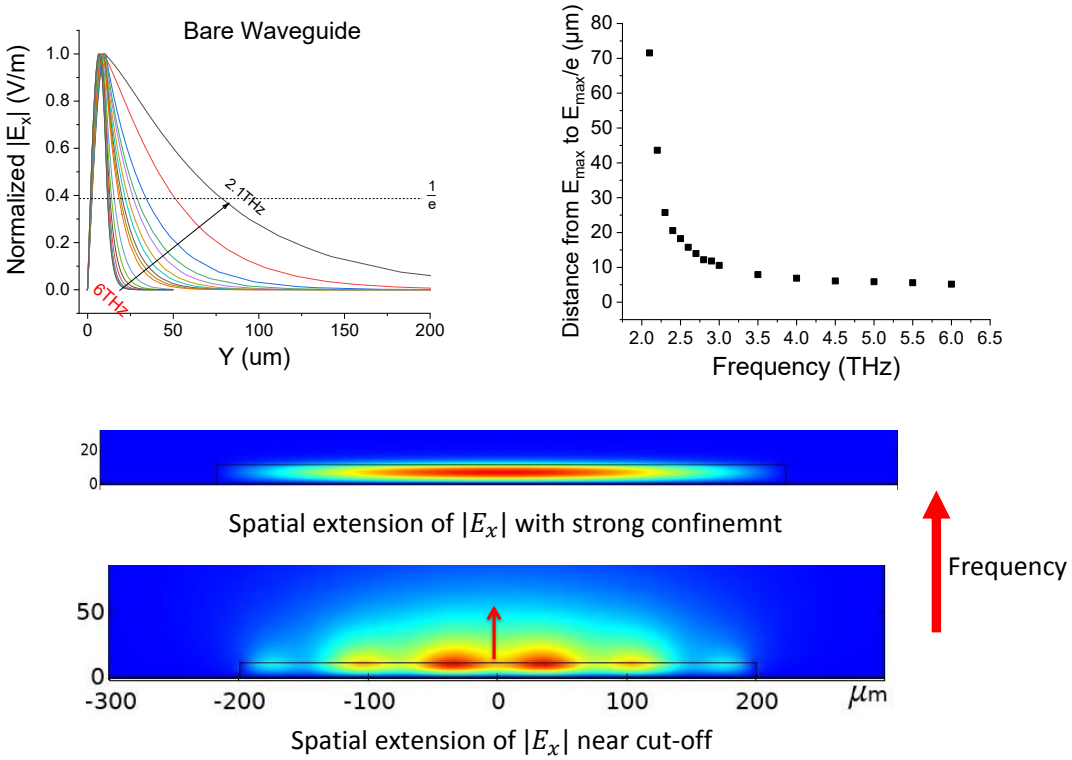

Fig. 5.20 *Left: Normalized $|E_x|$ of quasi-TE mode at the center of waveguide as a function of y-axis calculated using Comsol simulation. Right: The distance from max $|E_x|$ to max E_x/e as the function of frequency. Bottom: Two patterns of the spatial extension of $|E_x|$ for quasi-TE mode near the cut-off frequency, 2.1 THz (bottom) and at 6 THz (up).*

To include this spatial extension in the calculation, we introduce the parameter $C(\omega)$

given by $C = \frac{r_{1/e}}{r_{1/e\,@\,2.1THz}}$, which reflects the dependence of the spatial extension of the electric field with the frequency. $C(\omega)$ is the extension of the electric field normalized by its value at 2.1 THz when the extension of the mode is the highest. The values of C are directly obtained from the Comsol simulation. The proportion of the incident THz electric field that is coupled to the quasi-TE mode of the waveguides is expressed in the calculation by the product $a \cdot C(\omega)$, with a an adjustable parameter independent of the frequency. Let us now calculate the THz electric field after propagating through the bare waveguide placed at the center of the incident THz beam. The complex electric field $\widetilde{E}_{Bare}(\omega)$ is given by:

$$\widetilde{E}_{Bare}(\omega) = (1 - a \cdot C(\omega)) \cdot \widetilde{E}_{inc}(\omega) + a \cdot C(\omega) \cdot \widetilde{E}_{inc}(\omega) \cdot e^{\frac{\omega(\widetilde{n}_{eff} - n_{air}) \cdot L}{c}} \tag{5.1}$$

where $\widetilde{n}_{eff}$ is the effective index of the quasi-TE mode propagating within the bare waveguide. Note that a is the only adjustable parameter in the calculation. We perform numerical inverse Fourier transform to calculate the transient electric field of the complex expression we obtained in the frequency domain.

The confrontation between the calculated transient electric fields and the data are reported in Figure 5.21 for the samples WG-1A. The calculation is shown for two distinct values of a, a = 0.39 and a = 0.27. We observe that the calculation (red curves) well reproduce the oscillations observed (blue curve) after the main peaks at zero delay for both samples. This good agreement demonstrates that the interaction of the THz electric fields with the bare waveguide is well described by this interference signal between a part of the THz beam propagating above the waveguide and a part of THz pulse propagating through the waveguide. In the amplitude spectra reported in Figure 5.21b), the calculation (red line) also well reproduces the deep observed at 2.1 THz (blue curve), confirming that interference effect is dominating at this frequency. The decrease of the spectra above 2.1 THz is also well reproduced showing that the broad absorption is due to the intrinsic loss of the hybrid waveguide. This analysis demonstrates that the hybrid waveguide devices act similarly to a Mach-Zehnder interferometer with one arm being the THz signal above the waveguide and the other arm being the THz signal propagating through the waveguide. This constitutes an important result of this work since Mach-Zehnder interferometer based devices operating at THz frequencies could have a large impact on THz technology by opening new perspectives for on-chip THz interferometry and THz modulation.

We found similar tendencies from the confrontation between the calculated transient electric fields and the data obtained with the samples WG-600-2-2500 as reported in Fig-

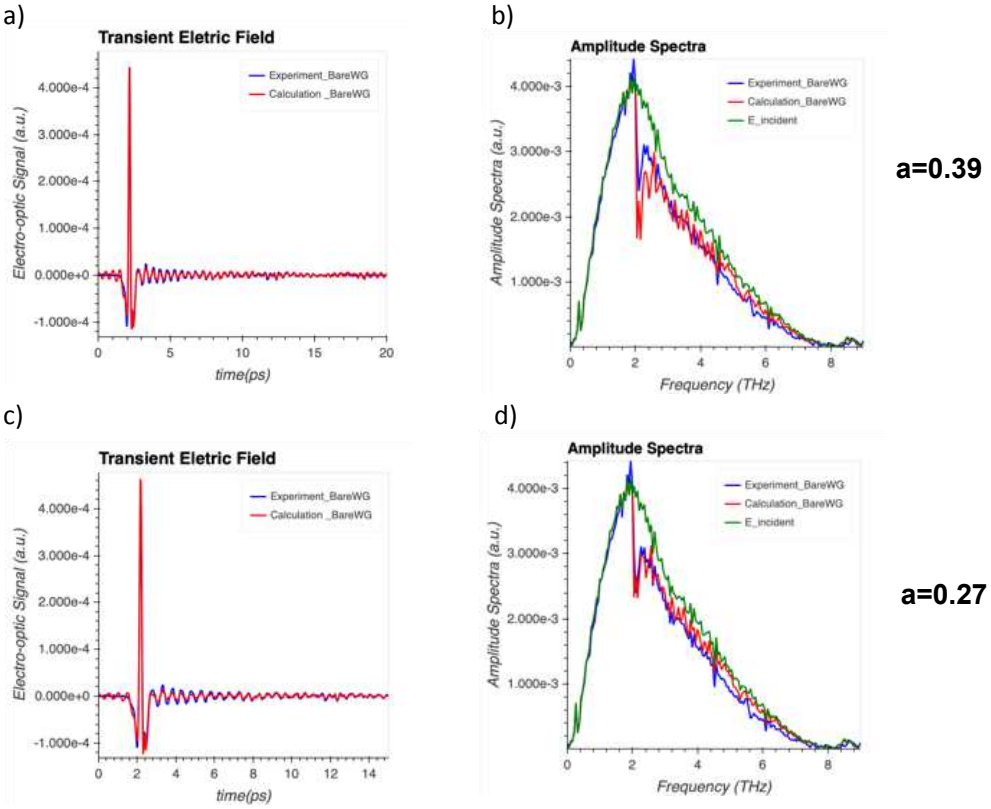

Fig. 5.21 *a) and c) are the experimental waveforms (blue lines) and calculated waveforms of the THz pulses using Equation*(5.1) *of sample WG-1A using parameter* $a = 0.39$ *and* $a = 0.27$ *respectively. b) and d) are the spectra corresponding to a) and c) respectively and the incident spectrum is reported in green curve as reference.*

ure 5.21, supporting the validity of our analysis. The effect related to Mach-Zehnder interferometer is thus confirmed.

In return, the deep at 5.6 THz does not appear in the calculated spectra. We attribute this deep to the interference of the incident THz beam with a quasi-TE_1 mode. Indeed, the cut-off frequency of the TE_1 mode is close to 6 THz and at the cut-off frequency, the extension of the mode above the waveguide is expected to be quite significant, as observed on Figure 5.23. Further developments are ongoing to include the interference of the incident THz beam with the quasi-TE_1 mode to reproduce by calculation the observed deep at 5.6 THz.

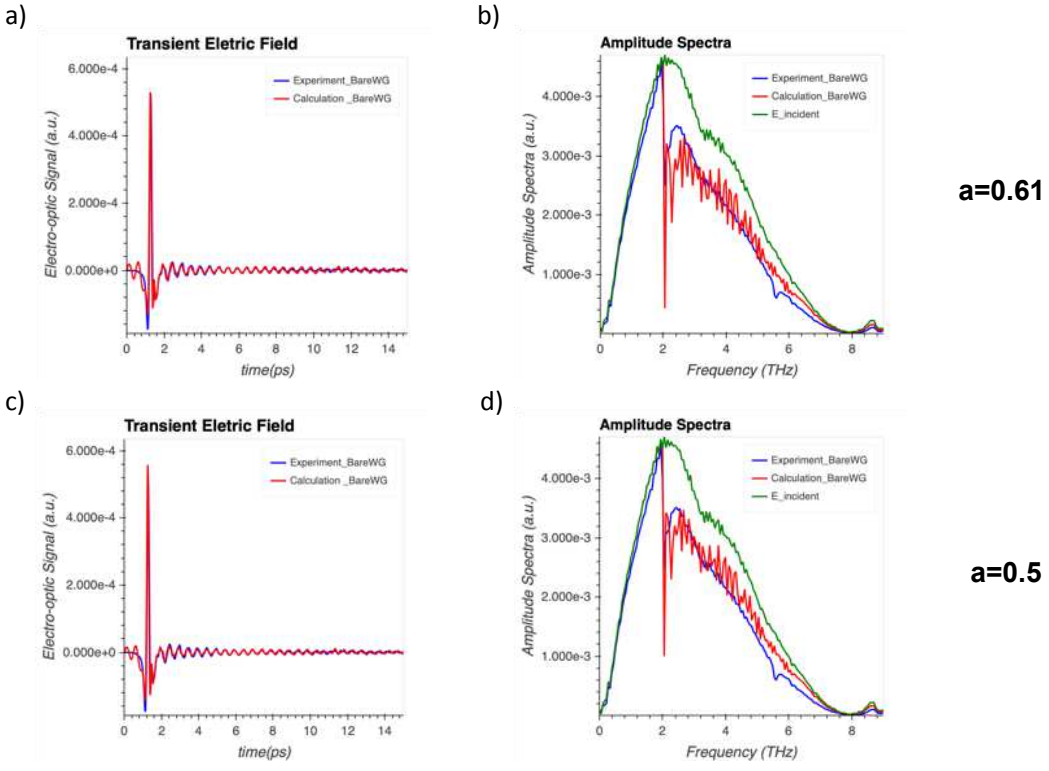

Fig. 5.22 *a) and c) are the experimental waveforms (blue lines) and calculated waveforms of the THz pulses using Equation(5.1) of sample WG-600-2-2500 with parameter a = 0.61 and a = 0.5 respectively. b) and d) are the spectra corresponding to a) and c) respectively and the incident spectrum is reported in green curve as reference.*

a) THz characterization of gated graphene waveguide

Our calculation will be used to interpret the data obtained for the graphene coupled waveguides. For the calculation, the coupling efficiency $a'C'$ and the effective index of the mode $\widetilde{n}_{eff}$ must be modify due to the presence of the graphene layer on top of the waveguides.

$$\widetilde{E}_{Graphene}(\omega) = (1 - a' \cdot C'(\omega)) \cdot \widetilde{E}_{inc}(\omega) + a' \cdot C'(\omega) \cdot \widetilde{E}_{inc}(\omega) \cdot e^{\frac{\omega(\widetilde{n}_{eff} - n_{air}) \cdot L}{c}}$$

Since the gate voltage applied to the graphene layer modifies both $\mathrm{Re}(\widetilde{n}_{eff})$ and $\mathrm{Im}(\widetilde{n}_{eff})$, it is expected that modulating the gate voltage will modulated this interference effect. Indeed, interference effect is strongly sensitive to the effective index of the propagating mode. We simulate using Comsol software, the mode effective index for two

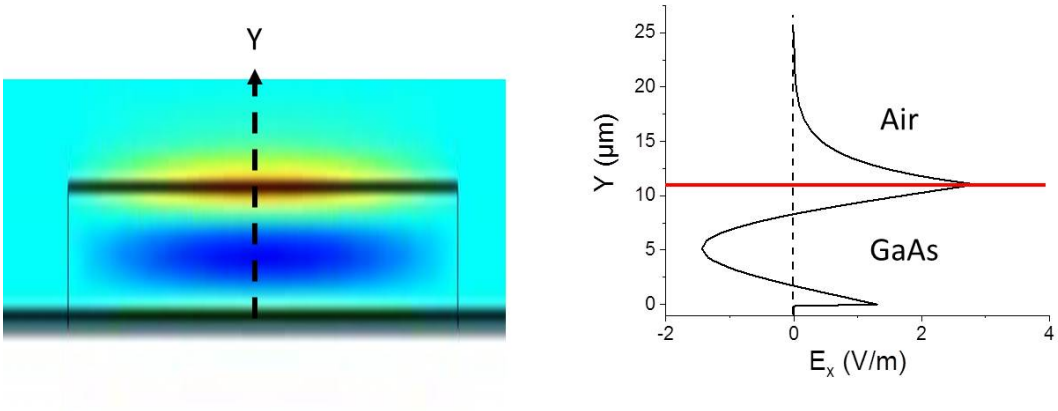

Fig. 5.23 *Left: Surface map of the spatial distribution of E_x calculated using Compsol software for the quasi-TE_1 mode at 6 THz. Right: 1D plot of E_x of quasi-TE_1 mode at 6THz as the function of y axis, the maximum of the electric field locates at the graphene position.*

distinct chemical potential in the graphene layer. For $\mu = 0\ meV$, the quasi-TE mode has an effective index $n_{eff} = 3.3465 - 0.0031066i$ at 5.8 THz; for $\mu = 200\ meV$ which is equivalent to high doping graphene, we observe two quasi-TE_1 mode with effective indices $n_{eff} = 3.3531 - 0.007782i$ and $n_{eff} = 3.4282 - 0.006796i$ at 5.8 THz and 6 THz respectively. Such change is expected to induce the modulation of the interference effect observed using the double modulation technique. Further analysis is on-going to provide a clear comparison.

In summary, our waveguides are as a Mach-Zehnder modulator with act similarly to a Mach-Zehnder interferometer with one arm being the THz signal above the waveguide and the other arm being the THz signal propagating through the waveguide.

5.3 Conclusion and perspectives

In this chapter, we experimentally analyze bare hybrid metal-GaAs waveguides and their coupling to a graphene monolayer using THz TDS spectroscopy. The fabrication of the devices were performed by Alessandra Digaspare and Miriam Vitiello from NEST, Istituto Nanoscienze – CNR and Scuola Normale Superiore (Italy. We perform Raman spectroscopy on the CVD graphene monolayer and electrical characterization of the graphene coupled hybrid waveguides as a preliminary characterization. Then, we analyze the propagation of the THz pulses propagating along these waveguides over a broad spectral range. We show that the THz pulses passing through bare and graphene-coupled waveguides pos-

sess long additional oscillations after the main peak compared to reference THz pulses. In the frequency domain, we show a broad absorption above 2.1 THz and the two deeps at 2.1 THz and 5.6 THz. We demonstrate that modulating the chemical potential of the graphene directly modulates the amplitude of the two deeps at 2.1 THz and 5.6 THz. Based on the calculation, we attribute these experimental observations to the interference of a part of the incident THz electric field propagating in the air (not coupled to the waveguide) and the THz electric field coupled to the waveguide. This interference effect can be modulated by the graphene layer via the modulation of its chemical potential. The interference effect is more pronounced at the cut-off frequencies, 2.1 THz and 5.6 THz, because at these frequencies specifically, the mode extension above the waveguides is large, resulting in a better overlap with the part of the electric field not coupled to the waveguides. In conclusion, these hybrid waveguide base devices act similarly to a Mach-Zehnder interferometer with one arm being the THz signal above the waveguide and the other arm being the THz signal propagating through the waveguide. The demonstration of such functionality is novel and opens very promising perspectives for THz interferometry and THz modulation. Moreover, our approach relies on well-mastered technological techniques for fabrication, it does not require incorporating the graphene into the core of a dielectric waveguide and is compatible with CMOS and THz quantum cascade lasers technologies. As a perspective, we plan to use the Si lens to improve the coupling of the incident THz pulses with the hybrid waveguides. We will also extend the study to other 2D materials to be coupled to these hybrid waveguides.

Chapter 6

General conclusion and perspectives

THz radiation is extremely attractive for fundamental investigations of matter and emerging applications including, for example, security screening, medical imaging, and spectroscopy. However, the THz spectral range remains one of the least exploited spectral regions, mainly due to the lack of compact powerful THz sources/amplifiers and passive devices. In this thesis work, we have investigated the potential of graphene as an active material for future developments of THz sources and amplifiers that involves radiative interband transitions. We have also studied the potential of graphene for the development of THz modulators. This works contains two main projects.

In the first project, we focus on the carrier lifetime in neutral graphene/hBN van der Waals heterostructures under mid-infrared illumination. In chapter 2, we present a phototransistor made of an hBN/graphene heterostructure of dimension $L \times W = 20$ µm $\times$ 10.4 µm, with residual density n_0 of $\sim 4 \times 10^{14}$ cm^{-2} ($\sim$ 20 meV) and an electron and hole mobility of 3.2 $m^2/(V \cdot s)$. We have shown that at low temperature and at CNP, the current flowing through these devices is dominated by ZKT. Thus at finite bias, there are non-equilibrium electron-hole pairs in the graphene channel of the phototransistor; the dc bias acts as an electrical pumping of the graphene/hBN heterostructures.

Then we use photocurrent as an interesting probe to investigate the recombination process of non-equilibrium carriers created by optical pumping. Using mid-infrared photoconductivity measurements, we have investigated recombination processes of carriers photoexcited at low density and energy in the graphene/hBN phototransistors. We have shown remarkable long carrier lifetime $\sim$ 30 ps, in quasi-intrinsic graphene, ultimately limited by interband Auger processes. By igniting the hyperbolic phonon polaritons in hBN via an electrical or optical pump, we demonstrate that the carrier lifetime is switched from $\sim$ 30ps down to few picoseconds. Furthermore, we have investigated the interplay

between optical and electrical pumping and demonstrated the opto-electrical pumping of HPhPs in the hBN layer at high Joule power and high optical power.

As a perspective of this first project, we will investigate recombination processes for non-equilibrium carriers at low density and energy in bilayer graphene. Our motivation is that the electronic dispersion relation in bilayer graphene is no more linear leading to different (larger) Auger recombination efficiency. This should affect the recombination time of the non-equilibrium carriers. We will also probe the spontaneous photon emission in the THz spectral range from these graphene/hBN heterostructures excited by mid-infrared laser light. Indeed with carrier lifetimes as long as 30 ps, we expect the spontaneous emission to be detectable by a Fourier transform spectrometer coupled to a bolometer. Furthermore, we will probe other heterostructures and materials such graphene-WSe_2 heterostructures, topological insulators and black phosphorus to provide unique basic physic knowledge on the carrier recombination processes in these materials. Besides, these works on the pumping of HPhPs in the hBN layer could promote graphene/hBN heterostructures as a platform for phonon polariton optics and nanoscale thermal management.

The second project reports an original device based on hybrid metal-dielectric waveguides coupled to a graphene monolayer. In chapter 5, we numerically investigate the fundamental quasi-TE and quasi-TM modes propagating along these hybrid metal-dielectric waveguides and show that owing to the metallic layer, the strength of in-plane electric field components of the propagating modes is maximized at the top of the dielectric strip on which the 2D material is deposited. Our study predicts 100% modulation of the THz light by tuning the chemical potential of the graphene layer coupled to a 1 mm-long hybrid metal-dielectric waveguides, which is very attractive for the development of THz modulators. We also show the potential of coupling undoped graphene multilayers to these hybrid metal-dielectric waveguides for achieving lasing at THz frequencies.

In chapter 5, we experimentally analyze bare hybrid metal-GaAs waveguides and their coupling to a graphene monolayer using THz TDS spectroscopy. We show that the THz pulses passing through bare and graphene-coupled waveguides possess long additional oscillations after the main peak compared to reference THz pulses. In the frequency domain, we show a broad absorption above 2.1 THz and the two deeps at 2.1 THz and 5.6 THz. We demonstrate that modulating the chemical potential of the graphene directly modulates the amplitude of the two deeps at 2.1 THz and 5.6 THz. Based on the calculation, we attribute these experimental observations to the interference of a part of the incident THz electric field propagating in the air (not coupled to the waveguide) and the

THz electric field coupled to the waveguide. This interference effect can be modulated by the graphene layer via the modulation of its chemical potential. We conclude that these hybrid waveguide based devices act similarly to a Mach-Zehnder interferometer with one arm being the THz signal above the waveguide and the other arm being the THz signal propagating through the waveguide. The demonstration of such functionality is novel and opens very promising perspectives for THz interferometry and THz modulation.

As a perspective, we will use a Si lens to improve the coupling of the incident THz pulses with the hybrid waveguides. We expect that the optimization of the coupling will reduce the interference effect and promote large modulation efficiency of the incident THz waves over the full spectral bandwidth of the hybrid waveguides. Such measurements will allow us to optimize the design of the waveguides for achieving performances comparable to the state of the art. We will also extend this architecture to other 2D materials and investigate the properties of the propagating modes.

Appendix A

Appendix

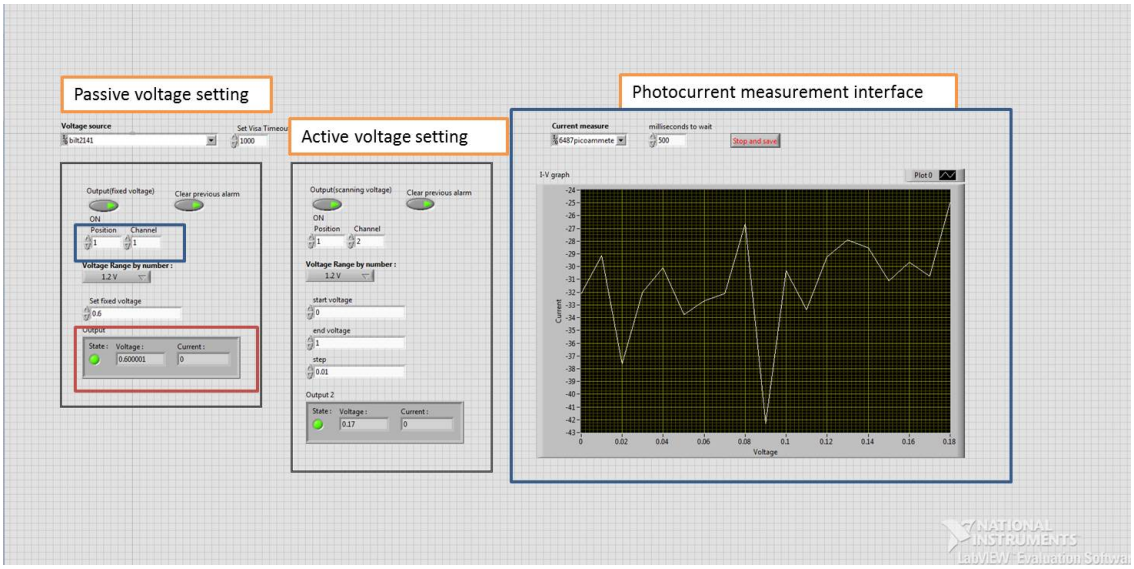

Fig. A.1 *V_{GATE} and V_{DS} are controlled by two channels on the panel. The active voltage channel follows a programmed loop, it can be either V_{GATE} or V_{DS}, the passive voltage channel is either a fixed voltage or an dependent variable of active voltage.*

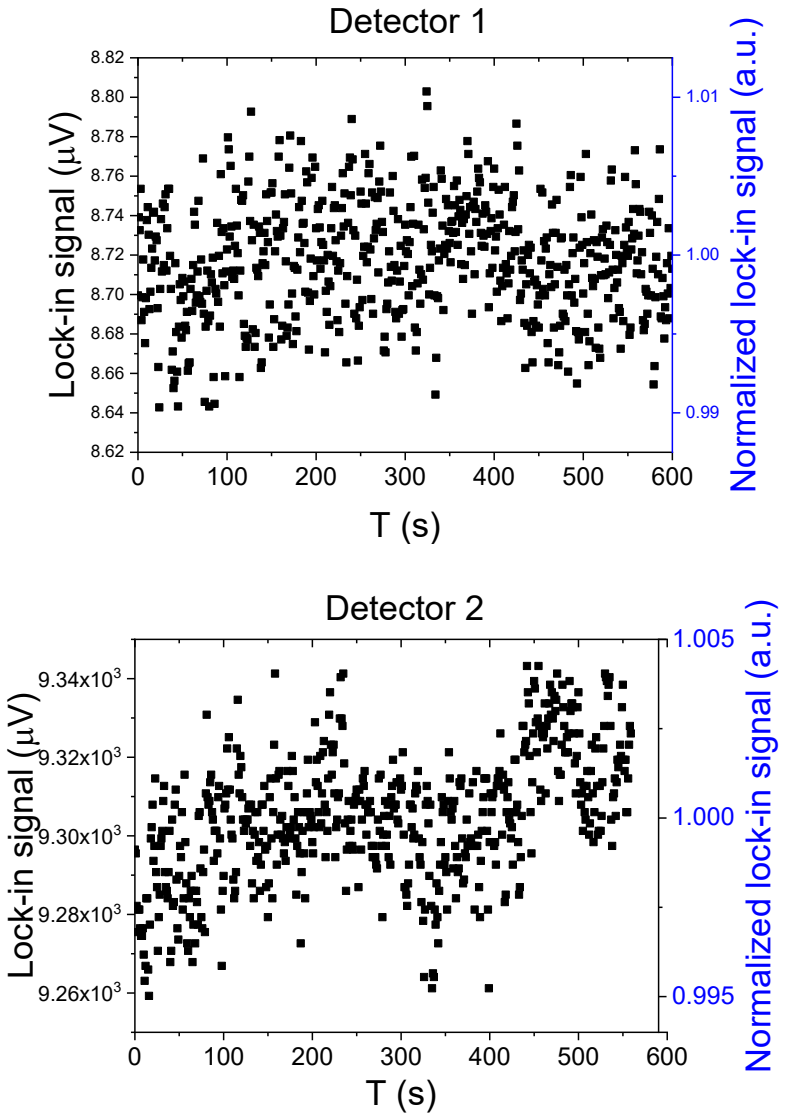

Fig. A.2 *In photocurrent measurement, the unstability of laser power needs to be less than 0.5% in 500 s, here is a 500 s stability test for two detectors at a fixed laser power.*

Appendix B

Fabrication of waveguide samples

Let me introduce the fabrication process of the waveguide samples. We start from the design of mask for waveguides with different dimensions. There two optional width for the waveguide that are 400 µm and 600 µm. For the length, there are three options that are 2 mm 2.5 mm, and 3 mm. The layout of ridges is illustrated in Figure B.1. Then, we

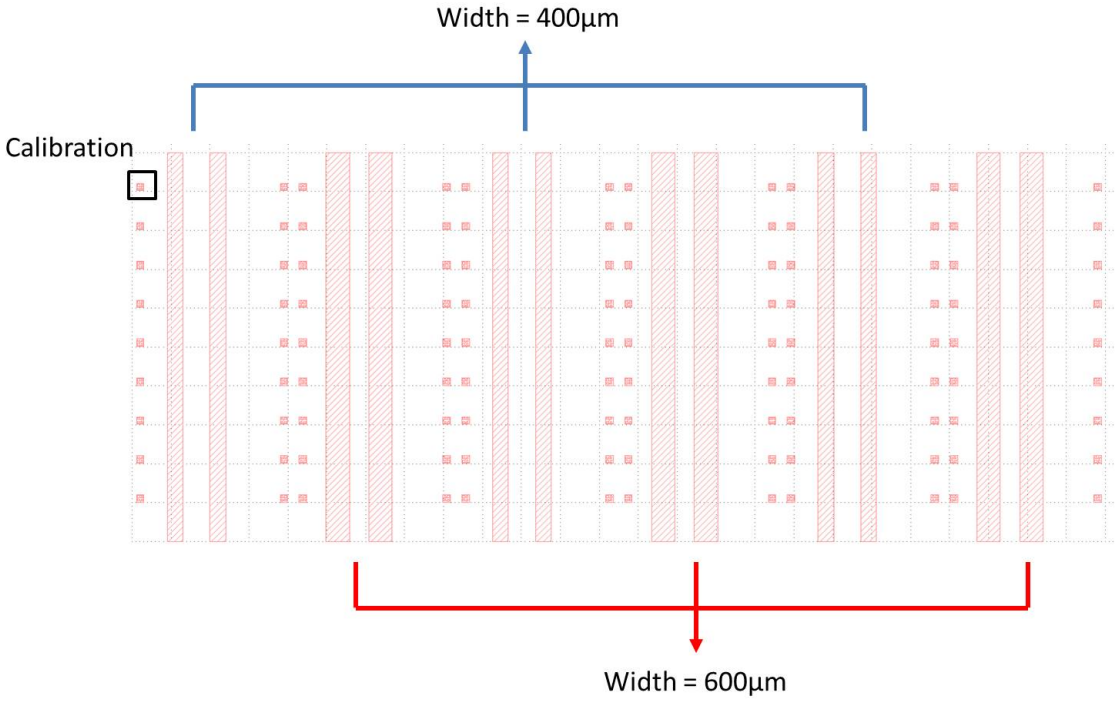

Fig. B.1 *Photomask of waveguides for optical lithography*

start to fabricate the sample by the following steps:

- Wafer bonding A 900 nm-thick layer of Au is deposited via thermal evaporation on top of the MBE-grown heterostructure and on a substrate of lightly doped

GaAs.These two structures are then surface-mounted with the gold layers in contact, and with the crystallographic axes aligned. By using *thermocompression bonding* technique, the sandwich structure sample is wafer-bonded. Then, we remove the GaAs substrate material underneath the waveguide active region grown via MBE by using a combination of mechanical and chemical processes.

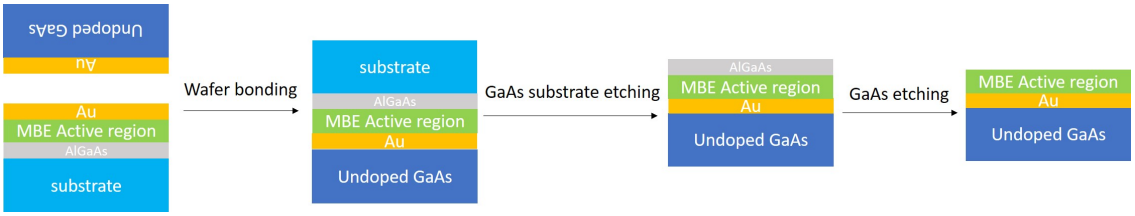

Fig. B.2 *A schematic workflow of wafer bonding.*

- WG definition and gate dielectric deposition With the layout defined by photomask design, the geometry of waveguide is realized by optical lithography[179, 180]. These ridges on the wafer are perpendicular to the major crystal axis. Then we use active material etching to remove those unnecessary parts[181]. After that, a 60 nm-thick HfO_2 is deposited on top of the ridges via atomic layer deposition(ALD) at T = 573 K

- Source and Drain top-metal contacts The layout of electrodes is realized by photomask reported in Figure B.3, then the top metallic contacts are grwon by metal deposition and liftoff process.

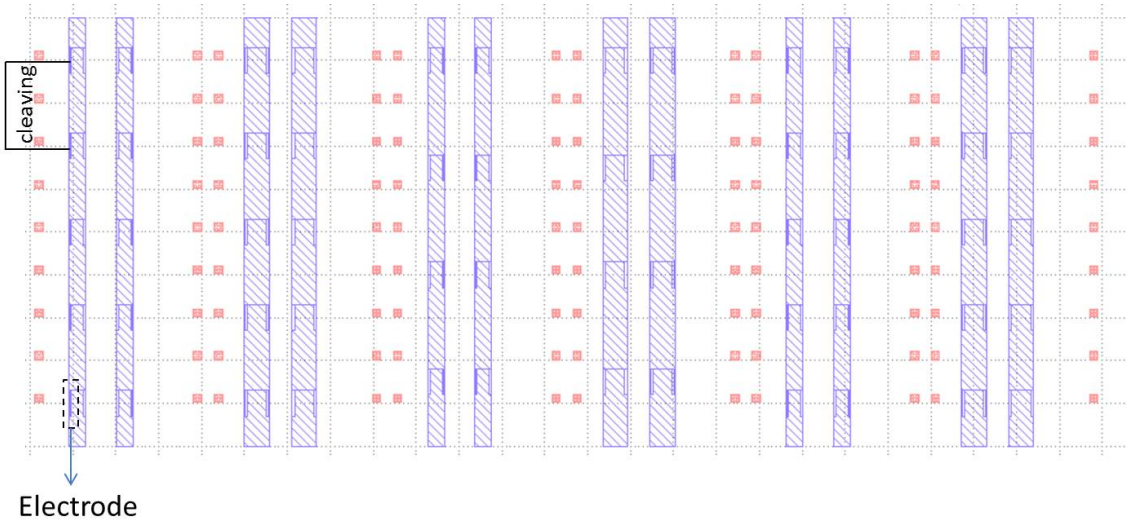

Fig. B.3 *Photomask of top metallic contacts for optical lithography*

- Graphene transfer and removal The transfer of the single layer graphene[182] is via standard wet transfer method [183]. First, the whole area of sample is covered with the graphene, the ridges with better coverage of the graphene are kept and masked. The graphene above other ridges then are chemically removed via O_2 plasma etching to be the bare waveguides.

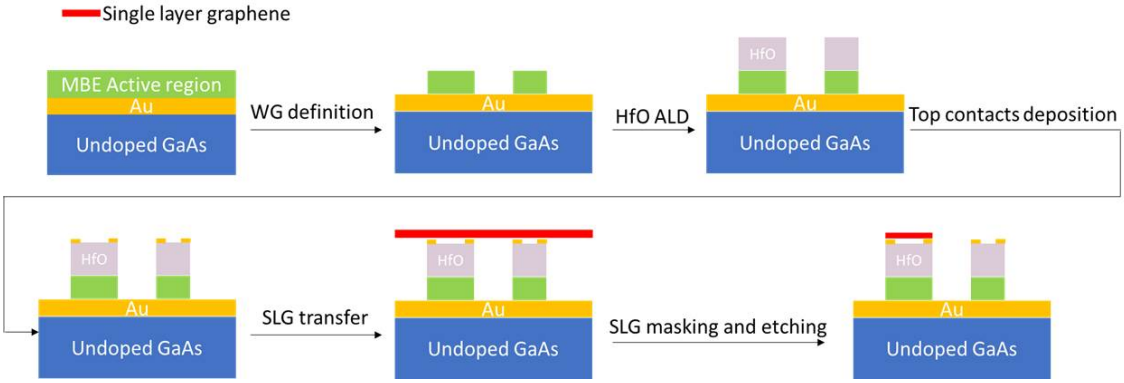

Fig. B.4 *A schematic workflow of waveguide definition including geometrical definition and the graphene layer transfer and removal.*

- Waveguids cleaving and wire bonding The waveguides are cleaved manually to three different lengths: 2.0 mm 2.5 mm, and 3.0 mm. Then a pair of waveguides composed of graphene-covered one and bare one are well packed onto a U-shaped copper holder via Indium soldering. The final step is to build electrical connection between the top contacts and the corresponding ceramic-metal pads by using wedge-bonding technique.

B.1 The strategy uesd in mapping Raman spectroscopy

We use two different strategies for investigating the coverage of graphene sheet and the eastimation of leaked graphene shown in Table B.1.

Graphene Coverage	
Wavelength	532 nm
Power ratio(Full Power@70mW)	1%
Exposure time	1 s
Step($X \times Y$)	10 µm × 2 µm
Objective	20 ×
Leakage Estimation	
Wavelength	532 nm
Power ratio(Full Power@70mW)	5%
Exposure time	2 s
Step($X \times Y$)	2 µm × 2 µm
Objective	50 ×

Table B.1: Parameters for Graphene coverage investigation and leakage estimation respetively

Bibliography

[1] H. Rubens & O. von Baeyer; " LXXX. On extremely long waves, emitted by the quartz mercury lamp "; The London, Edinburgh, and Dublin Philosophical Magazine and Journal of Science **21**, pp. 689–695 (1911). ISSN 1941-5982. 1

[2] A. Markelz, S. Whitmire, J. Hillebrecht & R. Birge; "THz time domain spectroscopy of biomolecular conformational modes"; Physics in Medicine and Biology **47**, pp. 3797–3805 (2002). ISSN 00319155. 1

[3] D. Saeedkia; *Handbook of Terahertz Technology for Imaging, Sensing and Communications* (Elsevier) (2013); ISBN 9780857096494. 1

[4] S. S. Dhillon, M. S. Vitiello, E. H. Linfield, A. G. Davies, M. C. Hoffmann, J. Booske, C. Paoloni, M. Gensch, P. Weightman, G. P. Williams, E. Castro-Camus, D. R. Cumming, F. Simoens, I. Escorcia-Carranza, J. Grant, S. Lucyszyn, M. Kuwata-Gonokami, K. Konishi, M. Koch, C. A. Schmuttenmaer, T. L. Cocker, R. Huber, A. G. Markelz, Z. D. Taylor, V. P. Wallace, J. Axel Zeitler, J. Sibik, T. M. Korter, B. Ellison, S. Rea, P. Goldsmith, K. B. Cooper, R. Appleby, D. Pardo, P. G. Huggard, V. Krozer, H. Shams, M. Fice, C. Renaud, A. Seeds, A. Stöhr, M. Naftaly, N. Ridler, R. Clarke, J. E. Cunningham & M. B. Johnston; "The 2017 terahertz science and technology roadmap"; Journal of Physics D: Applied Physics **50**, p. 043001 (2017). ISSN 13616463. 2

[5] Y. K. Zhu, G. Y. Tian, R. S. Lu & H. Zhang; "A review of optical NDT technologies"; Sensors **11**, pp. 7773–7798 (2011). ISSN 14248220. 2

[6] E. Abraham, A. Younus, J. C. Delagnes & P. Mounaix; "Non-invasive investigation of art paintings by terahertz imaging"; Applied Physics A **100**, pp. 585–590 (2010). ISSN 14320630. 2

[7] C. Yu, S. Fan, Y. Sun & E. Pickwell-Macpherson; "The potential of terahertz imaging for cancer diagnosis: A review of investigations to date." Quantitative imaging in medicine and surgery **2**, pp. 33–45 (2012). ISSN 2223-4292. 2, 3

[8] S. Koenig, D. Lopez-Diaz, J. Antes, F. Boes, R. Henneberger, A. Leuther, A. Tessmann, R. Schmogrow, D. Hillerkuss, R. Palmer, T. Zwick, C. Koos, W. Freude, O. Ambacher, J. Leuthold & I. Kallfass; "Wireless sub-THz communication system with high data rate"; Nature Photonics **7**, pp. 977–981 (2013). ISSN 17494885. 3, 57

[9] R. A. Lewis; "A review of terahertz sources"; Journal of Physics D: Applied Physics **47**, p. 374001 (2014). ISSN 13616463. 3, 6

[10] G. Chattopadhyay; "Technology, capabilities, and performance of low power terahertz sources"; IEEE Transactions on Terahertz Science and Technology **1**, pp. 33–53 (2011). ISSN 2156342X. 3

[11] M. Tacke; "Lead–salt lasers"; Philosophical Transactions of the Royal Society of London A: Mathematical, Physical and Engineering Sciences **359**, pp. 547–566 (2001). 3

[12] B. Scherger, C. Jördens & M. Koch; "Variable-focus terahertz lens"; Optics Express **19**, pp. 4528–4535 (2011). ISSN 1094-4087. 4

[13] J. S. Li; "Tunable focus graphene-based terahertz lens"; Optics Communications **359**, pp. 268–271 (2016). ISSN 00304018. http://dx.doi.org/10.1016/j.optcom.2015.09.105. 4

[14] J. Federici & L. Moeller; "Review of terahertz and subterahertz wireless communications"; Journal of Applied Physics **107**, p. 6 (2010). ISSN 00218979. 4

[15] M. Rahm, J. S. Li & W. J. Padilla; "THz wave modulators: A brief review on different modulation techniques"; Journal of Infrared, Millimeter, and Terahertz Waves **34**, pp. 1–27 (2013). ISSN 18666892. 4

[16] M. Y. Glyavin, G. G. Denisov, V. E. Zapevalov, A. N. Kuftin, A. G. Luchinin, V. N. Manuilov, M. V. Morozkin, A. S. Sedov & A. V. Chirkov; "Terahertz gyrotrons: State of the art and prospects"; Journal of Communications Technology and Electronics **59**, pp. 792–797 (2014). ISSN 10642269. 5

[17] K. H. Jang, S. G. Jeon, J. I. Kim, J. H. Won, J. K. So, S. H. Bak, A. Srivastava, S. S. Jung & G. S. Park; "High order mode oscillation in a terahertz photonic-band-gap multibeam reflex klystron"; Applied Physics Letters **93**, pp. 7–10 (2008). ISSN 00036951. 5

[18] J. M. Byrd, W. P. Leemans, A. Loftsdottir, B. Marcelis, M. C. Martin, W. R. McKinney, F. Sannibale, T. Scarvie & C. Steier; "Observation of Broadband Self-Amplified Spontaneous Coherent Terahertz Synchrotron Radiation in a Storage Ring"; Physical Review Letters **89**, pp. 1–4 (2002). ISSN 10797114. 5

[19] M. Y. Glyavin & A. G. Luchinin; "Powerful terahertz gyrotrons based on pulsed magnets"; Terahertz Science and Technology **2**, pp. 150–155 (2009). 5

[20] M. Y. Glyavin, A. G. Luchinin, G. S. Nusinovich, J. Rodgers, D. G. Kashyn, C. A. Romero-Talamas & R. Pu; "A 670 GHz gyrotron with record power and efficiency"; Applied Physics Letters **101**, p. 153503 (2012). ISSN 00036951. 5

[21] A. Fokin, M. Glyavin, G. Golubiatnikov, L. Lubyako, M. Morozkin, B. Movschevich, A. Tsvetkov & G. Denisov; "High-power sub-terahertz source with a record frequency stability at up to 1 Hz"; Scientific Reports **8**, pp. 1–6 (2018). ISSN 20452322. http://dx.doi.org/10.1038/s41598-018-22772-1. 5

[22] R. Li, C. Ruan, A. K. Fahad, C. Zhang & S. Li; "Broadband and high-power terahertz radiation source based on extended interaction klystron"; Scientific Reports **9**, pp. 3–10 (2019). ISSN 20452322. http://dx.doi.org/10.1038/s41598-019-41087-3. 6

[23] K.-i. Shudo, I. Katayama & S.-y. Ohno; *Frontier in Optical Methods: Nano-Characterization and Coherent Control*; volume 180 (Springer-Verlag Berlin An) (2014); ISBN 9783642536946; arXiv:1011.1669v3. 6

[24] J. Lusakowski, W. Knap, N. Dyakonova, L. Varani, J. Mateos, T. Gonzalez, Y. Roelens, S. Bollaert, A. Cappy & K. Karpierz; "Voltage tuneable terahertz emission from a ballistic nanometer InGaAsInAlAs transistor"; Journal of Applied Physics **97**, p. 064307 (2005). ISSN 00218979. 6

[25] L. Ozyuzer, A. E. Koshelev, C. Kurter, N. Gopalsami, Q. Li, M. Tachiki, K. Kadowaki, T. Yamamoto, H. Minami, H. Yamaguchi, T. Tachiki, K. E. Gray, W. K. Kwok & U. Welp; "Emission of coherent THz radiation from superconductors"; Science **318**, pp. 1291–1293 (2007). ISSN 00368075. 6

[26] O. A. Shevchenko, N. A. Vinokurov, V. S. Arbuzov, K. N. Chernov, I. V. Davidyuk, O. I. Deichuly, E. N. Dementyev, B. A. Dovzhenko, Y. V. Getmanov, Y. I. Gorbachev, B. A. Knyazev, E. I. Kolobanov, A. A. Kondakov, V. R. Kozak, E. V. Kozyrev, S. A. Krutikhin, V. V. Kubarev, G. N. Kulipanov, E. A. Kuper, I. V. Kuptsov, G. Y. Kurkin, L. E. Medvedev, S. V. Motygin, V. K. Ovchar, V. N. Osipov, V. M. Petrov, A. M. Pilan, V. M.

Popik, V. V. Repkov, T. V. Salikova, M. A. Scheglov, I. K. Sedlyarov, S. S. Serednyakov, A. N. Skrinsky, S. V. Tararyshkin, A. G. Tribendis, V. G. Tcheskidov, P. D. Vobly & V. N. Volkov; "The Novosibirsk Free-Electron Laser Facility"; Bulletin of the Russian Academy of Sciences: Physics **83**, pp. 228–231 (2019). ISSN 19349432. 6

[27] G. Dodel; "On the history of far-infrared (FIR) gas lasers: Thirty-five years of research and application"; Infrared Physics and Technology **40**, pp. 127–139 (1999). ISSN 13504495. 6

[28] A. Pagies, G. Ducournau & J. F. Lampin; "Low-threshold terahertz molecular laser optically pumped by a quantum cascade laser"; APL Photonics **1**, p. 031302 (2016). ISSN 23780967. http://dx.doi.org/10.1063/1.4945355. 6

[29] P. Chevalier, A. Amirzhan, F. Wang, M. Piccardo, S. G. Johnson, F. Capasso & H. O. Everitt; "Widely tunable compact terahertz gas lasers"; Science **366**, pp. 856–860 (2019). ISSN 10959203. 6

[30] M. Mičica, S. Eliet, M. Vanwolleghem, R. Motiyenko, A. Pienkina, L. Margulès, K. Postava, J. Pištora & J.-F. Lampin; "High-resolution THz gain measurements in optically pumped ammonia"; Optics Express **26**, pp. 21242–21248 (2018). ISSN 1094-4087. 6

[31] B. S. Williams; *Terahertz quantum cascade lasers*; Ph.D. thesis; Massachusetts Institute of Technology (2003). 7

[32] M. S. Vitiello, G. Scalari, B. Williams & P. De Natale; "Quantum cascade lasers: 20 years of challenges"; Optics Express **23**, pp. 5167–5182 (2015). ISSN 1094-4087. 7

[33] M. Ravaro, C. Manquest, C. Sirtori, S. Barbieri, G. Santarelli, K. Blary, J.-F. Lampin, S. P. Khanna & E. H. Linfield; "Phase-locking of a 25 THz quantum cascade laser to a frequency comb using a GaAs photomixer"; Optics Letters **36**, pp. 3969–3971 (2011). ISSN 0146-9592. 7

[34] H. W. Hübers, S. G. Pavlov & V. N. Shastin; "Terahertz lasers based on germanium and silicon"; Semiconductor Science and Technology **20**, p. S211 (2005). ISSN 02681242. 7

[35] M. A. Odnoblyudov, A. A. Prokofiev, I. N. Yassievich & K. A. Chao; "Theory of a strained p-Ge resonant-state terahertz laser"; Physical Review B **70**, pp. 1–14 (2004). ISSN 01631829. 7

[36] A. Rice, Y. Jin, X. F. Ma, X. C. Zhang, D. Bliss, J. Larkin & M. Alexander; "Terahertz optical rectification from <110> zinc-blende crystals"; Applied Physics Letters **64**, pp. 1324–1326 (1994). ISSN 00036951. 7

[37] S. L. Chuang, S. Schmitt-Rink, B. I. Greene, P. N. Saeta & A. F. Levi; "Optical rectification at semiconductor surfaces"; Physical Review Letters **68**, pp. 102–105 (1992). ISSN 00319007. 7

[38] K. A. McIntosh, E. R. Brown, K. B. Nichols, O. B. McMahon, W. F. DiNatale & T. M. Lyszczarz; "Terahertz photomixing with diode lasers in low-temperature-grown GaAs"; Applied Physics Letters **67**, pp. 3844–3846 (1995). ISSN 00036951. 7

[39] T. Kampfrath, M. Battiato, P. Maldonado, G. Eilers, J. Nötzold, S. Mährlein, V. Zbarsky, F. Freimuth, Y. Mokrousov, S. Blügel, M. Wolf, I. Radu, P. M. Oppeneer & M. Münzenberg; "Terahertz spin current pulses controlled by magnetic heterostructures"; Nature Nanotechnology **8**, pp. 256–260 (2013). ISSN 17483395. 7

[40] E. Beaurepaire, G. M. Turner, S. M. Harrel, M. C. Beard, J. Y. Bigot & C. A. Schmuttenmaer; "Coherent terahertz emission from ferromagnetic films excited by femtosecond laser pulses"; Applied Physics Letters **84**, pp. 3465–3467 (2004). ISSN 00036951. 7

[41] J. Maysonnave, S. Huppert, F. Wang, S. Maero, C. Berger, W. De Heer, T. B. Norris, L. A. De Vaulchier, S. Dhillon, J. Tignon, R. Ferreira & J. Mangeney; "Terahertz generation by dynamical photon drag effect in graphene excited by femtosecond optical pulses"; Nano Letters **14**, pp. 5797–5802 (2014). ISSN 15306992. 7, 8

[42] D. Sun, C. Divin, J. Rioux, J. E. Sipe, C. Berger, W. A. De Heer, P. N. First & T. B. Norris; "Coherent control of ballistic photocurrents in multilayer epitaxial graphene using quantum interference"; Nano Letters **10**, pp. 1293–1296 (2010). ISSN 15306984. 7

[43] J. Ajayan, D. Nirmal, T. Ravichandran, P. Mohankumar, P. Prajoon, L. Arivazhagan & C. K. Sarkar; "InP high electron mobility transistors for submillimetre wave and terahertz frequency applications: A review"; AEU - International Journal of Electronics and Communications **94**, pp. 199–214 (2018). ISSN 16180399. 8, 9

[44] M. A. Basten, J. C. Tucek, D. A. Gallagher, K. E. Kreischer & R. Mihailovich; "A 0.85 THz vacuum-based power amplifier"; in "2012 IEEE 13th International Vacuum Electronics Conference, IVEC 2012," pp. 39–40 (2012); ISBN 9781467301879. 8, 9

[45] C. Mauro, R. P. Green, A. Tredicucci, F. Beltram, H. E. Beere & D. A. Ritchie; "Amplification of terahertz radiation in quantum cascade structures"; Journal of Applied Physics **102**, pp. 1–4 (2007). ISSN 00218979. 8, 9, 10

[46] Y. Ren, R. Wallis, Y. D. Shah, D. S. Jessop, R. Degl'Innocenti, A. Klimont, V. Kamboj, H. E. Beere & D. A. Ritchie; "Single mode terahertz quantum cascade amplifier"; Applied Physics Letters **105**, pp. 1–5 (2014). ISSN 00036951. 8, 9, 10

[47] H. Zhu, H. Zhu, F. Wang, G. Chang, C. Yu, Q. Yan, J. Chen, L. Li, A. G. Davies, E. H. Linfield, Z. Tang, P. Chen, W. Lu, G. Xu & L. He; "Terahertz master-oscillator power-amplifier quantum cascade laser with a grating coupler of extremely low reflectivity"; Optics Express **26**, pp. 1942–1953 (2018). ISSN 1094-4087. 8

[48] L. A. Samoska; "An overview of solid-state integrated circuit amplifiers in the submillimeter-wave and THz regime"; IEEE Transactions on Terahertz Science and Technology **1**, pp. 9–24 (2011). ISSN 2156342X. 8

[49] D. Schwantuschke, P. Brückner, S. Wagner, M. Dammann, M. Mikulla & R. Quay; "Enhanced GaN HEMT technology for E-band power amplifier MMICs with 1W output power"; in "Asia-Pacific Microwave Conference Proceedings, APMC," pp. 395–398 (2017); ISBN 9781538606407. 9

[50] M. Urteaga, Z. Griffith, M. Seo, J. Hacker & M. J. Rodwell; "InP HBT Technologies for THz Integrated Circuits"; Proceedings of the IEEE **105**, pp. 1051–1067 (2017). ISSN 15582256. 9

[51] R. Degl'Innocenti, S. J. Kindness, H. E. Beere & D. A. Ritchie; "All-integrated terahertz modulators"; Nanophotonics **7**, pp. 127–144 (2018). ISSN 21928614. 9

[52] Z. Xie, X. Wang, J. Ye, S. Feng, W. Sun, T. Akalin & Y. Zhang; "Spatial terahertz modulator"; Scientific Reports **3**, pp. 1–4 (2013). ISSN 20452322. 9, 10

[53] P. Weis, J. L. Garcia-Pomar, M. Höh, B. Reinhard, A. Brodyanski & M. Rahm; "Spectrally wide-band terahertz wave modulator based on optically tuned graphene"; ACS Nano **6**, pp. 9118–9124 (2012). ISSN 19360851. 9, 10

[54] T. Okada & K. Tanaka; "Photo-designed terahertz devices"; Scientific Reports **1**, p. 121 (2011). ISSN 20452322. 9

[55] B. Zhang, T. He, J. Shen, Y. Hou, Y. Hu, M. Zang, T. Chen, S. Feng, F. Teng & L. Qin; "Conjugated polymer-based broadband terahertz wave modulator"; Optics Letters **39**, pp. 6110–6113 (2014). ISSN 0146-9592. 9, 10

[56] Y. Cao, S. Gan, Z. Geng, J. Liu, Y. Yang, Q. Bao & H. Chen; "Optically tuned terahertz modulator based on annealed multilayer MoS2"; Scientific Reports **6**, p. 22899 (2016). ISSN 20452322. 10, 72

[57] Q. Y. Wen, W. Tian, Q. Mao, Z. Chen, W. W. Liu, Q. H. Yang, M. Sanderson & H. W. Zhang; "Graphene based all-optical spatial terahertz modulator"; Scientific Reports **4**, pp. 2–6 (2014). ISSN 20452322. 10

[58] W. J. Padilla, A. J. Taylor, C. Highstrete, M. Lee & R. D. Averitt; "Dynamical electric and magnetic metamaterial response at terahertz frequencies"; Physical Review Letters **96**, pp. 1–4 (2006). ISSN 00319007. 10

[59] H. T. Chen, J. F. O'Hara, A. K. Azad, A. J. Taylor, R. D. Averitt, D. B. Shrekenhamer & W. J. Padilla; "Experimental demonstration of frequency-agile terahertz metamaterials"; Nature Photonics **2**, pp. 295–298 (2008). ISSN 17494885. 10

[60] T. Kleine-Ostmann, P. Dawson, K. Pierz, G. Hein & M. Koch; "Room-temperature operation of an electrically driven terahertz modulator"; Applied Physics Letters **84**, pp. 3555–3557 (2004). ISSN 00036951. 10

[61] H. T. Chen, W. J. Padilla, J. M. Zide, A. C. Gossard, A. J. Taylor & R. D. Averitt; "Active terahertz metamaterial devices"; Nature **444**, pp. 597–600 (2006). ISSN 14764687. 11

[62] A. Markov, H. Guerboukha & M. Skorobogatiy; "Hybrid metal wire–dielectric terahertz waveguides: challenges and opportunities [Invited]"; Journal of the Optical Society of America B **31**, pp. 2587–2600 (2014). ISSN 0740-3224. 11

[63] S. Atakaramians, S. Afshar V., T. M. Monro & D. Abbott; "Terahertz dielectric waveguides"; Advances in Optics and Photonics **5**, pp. 169–215 (2013). ISSN 1943-8206. 11

[64] M. Mittendorff, S. Li & T. E. Murphy; "Graphene-Based Waveguide-Integrated Terahertz Modulator"; ACS Photonics **4**, pp. 316–321 (2017). ISSN 23304022. 11, 59

[65] H. Li, S. Atakaramians, R. Lwin, X. Tang, Z. Yu, A. Argyros & B. T. Kuhlmey; "Flexible single-mode hollow-core terahertz fiber with metamaterial cladding"; Optica **3**, pp. 941–947 (2016). ISSN 2334-2536. 11

[66] R. W. McGowan, G. Gallot & D. Grischkowsky; "Propagation of ultrawideband short pulses of terahertz radiation through submillimeter-diameter circular waveguides"; Optics Letters **24**, pp. 1431–1433 (1999). ISSN 0146-9592. 11

[67] R. Mendis & D. Grischkowsky; "Undistorted guided-wave propagation of subpicosecond terahertz pulses"; Optics Letters **26**, pp. 846–848 (2001). ISSN 0146-9592. 11

[68] R. Mendis & D. M. Mittleman; "Comparison of the lowest-order transverse-electric (TE_1) and transverse-magnetic (TEM) modes of the parallel-plate waveguide for terahertz pulse applications"; Optics Express **17**, pp. 14839–14850 (2009). ISSN 1094-4087. 11

[69] R. Mendis & D. M. Mittleman; "An investigation of the lowest-order transverse-electric (TE_1) mode of the parallel-plate waveguide for THz pulse propagation"; Journal of the Optical Society of America B **26**, pp. A6–A13 (2009). ISSN 0740-3224. 11

[70] K. Wang & D. M. Mittleman; "Metal wires for terahertz wave guiding"; Nature **432**, pp. 376–379 (2004). ISSN 00280836. 11

[71] M. J. King & J. C. Wiltse; "Surface-Wave Propagation on Coated or Uncoated Metal Wires at Millimeter Wavelengths"; IRE Transactions on Antennas and Propagation **10**, pp. 246–254 (1962). ISSN 00961973. 11

[72] M. Wächter, M. Nagel & H. Kurz; "Metallic slit waveguide for dispersion-free low-loss terahertz signal transmission"; Applied Physics Letters **90**, pp. 1–4 (2007). ISSN 00036951. 11

[73] F. Benabid, P. J. Roberts, F. Couny & P. S. Light; "Light and gas confinement in hollow-core photonic crystal fibre based photonic microcells"; Journal of the European Optical Society **4**, pp. 1–9 (2009). ISSN 19902573. 11

[74] K. J. Rowland, P. T. M. Monro & S. A. Vahid; *Guiding Light in Low-Index Media via Multilayer Waveguides by*; Doctoral dissertation; The university of Adelaide (2010). 11

[75] A. Argyros & J. Pla; "Hollow-core polymer fibres with a kagome lattice: potential for transmission in the infrared"; Optics Express **15**, pp. 7713–7719 (2007). ISSN 1094-4087. 11

[76] F. Couny, P. J. Roberts, T. A. Birks & F. Benabid; "Square-lattice large-pitch hollow-core photonic crystal fiber"; Opt. Express **16**, pp. 20626–20636 (2008). http://www.opticsexpress.org/abstract.cfm?URI=oe-16-25-20626. 11

[77] A. Argyros, S. G. Leon-Saval, J. Pla & A. Docherty; "Antiresonant reflection and inhibited coupling in hollow-core square lattice optical fibres"; Optics Express **16**, pp. 5642–5648 (2008). ISSN 1094-4087. 11

[78] M. Nagel, A. Marchewka & H. Kurz; "Low-index discontinuity terahertz waveguides"; Optics Express **14**, pp. 9944–9954 (2006). ISSN 1094-4087. 11

[79] A. Hassani, A. Dupuis & M. Skorobogatiy; "Low loss porous terahertz fibers containing multiple subwavelength holes"; Applied Physics Letters **92**, pp. 90–93 (2008). ISSN 00036951. 11

[80] A. Hassani, A. Dupuis & M. Skorobogatiy; "Porous polymer fibers for low-loss Terahertz guiding"; Optics Express **16**, pp. 6340–6351 (2008). ISSN 1094-4087. 11

[81] S. Atakaramians, S. Afshar V., B. M. Fischer, D. Abbott & T. M. Monro; "Porous fibers: a novel approach to low loss THz waveguides"; Optics Express **16**, p. 8845 (2008). ISSN 1094-4087. 11

[82] P. R. Wallace; "The band theory of graphite"; Physical Review **71**, pp. 622–634 (1947). ISSN 0031899X. 12

[83] H. P. Boehm, R. Setton & E. Stumpp; "Nomenclature and terminology of graphite intercalation compounds"; Pure and Applied Chemistry **66**, pp. 1893–1901 (1994). ISSN 13653075. 12

[84] A. H. Castro Neto, F. Guinea, N. M. Peres, K. S. Novoselov & A. K. Geim; "The electronic properties of graphene"; Reviews of Modern Physics **81**, pp. 109–162 (2009). ISSN 00346861; 0709.1163. 13

[85] S. Massabeau, M. Baillergeau, T. Phuphachong, C. Berger, W. A. De Heer, S. Dhillon, J. Tignon, L. A. De Vaulchier, R. Ferreira & J. Mangeney; "Evidence of Fermi level pinning at the Dirac point in epitaxial multilayer graphene"; Physical Review B **95**, p. 85311 (2017). ISSN 24699969. 14, 73

[86] I. Gierz, M. Mitrano, J. C. Petersen, C. Cacho, I. C. Turcu, E. Springate, A. Stöhr, A. Köhler, U. Starke & A. Cavalleri; "Population inversion in monolayer and bilayer graphene"; Journal of Physics Condensed Matter **27**, p. 164204 (2015). ISSN 1361648X; 1409.0211. 14, 57

[87] O. A. Azar, M. Abdi & H. Baghban; "Graphene-Based Terahertz Waveguide Amplifier"; Procedia Materials Science **11**, pp. 270–274 (2015). ISSN 22118128. 14

[88] T. Guo, L. Zhu, P.-Y. Chen & C. Argyropoulos; "Tunable terahertz amplification based on photoexcited active graphene hyperbolic metamaterials [Invited]"; Optical Materials Express **8**, pp. 3941–3952 (2018). ISSN 2159-3930. 14

[89] P. A. George, J. Strait, J. Dawlaty, S. Shivaraman, M. Chandrashekhar, F. Rana & M. G. Spencer; "Ultrafast Optical-Pump Terahertz-Probe Spectroscopy of the Carrier Relaxation and Recombination Dynamics in Epitaxial Graphene"; Nano Letters **8**, pp. 4248–4251 (2008). ISSN 1530-6984. https://pubs.acs.org/doi/10.1021/nl8019399http://arxiv.org/abs/0805.4647http://dx.doi.org/10.1021/nl8019399; 0805.4647. 14

[90] V. V. Popov, O. V. Polischuk, A. R. Davoyan, V. Ryzhii, T. Otsuji & M. S. Shur; "Plasmonic terahertz lasing in an array of graphene nanocavities"; Physical Review B **86**, pp. 1–6 (2012). ISSN 10980121. 14

[91] Y. Takatsuka, K. Takahagi, E. Sano, V. Ryzhii & T. Otsuji; "Gain enhancement in graphene terahertz amplifiers with resonant structures"; Journal of Applied Physics **112**, pp. 3–7 (2012). ISSN 00218979. 14

[92] O. V. Polischuk, D. V. Fateev, T. Otsuji & V. V. Popov; "Plasmonic amplification of terahertz radiation in a periodic graphene structure with the carrier injection"; Applied Physics Letters **111**, p. 081110 (2017). ISSN 00036951. 14

[93] O. V. Polischuk, D. V. Fateev & V. V. Popov; "Electrical Tunability of Terahertz Amplification in a Periodic Plasmon Graphene Structure with Charge-Carrier Injection"; Semiconductors **52**, pp. 1534–1539 (2018). ISSN 10637826. 14

[94] I. Nefedov & L. Melnikov; "Plasmonic terahertz amplification in graphene-based asymmetric hyperbolic metamaterial"; Photonics **2**, pp. 594–603 (2015). ISSN 23046732. 14

[95] M. Chen, F. Fan, L. Yang, X. Wang & S. J. Chang; "Tunable Terahertz Amplifier Based on Slow Light Edge Mode in Graphene Plasmonic Crystal"; IEEE Journal of Quantum Electronics **53**, pp. 1–6 (2017). ISSN 00189197. 14

[96] T. Watanabe, T. Fukushima, Y. Yabe, S. A. Boubanga Tombet, A. Satou, A. A. Dubinov, V. Y. Aleshkin, V. Mitin, V. Ryzhii & T. Otsuji; "The gain enhancement effect of surface plasmon polaritons on terahertz stimulated emission in optically pumped monolayer graphene"; New Journal of Physics **15**, p. 075003 (2013). ISSN 13672630. 14

[97] P. Huang, E. Riccardi, S. Messelot, H. Graef, F. Valmorra, J. Tignon, T. Taniguchi, K. Watanabe, S. Dhillon, B. Plaçais, R. Ferreira & J. Mangeney; "Ultra-long carrier lifetime in neutral graphene-hBN van der Waals heterostructures under mid-infrared illumination"; Nature Communications **11**, pp. 1–9 (2020). ISSN 20411723. http://dx.doi.org/10.1038/s41467-020-14714-1. 17, 31

[98] S. Castilla, B. Terrés, M. Autore, L. Viti, J. Li, A. Y. Nikitin, I. Vangelidis, K. Watanabe, T. Taniguchi, E. Lidorikis, M. S. Vitiello, R. Hillenbrand, K. J. Tielrooij & F. H. Koppens; "Fast and Sensitive Terahertz Detection Using an Antenna-Integrated Graphene pn Junction"; Nano Letters **19**, pp. 2765–2773 (2019). ISSN 15306992; 1905.01881. 17

[99] I. Gierz, J. C. Petersen, M. Mitrano, C. Cacho, I. C. Turcu, E. Springate, A. Stöhr, A. Köhler, U. Starke & A. Cavalleri; "Snapshots of non-equilibrium Dirac carrier distributions in graphene"; Nature Materials **12**, pp. 1119–1124 (2013). ISSN 14764660; 1304.1389. 17

[100] F. H. Koppens, T. Mueller, P. Avouris, A. C. Ferrari, M. S. Vitiello & M. Polini; "Photodetectors based on graphene, other two-dimensional materials and hybrid systems"; Nature Nanotechnology **9**, pp. 780–793 (2014). ISSN 17483395. http://dx.doi.org/10.1038/nnano.2014.215. 17, 31, 35

[101] T. Winzer, E. Malić & A. Knorr; "Microscopic mechanism for transient population inversion and optical gain in graphene"; Physical Review B **87**, pp. 1–4 (2013). ISSN 10980121; 1209.4833. 17, 18, 57

[102] L. Viti, D. G. Purdie, A. Lombardo, A. C. Ferrari & M. S. Vitiello; "HBN-Encapsulated, Graphene-based, Room-temperature Terahertz Receivers, with High Speed and Low Noise"; Nano Letters **20**, pp. 3169–3177 (2020). ISSN 1530-6984. 17

[103] L. Banszerus, M. Schmitz, S. Engels, J. Dauber, M. Oellers, F. Haupt, K. Watanabe, T. Taniguchi, B. Beschoten & C. Stampfer; "Ultrahigh-mobility graphene devices from chemical vapor deposition on reusable copper"; Science Advances **1**, pp. 1–7 (2015). ISSN 23752548. 17

[104] R. Jago, T. Winzer, A. Knorr & E. Malic; "Graphene as gain medium for broadband lasers"; Physical Review B - Condensed Matter and Materials Physics **92**, pp. 1–7 (2015). ISSN 1550235X; 1409.8182. 18

[105] A. Satou, V. Ryzhii, Y. Kurita & T. Otsuji; "Threshold of terahertz population inversion and negative dynamic conductivity in graphene under pulse photoexcitation"; Journal of Applied Physics **113**, p. 143108 (2013). ISSN 00218979; 1210.6704. 18

[106] V. Ryzhii, A. A. Dubinov, T. Otsuji, V. Mitin & M. S. Shur; "Terahertz lasers based on optically pumped multiple graphene structures with slot-line and dielectric waveguides"; Journal of Applied Physics **107**, p. 054505 (2010). ISSN 00218979. 18, 59

[107] K. J. Tielrooij, J. C. Song, S. A. Jensen, A. Centeno, A. Pesquera, A. Zurutuza Elorza, M. Bonn, L. S. Levitov & F. H. Koppens; "Photoexcitation cascade and multiple hot-carrier generation in graphene"; Nature Physics **9**, pp. 248–252 (2013). ISSN 17452481. http://dx.doi.org/10.1038/nphys2564. 18, 31

[108] M. T. Mihnev, F. Kadi, C. J. Divin, T. Winzer, S. Lee, C. H. Liu, Z. Zhong, C. Berger, W. A. De Heer, E. Malic, A. Knorr & T. B. Norris; "Microscopic origins of the terahertz carrier relaxation and cooling dynamics in graphene"; Nature Communications **7**, pp. 1–11 (2016). ISSN 20411723. 18

[109] S. Winnerl, F. Göttfert, M. Mittendorff, H. Schneider, M. Helm, T. Winzer, E. Malic, A. Knorr, M. Orlita, M. Potemski, M. Sprinkle, C. Berger & W. A. De Heer; "Time-resolved spectroscopy on epitaxial graphene in the infrared spectral range: Relaxation dynamics and saturation behavior"; Journal of Physics Condensed Matter **25**, p. 054202 (2013). ISSN 09538984. 18, 41

[110] J. H. Strait, H. Wang, S. Shivaraman, V. Shields, M. Spencer & F. Rana; "Very slow cooling dynamics of photoexcited carriers in graphene observed by optical-pump terahertz-probe spectroscopy"; Nano Letters **11**, pp. 4902–4906 (2011). ISSN 15306984; 1108.2746. 18, 41

[111] T. Winzer & E. Malic; "The impact of pump fluence on carrier relaxation dynamics in optically excited graphene"; Journal of Physics Condensed Matter **25**, p. 054201 (2013). ISSN 09538984. 18

[112] K. J. Tielrooij, N. C. Hesp, A. Principi, M. B. Lundeberg, E. A. Pogna, L. Banszerus, Z. Mics, M. Massicotte, P. Schmidt, D. Davydovskaya, D. G. Purdie, I. Goykhman, G. Soavi, A. Lombardo, K. Watanabe, T. Taniguchi, M. Bonn, D. Turchinovich, C. Stampfer, A. C. Ferrari, G. Cerullo, M. Polini & F. H. Koppens; "Out-of-plane heat transfer in van der Waals stacks through electron-hyperbolic phonon coupling"; Nature Nanotechnology **13**, pp. 41–46 (2018). ISSN 17483395; 1702.03766. 19, 48, 54

[113] S. Dai, Q. Ma, M. K. Liu, T. Andersen, Z. Fei, M. D. Goldflam, M. Wagner, K. Watanabe, T. Taniguchi, M. Thiemens, F. Keilmann, G. C. Janssen, S. E. Zhu, P. Jarillo-Herrero, M. M. Fogler & D. N. Basov; "Graphene on hexagonal boron nitride as a tunable hyperbolic metamaterial"; Nature Nanotechnology **10**, pp. 682–686 (2015). ISSN 17483395; 1501.06956. 19

[114] S. Winnerl, M. Orlita, P. Plochocka, P. Kossacki, M. Potemski, T. Winzer, E. Malic, A. Knorr, M. Sprinkle, C. Berger, W. A. De Heer, H. Schneider & M. Helm; "Carrier relaxation in epitaxial graphene photoexcited near the dirac point"; Physical Review Letters **107**, pp. 2–6 (2011). ISSN 00319007. 19

[115] T. Winzer, R. Jago & E. Malic; "Experimentally accessible signatures of Auger scattering in graphene"; Physical Review B **235430**, pp. 1–5 (2016). ISSN 24699969. 19

[116] F. Pizzocchero, L. Gammelgaard, B. S. Jessen, J. M. Caridad, L. Wang, J. Hone, P. Bøggild & T. J. Booth; "The hot pick-up technique for batch assembly of van der Waals heterostructures"; Nature Communications **7**, pp. 1–10 (2016). ISSN 20411723; 1605.02334. 20

[117] L. Wang, I. Meric, P. Y. Huang, Q. Gao, Y. Gao, H. Tran, T. Taniguchi, K. Watanabe, L. M. Campos, D. A. Muller, J. Guo, P. Kim, J. Hone, K. L. Shepard & C. R. Dean; "One-dimensional electrical contact to a two-dimensional material"; Science **342**, pp. 614–617 (2013). ISSN 10959203. 20

[118] K. Mikhail I; "Graphene : carbon in Carbon is one of the most intriguing elements in the Periodic Table ." Materialstoday **10**, pp. 20–27 (2007). ISSN 1369-7021; 0612534. 22

[119] E. B. Sonin; "Effect of Klein tunneling on conductance and shot noise in ballistic graphene"; Physical Review B - Condensed Matter and Materials Physics **79**, pp. 1–10 (2009). ISSN 10980121; 0902.3622. 22

[120] N. Vandecasteele, A. Barreiro, M. Lazzeri, A. Bachtold & F. Mauri; "Current-voltage characteristics of graphene devices: Interplay between Zener-Klein tunneling and defects"; Physical Review B **82**, p. 45416 (2010). ISSN 10980121. https://link.aps.org/doi/10.1103/PhysRevB.82.045416; 1003.2072. 24

[121] W. Yang, S. Berthou, X. Lu, Q. Wilmart, A. Denis, M. Rosticher, T. Taniguchi, K. Watanabe, G. Fève, J. M. Berroir, G. Zhang, C. Voisin,

E. Baudin & B. Plaçais; "A graphene Zener-Klein transistor cooled by a hyperbolic substrate"; Nature Nanotechnology **13**, pp. 47–52 (2018). ISSN 17483395; 1702.02829. 24, 28, 29, 48, 49

[122] G. Kané, M. Lazzeri & F. Mauri; "High-field transport in graphene: The impact of Zener tunneling"; Journal of Physics Condensed Matter **27**, p. 164205 (2015). ISSN 1361648X. 24, 29

[123] J. Martin, N. Akerman, G. Ulbricht, T. Lohmann, J. H. Smet, K. Von Klitzing & A. Yacoby; "Observation of electron-hole puddles in graphene using a scanning single-electron transistor"; Nature Physics **4**, pp. 144–148 (2008). ISSN 17452481. 24

[124] S. Samaddar, I. Yudhistira, S. Adam, H. Courtois & C. B. Winkelmann; "Charge Puddles in Graphene near the Dirac Point"; Physical Review Letters **116**, pp. 1–5 (2016). ISSN 10797114; 1512.05304. 25

[125] S. Adam, E. H. Hwang, V. M. Galitski & S. Das Sarma; "A self-consistent theory for graphene transport"; Proceedings of the National Academy of Sciences of the United States of America **104**, pp. 18392–18397 (2007). ISSN 00278424; 0705.1540. 25

[126] S. Adam, S. Jung, N. N. Klimov, N. B. Zhitenev, J. A. Stroscio & M. D. Stiles; "Mechanism for puddle formation in graphene"; Physical Review B - Condensed Matter and Materials Physics **84**, pp. 1–6 (2011). ISSN 10980121; 1112.1070. 25

[127] H. Zhong, Z. Zhang, H. Xu, C. Qiu & L. M. Peng; "Comparison of mobility extraction methods based on field-effect measurements for graphene"; AIP Advances **5**, p. 057136 (2015). ISSN 21583226. http://dx.doi.org/10.1063/1.4921400. 26

[128] R. Jago, F. Wendler & E. Malic; "Microscopic understanding of the photoconduction effect in graphene"; Physical Review B **96**, pp. 1–7 (2017). ISSN 24699969. 31, 40

[129] R. J. Shiue, Y. Gao, Y. Wang, C. Peng, A. D. Robertson, D. K. Efetov, S. Assefa, F. H. Koppens, J. Hone & D. Englund; "High-Responsivity Graphene-Boron Nitride Photodetector and Autocorrelator in a Silicon Photonic Integrated Circuit"; Nano Letters **15**, pp. 7288–7293 (2015). ISSN 15306992; 1507.00426. 31

[130] M. Freitag, T. Low, F. Xia & P. Avouris; "Photoconductivity of biased graphene"; Nature Photonics **7**, pp. 53–59 (2013). ISSN 17494885; 1202.5342. 31, 36, 38, 39, 46

[131] H. Fang & W. Hu; "Photogating in Low Dimensional Photodetectors"; Advanced Science **4**, p. 1700323 (2017). ISSN 21983844. 31

[132] F. Xia, T. Mueller, Y. M. Lin, A. Valdes-Garcia & P. Avouris; "Ultrafast graphene photodetector"; Nature Nanotechnology **4**, pp. 839–843 (2009). ISSN 17483395. 35, 42

[133] S. Schuler, D. Schall, D. Neumaier, L. Dobusch, O. Bethge, B. Schwarz, M. Krall & T. Mueller; "Controlled Generation of a p-n Junction in a Waveguide Integrated Graphene Photodetector"; Nano Letters **16**, pp. 7107–7112 (2016). ISSN 15306992. 36

[134] Q. Ma, C. H. Lui, J. C. Song, Y. Lin, J. F. Kong, Y. Cao, T. H. Dinh, N. L. Nair, W. Fang, K. Watanabe, T. Taniguchi, S. Y. Xu, J. Kong, T. Palacios, N. Gedik, N. M. Gabor & P. Jarillo-Herrero; "Giant intrinsic photoresponse in pristine graphene"; Nature Nanotechnology **14**, pp. 145–150 (2019). ISSN 17483395. 36

[135] E. Malic, T. Winzer, F. Wendler & A. Knorr; "Review on carrier multiplication in graphene"; Physica Status Solidi (B) Basic Research **253**, pp. 2303–2310 (2016). ISSN 15213951; 1609.06356. 40

[136] A. Tomadin, S. M. Hornett, H. I. Wang, E. M. Alexeev, A. Candini, C. Coletti, D. Turchinovich, M. Kläui, M. Bonn, F. H. Koppens, E. Hendry, M. Polini & K. J. Tielrooij; "The ultrafast dynamics and conductivity of photoexcited graphene at different Fermi energies"; Science Advances **4**, pp. 1–11 (2018). ISSN 23752548; 1712.02705. 40

[137] M. A. Ordal, R. J. Bell, R. W. Alexander, L. L. Long & M. R. Querry; "Optical properties of fourteen metals in the infrared and far infrared: Al, Co, Cu, Au, Fe, Pb, Mo, Ni, Pd, Pt, Ag, Ti, V, and W"; Applied Optics **24**, pp. 4493–4499 (1985). ISSN 0003-6935. 40

[138] K. Nagashio, T. Nishimura & A. Toriumi; "Estimation of residual carrier density near the Dirac point in graphene through quantum capacitance measurement"; Applied Physics Letters **102**, pp. 1–5 (2013). ISSN 00036951. 41

[139] E. Baudin, C. Voisin & B. Plaçais; "Hyperbolic Phonon Polariton Electroluminescence as an Electronic Cooling Pathway"; Advanced Functional Materials **30**, p. 1904783 (2019). ISSN 16163028; 1908.02953. 42, 49

[140] W. K. Tse & S. Das Sarma; "Energy relaxation of hot Dirac fermions in graphene"; Physical Review B **79**, pp. 2–6 (2009). ISSN 10980121. 42

[141] M. W. Graham, S. F. Shi, D. C. Ralph, J. Park & P. L. McEuen; "Photocurrent measurements of supercollision cooling in graphene"; Nature Physics **9**, pp. 103–108 (2013). ISSN 17452481; 1207.1249. 42

[142] A. C. Betz, S. H. Jhang, E. Pallecchi, R. Ferreira, G. Fève, J. M. Berroir & B. Plaçais; "Supercollision cooling in undoped graphene"; Nature Physics **9**, pp. 109–112 (2013). ISSN 17452481; 1210.6894. 42

[143] G. Alymov, V. Vyurkov, V. Ryzhii, A. Satou & D. Svintsov; "Auger recombination in Dirac materials: A tangle of many-body effects"; Physical Review B **97**, pp. 1–13 (2018). ISSN 24699969; 1709.09015. 42, 44

[144] F. Rana; "Electron-hole generation and recombination rates for Coulomb scattering in graphene"; Physical Review B - Condensed Matter and Materials Physics **76**, pp. 1–5 (2007). ISSN 10980121; 0705.1204. 43, 44

[145] Q. Guo, R. Yu, C. Li, S. Yuan, B. Deng, F. J. García de Abajo & F. Xia; "Efficient electrical detection of mid-infrared graphene plasmons at room temperature"; Nature Materials **17**, pp. 986–992 (2018). ISSN 14764660. 44

[146] Y. Yao, R. Shankar, P. Rauter, Y. Song, J. Kong, M. Loncar & F. Capasso; "High-responsivity mid-infrared graphene detectors with antenna-enhanced photocarrier generation and collection"; Nano Letters **14**, pp. 3749–3754 (2014). ISSN 15306992. 44

[147] J. C. König-Otto, M. Mittendorff, T. Winzer, F. Kadi, E. Malic, A. Knorr, C. Berger, W. A. De Heer, A. Pashkin, H. Schneider, M. Helm & S. Winnerl; "Slow Noncollinear Coulomb Scattering in the Vicinity of the Dirac Point in Graphene"; Physical Review Letters **117**, pp. 1–6 (2016). ISSN 10797114. 45

[148] A. Principi, M. B. Lundeberg, N. C. Hesp, K. J. Tielrooij, F. H. Koppens & M. Polini; "Super-Planckian Electron Cooling in a van der Waals Stack"; Physical Review Letters **118**, pp. 1–6 (2017). ISSN 10797114; 1608.01516. 48, 49, 54

[149] A. Woessner, R. Parret, D. Davydovskaya, Y. Gao, J. S. Wu, M. B. Lundeberg, S. Nanot, P. Alonso-González, K. Watanabe, T. Taniguchi, R. Hillenbrand, M. M. Fogler, J. Hone & F. H. Koppens; "Electrical detection of hyperbolic phonon-polaritons in heterostructures of graphene and boron nitride"; npj 2D Materials and Applications **1**, pp. 1–6 (2017). ISSN 23977132; 1705.10318. 48, 49

[150] S. Jia, X. Yu, H. Hu, J. Yu, T. Morioka, P. U. Jepsen & L. K. Oxenlowe; "120 Gb/s multi-channel THz wireless transmission and THz receiver performance analysis"; IEEE Photonics Technology Letters **29**, pp. 310–313 (2017). ISSN 10411135. 57

[151] V. Ryzhii, M. Ryzhii & T. Otsuji; "Negative dynamic conductivity of graphene with optical pumping"; Journal of Applied Physics **101**, p. 083114 (2007). ISSN 00218979. 57

[152] B. Sensale-Rodriguez, R. Yan, S. Rafique, M. Zhu, W. Li, X. Liang, D. Gundlach, V. Protasenko, M. M. Kelly, D. Jena, L. Liu & H. G. Xing; "Extraordinary control of terahertz beam reflectance in graphene electro-absorption modulators"; Nano Letters **12**, pp. 4518–4522 (2012). ISSN 15306984. 58

[153] Y. Yao, R. Shankar, M. A. Kats, Y. Song, J. Kong, M. Loncar & F. Capasso; "Electrically tunable metasurface perfect absorbers for ultrathin mid-infrared optical modulators"; Nano Letters **14**, pp. 6526–6532 (2014). ISSN 15306992. 58

[154] G. Liang, X. Hu, X. Yu, Y. Shen, L. H. Li, A. G. Davies, E. H. Linfield, H. K. Liang, Y. Zhang, S. F. Yu & Q. J. Wang; "Integrated Terahertz Graphene Modulator with 100% Modulation Depth"; ACS Photonics **2**, pp. 1559–1566 (2015). ISSN 23304022. 58

[155] V. Ryzhii, M. Ryzhii, A. S. Satou, T. Otsuji, A. A. Dubinov & V. Y. Aleshkin; "Feasibility of terahertz lasing in optically pumped epitaxial multiple graphene layer structures"; Journal of Applied Physics **106**, p. 084507 (2009). ISSN 00218979; 0908.2488. 58

[156] A. Locatelli, G. E. Town & C. De Angelis; "Graphene-based terahertz waveguide modulators"; IEEE Transactions on Terahertz Science and Technology **5**, pp. 351–357 (2015). ISSN 2156342X. 59

[157] S. E. Hosseininejad & N. Komjani; "Waveguide-Fed Tunable Terahertz Antenna Based on Hybrid Graphene-Metal Structure"; IEEE Transactions on Antennas and Propagation **64**, pp. 3787–3793 (2016). ISSN 0018926X. 59

[158] I. Khromova, A. Andryieuski & A. Lavrinenko; "Ultrasensitive terahertz/infrared waveguide modulators based on multilayer graphene metamaterials"; Laser and Photonics Reviews **8**, pp. 916–923 (2014). ISSN 18638899. 59

[159] X. Zhou, T. Zhang, L. Chen, W. Hong & X. Li; "A graphene-based hybrid plasmonic waveguide with ultra-deep subwavelength confinement"; Journal of Lightwave Technology **32**, pp. 3597–3601 (2014). ISSN 07338724. 59

[160] P. Kozma, F. Kehl, E. Ehrentreich-Förster, C. Stamm & F. F. Bier; "Integrated planar optical waveguide interferometer biosensors: A comparative review"; Biosensors and Bioelectronics **58**, pp. 287–307 (2014). ISSN 18734235. http://dx.doi.org/10.1016/j.bios.2014.02.049. 59

[161] P. Huang, S. Massabeau, J. Tignon, S. Dhillon, J. Mangeney & A. Degiron; "2D Materials Coupled to Hybrid Metal-Dielectric Waveguides for THz Technology"; in "International Conference on Infrared, Millimeter, and Terahertz Waves, IRMMW-THz," , volume 2018-Septepp. 1–1 (2018); ISBN 9781538638095; ISSN 21622035. 59

[162] K. S. Chiang; "Review of numerical and approximate methods for the modal analysis of general optical dielectric waveguides"; Optical and Quantum Electronics **26**, pp. S113–S134 (1994). ISSN 03068919. 62

[163] G. Kovacevic & S. Yamashita; "Waveguide design parameters impact on absorption in graphene coated silicon photonic integrated circuits"; Optics Express **24**, pp. 3584–3591 (2016). ISSN 1094-4087. 64

[164] K. F. Mak, M. Y. Sfeir, Y. Wu, C. H. Lui, J. A. Misewich & T. F. Heinz; "Measurement of the opptical conductivity of graphene"; Physical Review Letters **101**, p. 196405 (2008). ISSN 00319007. 65

[165] C. J. Johnson, G. H. Sherman & R. Weil; "Far Infrared Measurement of the Dielectric Properties of GaAs and CdTe at 300 K and 8 K"; Applied Optics **8**, pp. 1667–1671 (1969). ISSN 0003-6935. 66

[166] D. Grischkowsky, S. Keiding, M. van Exter & C. Fattinger; "Far-infrared time-domain spectroscopy with terahertz beams of dielectrics and semiconductors"; Journal of the Optical Society of America B **7**, pp. 2006–2015 (1990). ISSN 0740-3224. 66

[167] M. A. Ordal, R. J. Bell, R. W. Alexander, L. L. Long & M. R. Querry; "Optical properties of Au, Ni, and Pb at submillimeter wavelengths"; Applied Optics **26**, pp. 744–752 (1987). ISSN 0003-6935. 66

[168] B. Yu, Y. Liu, Y. Ye, J. Ren, X. Liu & Q. J. Gu; "High-efficiency micromachined sub-THz channels for low-cost interconnect for planar integrated circuits"; IEEE Transactions on Microwave Theory and Techniques **64**, pp. 96–105 (2016). ISSN 00189480. 69

[169] D. Gacemi, A. Degiron, M. Baillergeau & J. Mangeney; "Identification of several propagation regimes for terahertz surface waves guided by planar Goubau lines"; Applied Physics Letters **103**, pp. 1–5 (2013). ISSN 00036951. 69

[170] D. Giovanni, G. Yu, G. Xing, M. L. Leek & T. C. Sum; "Measurement of sub-10 fs Auger processes in monolayer graphene"; Optics Express **23**, p. 21107 (2015). ISSN 1094-4087. 69

[171] D. Svintsov, V. Ryzhii, A. Satou, T. Otsuji & V. Vyurkov; "Carrier-carrier scattering and negative dynamic conductivity in pumped graphene"; Optics Express **22**, pp. 19873–19886 (2014). ISSN 1094-4087. 71, 74

[172] J. Kim, S. S. Baik, S. H. Ryu, Y. Sohn, S. Park, B. G. Park, J. Denlinger, Y. Yi, H. J. Choi & K. S. Kim; "Observation of tunable band gap and anisotropic Dirac semimetal state in black phosphorus"; Science **349**, pp. 723–726 (2015). ISSN 10959203. 72

[173] Y. Liu, Z. Qiu, A. Carvalho, Y. Bao, H. Xu, S. J. Tan, W. Liu, A. H. Castro Neto, K. P. Loh & J. Lu; "Gate-Tunable Giant Stark Effect in Few-Layer Black Phosphorus"; Nano Letters **17**, pp. 1970–1977 (2017). ISSN 15306992. 72

[174] S. Chen, F. Fan, Y. Miao, X. He, K. Zhang & S. Chang; "Ultrasensitive terahertz modulation by silicon-grown MoS2 nanosheets"; Nanoscale **8**, pp. 4713–4719 (2016). ISSN 20403372. 72

[175] P. Gopalan, A. Chanana, S. Krishnamoorthy, A. Nahata, M. A. Scarpulla & B. Sensale-Rodriguez; "Ultrafast THz modulators with WSe 2 thin films [Invited]"; Optical Materials Express **9**, pp. 826–836 (2019). ISSN 2159-3930. 72

[176] J. Robertson; "High dielectric constant oxides"; EPJ Applied Physics **28**, pp. 265–291 (2004). ISSN 12860042. 79

[177] J. Neu & C. A. Schmuttenmaer; "Tutorial: An introduction to terahertz time domain spectroscopy (THz-TDS)"; Journal of Applied Physics **124**, p. 231101 (2018). ISSN 10897550. http://dx.doi.org/10.1063/1.5047659. 83

[178] I. Galbraith, R. Chari, S. Pellegrini, P. J. Phillips, C. J. Dent, A. F. Van Der Meer, D. G. Clarke, A. K. Kar, G. S. Buller, C. R. Pidgeon, B. N. Murdin, J. Allam & G. Strasser; "Excitonic signatures in the photoluminescence and terahertz absorption of a GaAs/Al xGa 1-xAs multiple quantum well"; Physical Review B - Condensed Matter and Materials Physics **71**, pp. 2–5 (2005). ISSN 10980121. 93

[179] B. S. Williams, S. Kumar, H. Callebaut, Q. Hu & J. L. Reno; "Terahertz quantum-cascade laser at $\lambda \tilde{}$ 100 μm using metal waveguide for mode confinement"; Applied Physics Letters **83**, pp. 2124–2126 (2003). ISSN 00036951. 112

[180] K. Unterrainer, R. Colombelli, C. Gmachl, F. Capasso, H. Y. Hwang, A. M. Sergent, D. L. Sivco & A. Y. Cho; "Quantum cascade lasers with double metal-semiconductor waveguide resonators"; Applied Physics Letters **80**, pp. 3060–3062 (2002). ISSN 00036951. 112

[181] K. Ito; "Selective Etching of Gallium Arsenide Crystals in H 2 SO 4 - H 2 O 2 - H 2 O System"; Journal of electrochemical society **118**, pp. 768–771 (1971). 112

[182] A. C. Ferrari, F. Bonaccorso, V. Fal'ko, K. S. Novoselov, S. Roche, P. Bøggild, S. Borini, F. H. Koppens, V. Palermo, N. Pugno, J. A. Garrido, R. Sordan, A. Bianco, L. Ballerini, M. Prato, E. Lidorikis, J. Kivioja, C. Marinelli, T. Ryhänen, A. Morpurgo, J. N. Coleman, V. Nicolosi, L. Colombo, A. Fert, M. Garcia-Hernandez, A. Bachtold, G. F. Schneider, F. Guinea, C. Dekker, M. Barbone, Z. Sun, C. Galiotis, A. N. Grigorenko, G. Konstantatos, A. Kis, M. Katsnelson, L. Vandersypen, A. Loiseau, V. Morandi, D. Neumaier, E. Treossi, V. Pellegrini, M. Polini, A. Tredicucci, G. M. Williams, B. Hee Hong, J. H. Ahn, J. Min Kim, H. Zirath, B. J. Van Wees, H. Van Der Zant, L. Occhipinti, A. Di Matteo, I. A. Kinloch, T. Seyller, E. Quesnel, X. Feng, K. Teo, N. Rupesinghe, P. Hakonen, S. R. Neil, Q. Tannock, T. Löfwander & J. Kinaret; "Science and technology roadmap for graphene, related two-dimensional crystals, and hybrid systems"; Nanoscale **7**, pp. 4598–4810 (2015). ISSN 20403372. 113

[183] X. Li, Y. Zhu, W. Cai, M. Borysiak, B. Han, D. Chen, R. D. Piner, L. Colomba & R. S. Ruoff; "Transfer of large-area graphene films for high-performance transparent conductive electrodes"; Nano Letters **9**, pp. 4359–4363 (2009). ISSN 15306984. 113

RÉSUMÉ

Le rayonnement THz est extrêmement attractif pour les études fondamentales de la matière et pour les applications émergentes, telles que la sécurité, l'imagerie médicale et la spectroscopie. Cependant, la gamme spectrale THz reste l'une des régions spectrales les moins exploitées, principalement en raison du manque de sources/amplificateurs THz puissants et compacts et de dispositifs passifs performants. Cette thèse concerne le développement de dispositifs THz avancés à base de graphène. Dans le premier projet, nous avons étudié la durée de vie des porteurs photo-excités dans des hétérostructures de van der Waals à base de graphène-hBN sous éclairement moyen-infrarouge. Nous avons rapporté, grâce à des mesures de photoconductivité dans le moyen infrarouge, que la durée de vie des porteurs photo-excités en faible densité et à faible énergie dans un tel dispositif est de 30ps. En allumant les phonons polaritons hyperboliques du hBN via une pompe électrique ou optique, nous avons démontré que la durée de vie des porteurs photoexcités s'ajuste de 30 ps à quelques picosecondes. Ce projet ouvre des perspectives intéressantes pour la réalisation d'un laser THz en exploitant des hétérostructures à base de graphène/hBN, pour le dévelopement de photodétecteurs THz très sensibles ainsi que pour l'optique à phonons polaritons. Le deuxième projet est centré sur l'étude des dispositifs originaux à base de guides d'onde hybrides semiconductor-metal couplés à une couche de graphene. Ces dispositifs, qui sont facile à fabriquer, peuvent agir comme des modulateurs THz et des amplificateurs THz. D'abord, nous avons étudié numériquement la relation de dispersion des deux modes fondamentaux de propagation de ces guides d'onde hybrides. Puis, nous avons caractérisé expérimentalement ces guides d'ondes hybrides couplés à du graphène en utilisant un système de spectroscopie THz avec le domaine temporel. Nous avons démontré que ces dispositifs peuvent agir comme des modulateurs Mach-Zehnder at 2 THz and 5.7 THz, les fréquences de coupures des modes propres TE0 et TE1 respectivement. Ce projet ouvre des perspectives intéressantes pour la modulation d'ondes THz et représente aussi une étape importante pour la réalisation d'un laser THz.

MOTS CLÉS

Terahertz,Graphene,Laser

ABSTRACT

THz radiation is extremely attractive for fundamental investigations of matter and emerging applications including, for example, security screening, medical imaging, and spectroscopy. However, the THz spectral range remains one of the least exploited spectral regions, mainly due to the lack of compact powerful THz sources/amplifiers and passive devices. This thesis concerns the development of advanced THz devices based on graphene material. The first project focuses on the carrier lifetime in neutral graphene-hBN van der Waals heterostructures under mid-infrared illumination. The carrier lifetime in such device for photoexcited carriers at low density and energy is reported to be 30 ps using mid-infrared photoconductivity measurements. By igniting the hyperbolic phonon polaritons in hBN via an electrical or optical pump, we demonstrate that the carrier lifetime is switched from 30 ps down to few picoseconds. This project opens interesting perspectives for the development of THz lasers by exploiting graphene/hBN heterostructures, for the realization of highly sensitive THz photodetectors as well as for phonon polariton optics. A second project reports on original devices based on hybrid semiconductor-metal waveguides coupled to the graphene layer. These devices, which are easy to fabricate, can act as THz amplitude modulators and THz amplifiers. First, we numerically investigate the dispersion relation of the two fundamental propagation modes of these hybrid waveguides. Then, we experimentally characterize these graphene-coupled waveguides using THz time-domain spectroscopy. We demonstrate that these devices act as Mach-Zehnder modulators at 2 THz and 5.7 THz, the cut-off frequencies of TE0 and TE1 modes respectively. This project opens interesting perspectives on the modulation of THz waves and represents an important building block for the realization of THz lasers.

KEYWORDS

Terahertz,Graphene,Laser